2016

Microscopic Study of Structure, Chemical Composition and Local Conductivity of La2/3Sr1/3MnO3 Films

Lina Chen
Louisiana State University and Agricultural and Mechanical College

MICROSCOPIC STUDY OF STURCTURE, CHEMICAL COMPOSITION AND LOCAL CONDUCTIVITY OF $La_{2/3}Sr_{1/3}MnO_3$ FILMS

A Dissertation

Submitted to the Graduate Faculty of the
Louisiana State University and
Agricultural and Mechanical College
in partial fulfillment of the
requirements for the degree of
Doctor of Philosophy

in

The Department of Physics and Astronomy

by
Lina Chen
B.S., Anhui University,China, 2006
M.S., University of Science and Technology of China, 2009
August 2016

Acknowledgments

First I wish to express my gratitude to my supervisors, Professor Jiandi Zhang and Ward Plummer, for supporting me during these past seven years. They have supported me not only financially through a research assistantship, but also academically and emotionally along the tumultuous path to finishing this thesis work. Without their help, I could not have completed my Ph.D, and this dissertation would not be possible. Jiandi is an instantly endearing and unforgettable person, and I have greatly benefited from his detailed guidance and scientific insight throughout my Ph.D study. I sincerely appreciate his instruction and help in finishing this research. With a keen eye, Ward has always provided invaluable insight into my research. He helped form the course of my research, and was always willing to read through my work. His extraordinary passion for research, great knowledge, and resourcefulness have been inspirations to me. I also would like to thank my committee members, Dr. Rongying Jin, Dr. Juana Moreno, and Dr. Jianwei Wang for their helpful advice and suggestions throughout my work.

It is a pleasure to thank some of the previous members of Dr. Zhang and Dr. Plummer's groups: Dr. Jinsun Shin, Dr. Xiaobo He, and Dr. Zhaoliang Liao. With their help, I learned the basics of this field, as well as how to manipulate our equipment in the ultrahigh vacuum and pulsed laser deposition systems. I also want to thank all the present members of the Dr. Zhang, Dr. Plummer, and Dr. Jin groups: Dr. Zhen Wang, Dr. Jisun Kim, Gaomin Wang, Dr. Hangwen Guo, Mohammad Saghayezhian, David Howe, Dr. Chen Chen, Dr. Fangyang Liu, Zhenyu Diao, Jianyu Pan, and Silu Huang for their collaboration and creation of a pleasant working environment.

I have found great joy these past seven years not only in the lab but also in my life, and I owe that to my loving husband. As a Ph.D candidate, often times experiments are unsuccessful and do not go as planned, which can be frustrating. Ronghua was always there to give suggestions and cheered me up. He was always right there when I needed him, and I deeply thank him.

My final and most heartfelt acknowledgement goes to my parents. Although they cannot read or speak English, I still want to thank them here. My parents are both traditional Chinese parents, who give their endless love, support, and care to their children, but are also unique in many ways, and they gave me the freedom to let me be myself. For both of these aspects, I thank them.

Table of Contents

Acknowledgments ii

List of Tables vi

List of Figures vii

Abstract xiii

Chapter 1: Structure and Physical Properties of Manganites in Bulk and Thin Film 1
1.1 Introduction 1
1.2 Perovskite Structure of Manganites 4
1.3 Physical Properties of Manganites 8
1.3.1 Phase Diagram of Manganites in Bulk 8
1.3.2 Physical Properties of Manganites Thin Films 12
1.3.3 Dead-layer in LSMO Thin Films 14
1.3.4 Surface Termination of LSMO Thin Films 19
1.3.5 Polarity Discontinuity at Interface 20
1.4 Summary 22

Chapter 2: Experimental Methods 24
2.1 Introduction 24
2.2 Film growth 25
2.2.1 Laser Molecular Beam Epitaxy (Laser-MBE) 25
2.2.2 Reflection High Energy Electron Diffraction (RHEED) 27
2.3 $In-Situ$ Characterization 29
2.3.1 Low Energy Electron Diffraction (LEED) 30
2.3.2 Angle resolved X-ray Photoelectron Spectroscopy (ARXPS) 33
2.3.3 Scanning Tunneling Microscopy/Spectroscopy (STM/STS) 38
2.4 *Ex-situ* Characterization 42
2.4.1 Scanning Transmission Electron Microscopy/Electron Energy Loss Spectroscopy (STEM/EELS) 42
2.4.2 Physical Property Measurement System (PPMS) 45
2.4.3 Summary 46

Chapter 3: Substrate treatment and LSMO film growth 47
3.1 Introduction and motivation 47
3.2 The treatment of $SrTiO_3$ substrate 48
3.3 High quality LSMO film growth 54
3.3.1 LSMO film growth 54
3.3.2 LSMO film quality characterization 59

3.4 Summary 61

Chapter 4: Layer-by-layer composition 63
4.1 Introduction and motivation 63
4.2 LSMO film interface composition from TEM 65
4.3 LSMO film surface composition from ARXPS 73
4.4 Summary 81

Chapter 5: Surface investigation 83
5.1 Introduction and motivation 83
5.2 Surface morphology and local tunneling conductivity(STS/STM) . . 84
5.3 Layer-by-layer structure 97
5.4 Film properties interpretation 102
5.5 Summary 104

Chapter 6: Introduce to the segregation theory and experiment discussion in LSMO 106
6.1 Introduction and motivation 106
6.2 Segregation in Metal alloys 111
6.2.1 Experimental Methods for Study of Grain Boundary Segregation 111
6.2.2 Theoretical Study of Grain Boundary Segregation 112
6.3 Present Results and Discussion for LSMO film 117
6.3.1 Segregation driving forces in LSMO films 118
6.3.2 Surface segregation in LSMO films 121
6.4 Summary 122

References 124

Vita 136

List of Tables

3.1 Parameters to calculate the IMFP of characteristic curves for STO . 50

3.2 List of parameters of Sr 3p, Sr 3d, Ti 2p and O 1s core levels for STO ARXPS calculation. 50

4.1 Fitting results for Sr profiles near the interface of LSMO films . . . 72

4.2 Parameters to calculate the IMFP of characteristic curves for LSMO 75

4.3 List of parameters for LSMO ARXPS Sr3d/La4d fitting. 75

4.4 List of parameters of Sr 3d, La 4d, Mn 2p and O 1s core levels for LSMO ARXPS calculation. 76

5.1 Relative atomic positions of the refined surface structure of 2 u.c. LSMO film grown on STO. 99

5.2 Relative atomic positions of the refined surface structure of 6 u.c. and 10 u.c. LSMO films. 100

List of Figures

1.1 Schematic diagram showing transition metal oxides with emergent phenomena due to the strong interactions among multiple degrees of freedom of correlated electron interaction. 2

1.2 (a) The perovskite structure of manganites; (b) Field splitting of the five-fold degenerate Mn^{3+} with d^4 $3d$ levels into lower t_{2g} and higher e_g levels, and further splitting of t_{2g} and e_g levels due to Jahn-Teller (JT) distortion. (c) The shapes of these $3d$ orbitals. 5

1.3 The electronic phase diagram of $RE_{1-x}AE_xMnO_3$ (x=0.45) bulk crystals in the plane of $< r_A >$ and variance. FM, CO/OO AFI, and SGI represent the phases of ferromagnetic metal, charge/orbital-ordered antiferromagnetic insulator, and spin glass-like insulator, respectively. Adopted from [25]. 7

1.4 Phase diagram of $RE_{1-x}AE_xMnO_3$ systems with doping concentration x and temperature T for representative distorted perovskites (a) $La_{1-x}Sr_xMnO_3$ (b) $Nd_{1-x}Sr_xMnO_3$ (NSMO) (c) $La_{1-x}Ca_xMnO_3$ (LCMO) (d) $Pr_{1-x}Ca_xMnO_3$ (PCMO). There are several electronic and magnetic states: paramagnetic insulating (PI); paramagnetic metallic (PM); spin-canted insulating (SCI); charge-ordered insulating (COI); antiferromagnetic insulating (AFI in the COI); canted antiferromagnetic insulating (CAFI in the COI). Adopted from [9]. 8

1.5 Phase diagram of $La_{1-x}Sr_xMnO_3$ ($0 \leq x \leq 1$). Crystal structures, magnetic, and electronic states: Jahn-Teller distorted orthorhombic (O'), orthorhombic (O), orbital-ordered orthorhombic (O"), rhombohedral (R), tetragonal (T), monoclinic (Mc), hexagonal (H); ferromagnetic (FM), paramagnetic (PM), antiferromagnetic (AFM), canted-AFM (CA); insulating (I) and metallic (M). Adopted from [76] 9

1.6 Schematic diagram showing the additional manipulation approaches to symmetry and degrees of freedom of correlated electrons that can be engineered at oxide interfaces. 14

1.7 Temperature dependent resistivity (a) and magnetization (b) for $La_{2/3}Sr_{1/3}MnO_3$ (LSMO) films with different thicknesses, grown on STO (001) substrates. Adopted from [27]. 15

1.8 Schematic drawings of the lattice cell distortion of epitaxial film under tension (a) or compression (b). Adopted from [18] 16

1.9 Relationship between the thickness of dead layer and lattice mismatch between LSMO and substrates. (a) LSMO films suffer from compressive or tensile strain based on different degrees of lattice mismatch between film and different type perovskite substrates; (b) Dependence of resistivity on temperature for LSMO films grown on substrates DSO, LAO, NGO, STO and NGO with 9 u.c. STO buffer layer; (c) Thickness of dead-layer *vs.* the degree of lattice mismatch ε. Adopted from [73, 75]. 17

1.10 Schematic drawings of the polar discontinuniy and screening the depolarizing field inside LAO. (a). the electrical potential divergence at the LAO/STO interface with TiO_2 termination is avoided by electronic reconstruction through adding half an electron to TiO_2 termination layer in reducing the valence of Ti^{4+} ; (b) the electrical potential divergence at the LAO/STO interface with SrO termination is also avoided by removing half an electron from the SrO termination layer in the introduction of oxygen vacancies. Adopted from [19] 21

2.1 The system combines growth chamber and analysis chamber. 25

2.2 Schematic diagram of Laser-MBE setup 26

2.3 (a) Schematic diagram of RHEED setup. (b) RHEED patterns and AFM images during growth of one unit cell layer. (c) Ideal layer by layer film growth [84]. 28

2.4 Theory predicted mean free path depends on electron energy (dash line) and mean free path of electrons in solid as a function of their energy. [85]. 29

2.5 (a) Schematic view of LEED setup.(b) LEED diffraction pattern of $Sr_3Ru_2O_7$ measured at 190 eV. (c) LEED-IV curve of (1,0) diffraction spot. 32

2.6 Schematic drawing of a typical ARXPS setup with photon source. . 33

2.7 XPS spectra of metal Ni irradiated with Mg source $K\alpha_{1,2}$ ($\hbar\omega$=1253.6 eV) [93]. 34

2.8 The bonding energy of C 1s peaks with different chemical states. . . 35

2.9 (a) An image of Omicron VT-STM. (b) Schematic view of STM setup. 39

2.10 (a) Schematic view of STEM setup. (b) HAADF and (C) ABF images of LSMO film on STO(001). 43

2.11 Instrument of Quantum Design PPMS. (b) Schematic diagram of four probe method. 45

3.1 (a) STM image and (b) height profile of STO annealed at 900 °C for 1 h with 10^{-4} Torr Ozone. (c) Angle resolved spectra of Ti 2p and Sr 3p peak. (d) Angle dependence of intensity ratios Ti2p/Sr3p, degassed in UHV for 1 hr at 100 °C (Rectangle), and annealed in 10^{-4} Torr Ozone for 1 hr with 500 °C (circular) and 900 °C (triangle). The pentagram is the theory result of STO with TiO_2 termination. 49

3.2 The morphologies of STO substrates are annealed at different temperature (a) 800 °C (b) 900 °C (c) 950 °C and (d)1000 °C. 51

3.3 Surface morphology, structure and termination characterizations of STO $ex-situ$ annealed at 900 °C for 3 hr with $O_2 \sim 1.45$ PSI. (a) STM image; (b) 1×1 LEED pattern; (c) and (d)Experimental data and theoretical calculation based on TiO_2 or SrO termination of the angle dependent intensity ration of Ti2p/Sr3p and Ti2p/Sr3d. . . . 52

3.4 (a) RHEED pattern of STO before film growth. (b) RHEED intensity oscillation pattern at various oxygen partial pressures. 55

3.5 Temperature dependent resistivity for LSMO films with different thicknesses grown at 80 mTorr. [75] 56

3.6 (a) RHEED images in the (100) direction for STO substrate. (b) RHEED images in the 20 u.c. LSMO films. (c) Typical RHEED intensity oscillations for 20 u.c. LSMO growth on STO (001) (d) Zoom in of the RHEED oscillations from (c) 57

3.7 Specular and extra maxima growth time for different thicknesses. . 59

3.8 (a) The STM image of the surface morphology of a 12 u.c. LSMO film. (V=1.0 V, I = 20 pA, T = 300 K) (b) LEED pattern of 12 u.c. LSMO film at RT at 95 eV. (c) HAADF-STEM image near the interface of 40 u.c. LSMO grown on STO (001) taken along [110]. The dish line indicates the interface between LSMO film and STO substrate. 60

4.1 (a) HAADF-STEM image and (b) ABF-STEM of 40 u.c. LSMO grown on TiO_2 terminated STO interface along [110]. A zoom-in ABF-STEM (Right) images and a structural model from the marked area shows the position for La/Sr, Mn and O atoms. 66

4.2 (Color online) HAADF-STEM image for La, Sr, Ti and Mn of LSMO/STO interface for (a) 8 u.c. taken along and (b) 4 u.c. taken along [100], respectively. 67

4.3 Profiles of chemical composition as a function of distance for 4 different areas of the 8 u.c. LSMO/STO interface extracted from the La-M edge, Ti-L edge, and Mn-L edge. 68

4.4 (Color online) The concentration profiles for La and Sr as a function of distance (unit cells) from the interface obtained from Fig4.3. . . 69

4.5 (Color online) (a) The STEM specimen includes a step. The cutting and step directions are along a; the STEM/EELS measurement direction is along b. (b) Based on sample (a) and (c) in Fig. 4.4 results and simple model of step, fitting results for sample (b) and (d) in Fig 4.4 are given. 70

4.6 (Color online) Averaged EELS elemental concentration profiles for La/Sr as a function of distance (unit cells) from the interface between (a) 40 u.c., (b) 8 u.c., (c) 4 u.c. LSMO, and STO substrate. 71

4.7 (a)Schematic diagram of ARXPS measurement. (b) raw ARXPS spectrum of Mn2p, Sr3d and La4d core levels for 65u.c. LSMO films grown on TiO_2 terminated STO substrate. 73

4.8 (a) Intensity ratio of Sr3d to La4d cores as a function of the emission angle θ for different thickness of LSMO films. (b) The experimental (20, 40 and 65 u.c.) and fitted (65 u.c.) intensity ratios of Sr3d/La4d as a function of emission angle for LSMO films. 77

4.9 Layer-by-layer dependence of Sr concentration of LSMO films near (left) the interface determined by STEM/EELS and (right) the surface determined by ARXPS. 78

4.10 Intensity ratio of Sr3d plus La4d to Mn2p cores as a function of the emission angle θ for different thicknesses of LSMO films. 79

4.11 (a) Intensity ratio of La4d to Mn2p cores as a function of the emission angle θ for different thickness of LSMO films. (b) Intensity ratio of La4d to Mn2p core as a function of film thickness for $\theta = 0^\circ$ and 81°. The inset presents the determined fraction of surface La/Sr-O termination for different thickness of LSMO films. 80

5.1 The STM morphological surface images of (a) 12 u.c., (b) 40 u.c. and (c) 60 u.c. LSMO films on STO with TiO_2 termination. The STM images are obtained at bias voltage V = 1.0 V, tunneling current setpoint $I_p = 20$ pA, and at room temperature). 84

5.2 The 200 $I - V$ curves of 40 u.c. LSMO film are measured at 10 different locations at (a) room temperature (RT) and (b) low temperature ($\sim$ 100K, LT) ($V_b = 0.5$ V, $I_{setpoint} = 50$ pA). 86

5.3 The differential tunneling conductance dI/dV spectra of 40 u.c. LSMO film measured at (a) room temperature (RT) and (b) low temperature ($\sim$ 100K, LT) ($V_b = 0.5$ V, $I_{setpoint} = 50$ pA). 87

5.4 (a) Bias shift of 40 u.c. LSMO film extracted from the STS spectra measured by using Pt-Ir tip and W tip at RT and low temperature (LT$\sim$ 100k). (b) The STS spectra of 10 u.c. $SrVO_3$ film measured at low temperature ($\sim$ 100k) ($V_b = 0.5$ V, $I_{setpoint} = 50$ pA (blue) and 100 pA(red)) 88

5.5 (a) Schematic view of 8 u.c. LSMO film grown on STO substrate capped with 10 u.c. SVO films. (b) The $dI/dV - V$ spectra of 8 u.c. LSMO film and 8 u.c. LSMO film capped with 10 u.c. SVO obtained at RT and LT $\sim$ 100 K, respectively. 89

5.6 (a) XPS O 1s core-level spectra of 40 u.c. LSMO film on STO substrate measured at RT and LT $\sim$ 100 K. (b) The binding energy difference for RT and LT La 4d, Sr 3d, Mn 2p and O 1s core-level spectra of 40 u.c. LSMO film. 91

5.7 (a) Schematic view of the polar surface of thick LSMO film based on the ARXPS results. The yellow arrow is the spontaneous polarization P_S. (b) Schematic diagram of the STS experiment. I is the tunnel current, and V is the bias applied between the tip and sample. 92

5.8 (a) Averaged and tunnel spectra of the 4, 6, and 8 u.c. LSMO films at LT $\sim$ 100 K. (b) The thickness dependence of bias shift obtained at RT and LT $\sim$ 100 K. 94

5.9 Temperature dependence of bias shift for 40 u.c. LSMO film measured with LED light on and off. 96

5.10 Comparison between experimental and theoretically-generated I(V) curves for the final structure of 2 u.c. LSMO film surface at RT . . 97

5.11 (a) bulk structure of LSMO and (b) Surface Structure of 2 u.c. LSMO film 98

5.12 Evolution of the interlayer atom distances and the tolerance factor (Γ) with film thickness. The distances are normalized by LSMO bulk lattice constant. 101

5.13 (a) Temperature dependence of the resitivity(ρ) of LSMO films with different thicknesses. (b) Thickness dependence of the conductivity (σ) measured at 6 K. (c) Schematic view of n u.c. LSMO film with a certain thickness (n_0) of nonmetallic layers near the surface and interface. (d) The thickness dependence of the measured conductivity (σ) times film thickness (n), measured at 6 K. The solid line is the fitting result with the suggested model by assuming a certain thickness (n_0) of nonmetallic layers near the surface and interface of LSMO films on STO (001) 103

6.1 Structure of a low-angle grain boundary (a) schematic illustration; (b) image of a [100] low-angle grain boundary in molybdenum revealed by the high-resolution electron microscopy. [172] 107

6.2 The schematic diagrams for (a) absorption, (b) phase separation, and (c) segregation. 109

6.3 (a) Schematics of interface and surface segregation for a crystalline film; (b) Schematics of grain boundary segregation in a polycrstalline solid. 109

6.4 (a) HAAD-STEM image and EELS elemental profiles for La, Sr, Ti and Mn of 40 u.c. LSMO/STO interface. (b) The concentration profiles for La and Sr as a function of distance(unit cells) from the interface of 40 u.c. LSMO film. 110

Abstract

The colossal magnetoresistance (CMR) manganites have attracted intensive study due to their richness of underlying physics and potential technological applications. Of particular interest is half-metallic $La_{2/3}Sr_{1/3}MnO_3$ (LSMO) because it possesses the highest known Curie temperature of the group ($\sim$ 370 K), which makes it a promising candidate for room temperature spintronic applications. On the other hand, LSMO ultrathin films exhibit a metal-insulator transition (MIT) when reducing film thickness. The origin of such a thickness-dependent MIT remains highly controversial, though understanding and controlling this kind of behavior is necessary for any possible device applications. An essential first step then, and the objective of this thesis project, is the characterization of the lattice structure and chemical composition.

The chemical composition of LSMO films grown on TiO_2-terminated $SrTiO_3$ (001) is quantified with unit cell precision by combining in-situ angle-resolved x-ray photoelectron spectroscopy (ARXPS), ex-situ scanning transmission electron microscopy (STEM), and electron energy loss spectroscopy (EELS). Substantial deviations in Sr doping concentrations from its bulk value are observed at both the interface and surface. Deviation at the interface is due mainly to single unit cell intermixing, while in proximity to the surface the segregation occurs in a wider thickness range. The surface undergoes a gradual conversion from MnO2 to (La/Sr)O layer termination with increasing thickness.

To study the consequences of the surface Sr segregation, scanning tunneling spectroscopy (STS) is applied to study the local electronic properties. According to the STS results, the nonmetallic character and spontaneous polarization at the surface of both thin and thick LSMO films is revealed. The difference in surface behavior

from the bulk is also confirmed by the temperature-dependent X-ray photoemission spectroscopy (XPS). Sr surface concentration deviation from the bulk value is unambiguously related to the nonmetallic behavior at the surface and interface, which is further verified by the thickness dependence of the film conductivity. The layer-by-layer variation in chemical composition generates an immense impact on the physical properties of the epitaxial oxide films and heterostructures. It naturally explains the existence of a 'dead' layer and the persistent nonmetallic behavior near the surface and interface of LSMO films, regardless their thickness.

Chapter 1

Structure and Physical Properties of Manganites in Bulk and Thin Film

1.1 Introduction

Oxygen is the most mass abundant chemical element on our planet. It is by mass 88.8% of our oceans and constitutes 49.2% of the earth's crust by forming various types of oxide minerals. Oxide materials have long been known as hosts for exotic and useful physical properties [1]. By using clay, a mixture of many oxide materials, pottery can be made, which is one of the oldest human technologies. Fragments of clay pottery found in the Jiangxi Province in China have been carbon dated to 20,000 years old [2]. Since the nature of metal-oxygen bonding can vary from ionic to covalent and metallic, transition metal oxides (TMOs) exhibit an enormous amount of structures and remarkable properties ranging from high-Tc superconductivity in layer-structured cuprates [3] and colossal magnetoresistance (CMR) in perovskite manganese oxides [4] to multiferroicity with simultaneous ferromagnetism and ferroelectricity [5]. These complex metal oxides have been used commercially in various fields, including electronics, medical diagnostics, and renewable energy. Nonvolatile memories, magnetic or electrical sensors and actuators, high-temperature superconductivity electrodes, electro-optic modulators, catalysts, solar/fuel cells and batteries all use metal oxide technology [6]. Fantastic physical phenomena and a rich array of multifunctional properties in TMOs are intimately related to strong electron correlation [7] and strong competition among multiple degrees of freedom: spin, charge, orbital, and lattice freedoms, as illustrated in the schematic diagram of 1.1.

In this thesis, I focus on the study of the relationship between physical properties and structure for both the surface and interface states of manganese perovskite

oxide $La_{2/3}Sr_{1/3}MnO_3$ thin films. The phase diagrams of the structures and magnetic/electronic properties, surface/interface effects, and the progress of possible applications are introduced in the first chapter. The mixed-valence manganese oxides with the perovskite structure $RE_{1-x}AE_xMnO_3$ (where RE is a trivalent rare-earth metal (La, Pr, Sm, etc.) and AE is a divalent alkaline-earth ion (Ca, Sr, Ba, etc.)) exhibit a metal-valence transition accompanied by so-called CMR effects [8]. These oxides have rich and complex physics related to the strong interactions among the charge, spin, orbital, and lattice degrees of freedom, such as double-exchange interaction, super-exchange interaction, Jahn-Taller type electron-lattice distortion, Hunds coupling etc. Since these strong electron-lattice and electron-electron interactions exist, their magnetic and transport properties are intrinsically coupled with the crystal structures and surrounding conditions, such as magnetic field, electric field, light, temperature, pressure, and strain [9].

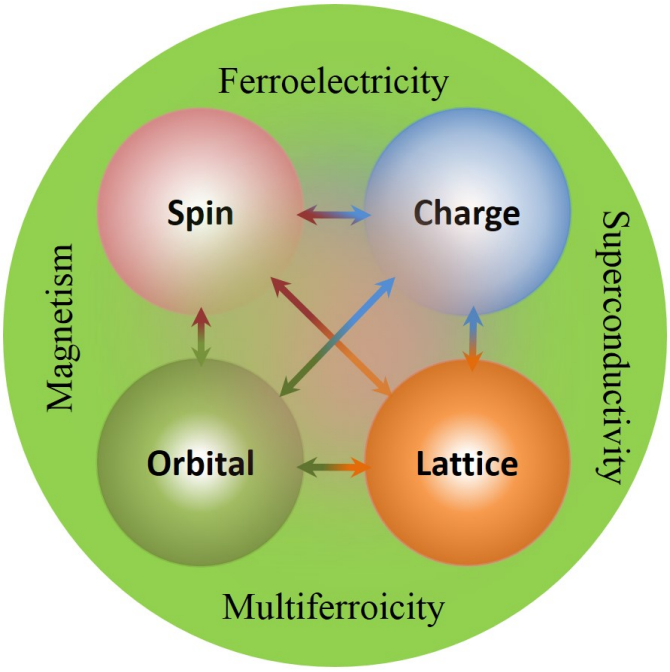

FIGURE 1.1: Schematic diagram showing transition metal oxides with emergent phenomena due to the strong interactions among multiple degrees of freedom of correlated electron interaction.

Manganites with perovskite structure have been studied for more than half a century [4, 8]. The original motivation for studying these manganese oxides was to develop insulating ferromagnets with a larger magnetization for high-frequency applications, which was expected due to the manganese ion's large magnetic moment compared to other $3d$ transition elements. Through the mid-1990s, the large amount of studies in these manganites with perovskite structure were motivated by the discovery of so-called CMR related to a metal-insulator transition in manganite $La_{1-x}Ca_xMnO_3$ (LCMO) thin films at 77 K and 6 T [10]. The observed CMR values ($\sim$ 100,000%) were four orders of magnitude larger than the giant magnetoresistance (GMR $\sim$ 50%) observed in thin-film structures composed of alternating ferromagnetic and non-magnetic conductive layers in the late 1980s [11, 12]. The discovery of GMR revolutionized hard drives for data storage and greatly changed modern computing, which garnered the 2007 Nobel Prize in Physics for Albert Fert and Peter Grünberg [13]. Besides these CMR effects having potential application in magnetic sensors and data storage, manganites are also half-metals that act as conductors to electrons of one spin orientation and as an insulator to those of the opposite orientation. This is due to their valence bands for one spin orientation being partially filled while there is a gap in the density of states for the other spin orientation. Half-metallicity with a fully spin-polarized conduction band is promising for potential spintronics application [14], a new type of technology which could be the basis of future revolutions in computing and storage with ultra-low power consumption [15]. In addition, since the underlying cause of the CMR effect comes from the nature of the complex strongly correlated electron system, where the lattice, charge, spin, and orbit are intrinsically coupled to each other, the manganites offer an outstanding opportunity to study fundamental physics from the

metal-insulator transition [9], charge and orbital ordering/reconstruction [17], and electronic phase separation [18].

1.2 Perovskite Structure of Manganites

Manganites have perovskite structure. An ideal perovskite structure has a cubic unit cell with an empirical formula ABO_3, shown in Fig. 1.2 (a). The A site cation is located on the corners, and the B-site cation is located in the cubic center while the oxygen atoms occupy the face centers and form a BO_6 octahedral. The RE trivalent and doping AE divalent ions occupy the A-site with 12-fold oxygen coordination, while the smaller Mn ion at the B-site is located at the center of an oxygen octahedron with 6-fold coordination [8].

To obtain a stable cubic structure, the relative ion size needs to meet certain conditions. A change of A- and B-site cation size induces slight bucking and distortion of the MnO_6 octahedra and will evolve several lower symmetry distorted structures. Tilting (rotation) of the MnO_6 octahedron is one possible lattice deformation in which the Mn-O-Mn angles become less than 180°. This comes from the connective pattern of the MnO_6 octahedron in the perovskite structure, which is quantified by the so-called Goldschmidt's tolerance factor [21, 22]. This factor describes the mismatch or degree of distortion between the A-O and B-O bond lengths in the ABO_3 cubic perovskite structure using the following equation:

$$t = \frac{< r_A > + r_O}{\sqrt{2}(< r_B > + r_O)} \tag{1.1}$$

where $< r_A >$, $< r_B >$ and r_O are the average A-site, B-site, and O anion ionic radii, respectively. The average A-site cationic radius $< r_A >$ can be calculated by the following formula:

$$< r_A >= \sum_i x_i r_i \tag{1.2}$$

where, r_i is the ionic radius of the i^{th} cation.

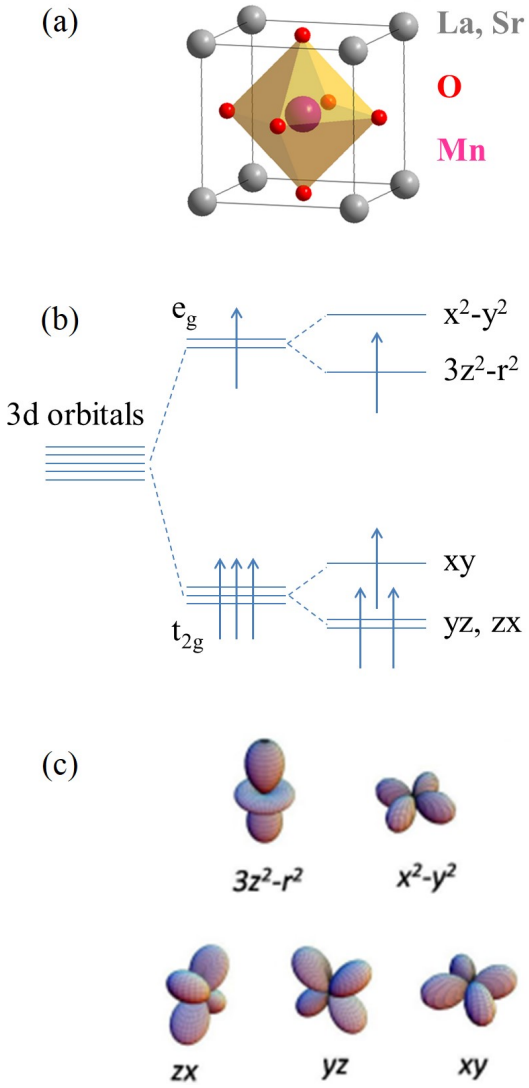

FIGURE 1.2: (a) The perovskite structure of manganites; (b) Field splitting of the five-fold degenerate Mn^{3+} with d^4 $3d$ levels into lower t_{2g} and higher e_g levels, and further splitting of t_{2g} and e_g levels due to Jahn-Teller (JT) distortion. (c) The shapes of these $3d$ orbitals.

The structure is ideally cubic with a B-O-B bond angle of 180 °. The structure will change to rhombohedral in the $0.96 < t < 1$ range and further change to

orthorhombic for $t < 0.96$, but the cubic perovskite structure will cease to be stable in the bulk when the t value is below the critical point of 0.89. The above relationship between tolerance factor t and lattice structure will vary slightly under different temperatures, pressures, or substrates used.

Since there are strong interactions among the electron, spin, orbit, and lattice as mentioned above, another possible lattice distortion is the deformation of the MnO_6 octahedron with one long Mn-O bond and two short bonds, where the long bonds alternatively in the $a-$ and $b-$directions arising from the Jahn-Teller (JT) effect due to strong electron-photon coupling [23, 24]. At the cross-over from localized to itinerant electronic structures, the dynamic and cooperative Jahn-Teller (JT) deformations in mixed valence perovskite manganites change the electronic structure because an appropriate local JT site deformation to lower symmetry removes the orbital degeneracy at a JT cation. Due to the symmetry of the crystal field defined by the lattice structure, in octahedral symmetry, the five-degenerate $3d$ orbital on the Mn sites splits into three lower level t_{2g} orbitals and two higher level e_g orbitals, as shown in Fig. 1.2. In doped $La_{1-x}Sr_xMnO_3$ systems, the Mn is a mixed valance of Mn^{3+} and Mn^{4+}. The Mn^{3+} ion has high-spin configuration d^4 with three electrons occupying the triply degenerate t_{2g} orbitals and one electron occupying the doubly degenerate e_g orbitals, while the Mn^{3+} ion with d^3 only occupies the three t_{2g} orbitals. The proportions of Mn ions for the valence states 3+ and 4+ are x and 1-x, respectively. According to the JT theorem, the degeneracy of the e_g and t_{2g} orbitals will be further removed by the structure distortion due to JT deformations. Therefore, the orbital degree of freedom of the Mn ion often shows long range ordering associated with the cooperative JT electron-lattice coupling.

As mentioned above, the averaged ionic radius of A-site $< r_A >$ (RE^{3+} and AE^{2+}) directly controls the tilting (rotation) of MnO_6 octahedra or the lattice distortion. Decreasing $< r_A >$ increases of tilting of MnO_6 octahedra (i.e. the Mn-O-Mn angles become less than 180°), which reduces the effective bandwidth W of the manganese e_g band and the hybridization between its e_g and oxygen $2p$ states in $RE_{1-x}AE_xMnO_3$. The bandwidth of solids has a direct effect on their magnetic and electronic properties, but in $RE_{1-x}AE_xMnO_3$ system, the material's behavior also involves strong electron correlation effects and electron-lattice interactions such as JT distortion, exchange interaction between local t_{2g} spins, and orbital ordering, etc., which induces many emergent quantum effects and physical phenomena. In Fig. 1.3, the electronic phase diagram shows that $RE_{1-x}AE_xMnO_3$ (x = 0.45) evolves from ferromagnetic metal to antiferromagnetic insulator to spin glass insulator with only the average A-site $< r_A >$ [25].

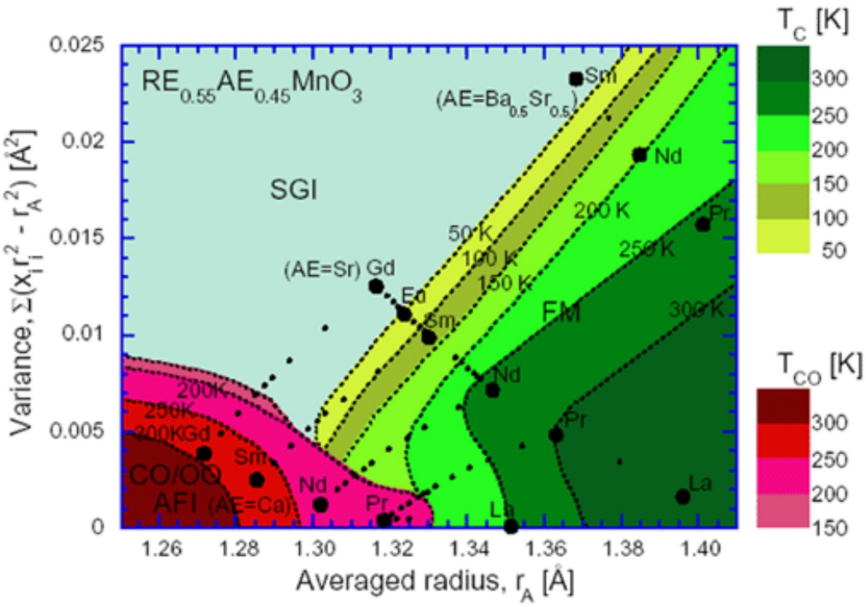

FIGURE 1.3: The electronic phase diagram of $RE_{1-x}AE_xMnO_3$ (x=0.45) bulk crystals in the plane of $< r_A >$ and variance. FM, CO/OO AFI, and SGI represent the phases of ferromagnetic metal, charge/orbital-ordered antiferromagnetic insulator, and spin glass-like insulator, respectively. Adopted from [25].

1.3 Physical Properties of Manganites

In these mixed valence manganites, subtle displacements in the crystal lattice can induce a significant change in magnetism and electronic or thermal transport due to the complex interplay between the lattice, spin, charge, and orbital degrees of freedom [9, 17]. Various electronic, structural, and magnetic phase diagrams of manganites are introduced and elucidated in the following section.

1.3.1 Phase Diagram of Manganites in Bulk

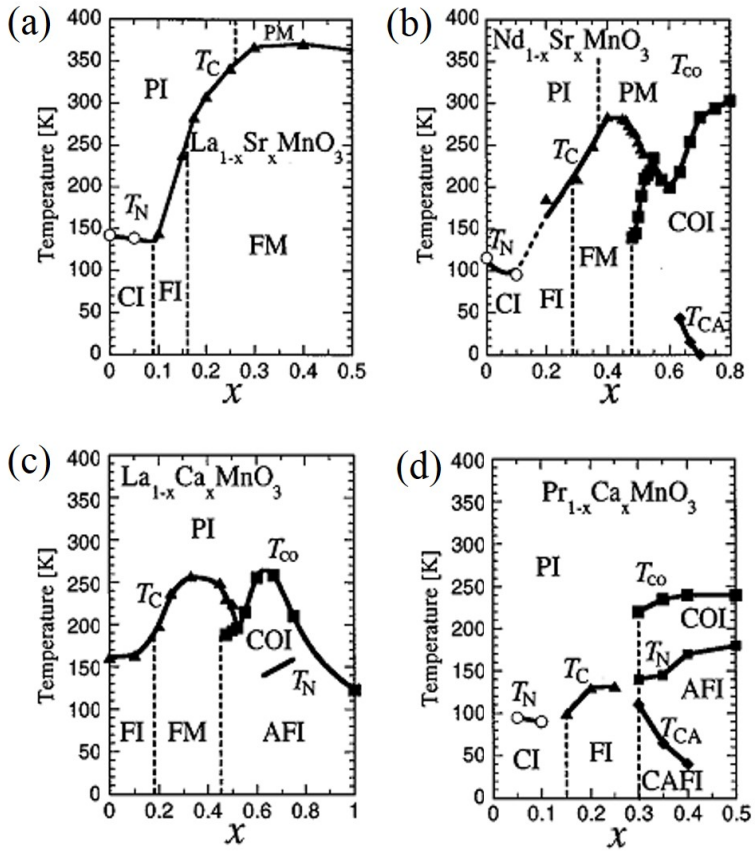

FIGURE 1.4: Phase diagram of $RE_{1-x}AE_xMnO_3$ systems with doping concentration x and temperature T for representative distorted perovskites (a) $La_{1-x}Sr_xMnO_3$ (b) $Nd_{1-x}Sr_xMnO_3$ (NSMO) (c) $La_{1-x}Ca_xMnO_3$ (LCMO) (d) $Pr_{1-x}Ca_xMnO_3$ (PCMO). There are several electronic and magnetic states: paramagnetic insulating (PI); paramagnetic metallic (PM); spin-canted insulating (SCI); charge-ordered insulating (COI); antiferromagnetic insulating (AFI in the COI); canted antiferromagnetic insulating (CAFI in the COI). Adopted from [9].

The bulk properties of CMR manganese oxides with perovskite structure have been systematically studied during last two decades. Figure 1.4 shows the phase diagrams of several types of manganites with different doping levels. The distorted perovskite $RE_{1-x}AE_xMnO_3$ shows rich structural, electronic, and magnetic phases with doping levels and temperature [9].

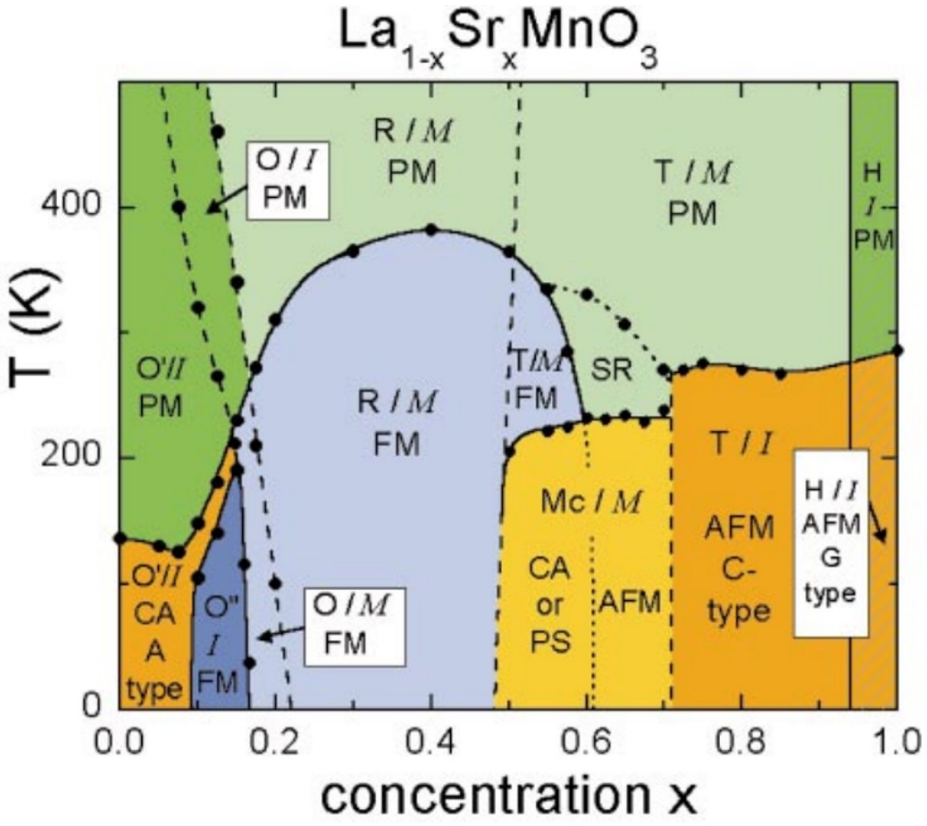

FIGURE 1.5: Phase diagram of $La_{1-x}Sr_xMnO_3$ ($0 \leq x \leq 1$). Crystal structures, magnetic, and electronic states: Jahn-Teller distorted orthorhombic (O'), orthorhombic (O), orbital-ordered orthorhombic (O"), rhombohedral (R), tetragonal (T), monoclinic (Mc), hexagonal (H); ferromagnetic (FM), paramagnetic (P-M), antiferromagnetic (AFM), canted-AFM (CA); insulating (I) and metallic (M). Adopted from [76]

The parent compound $LaMnO_3$ (LMO) is orthorhombic under uniaxial strain conditions and shows an antiferromagnetic insulator (AFI) transition with $T_N \sim$ 140 K. Its ground state magnetic structure has ferromagnetic *ab* planes stacked an-

tiferromagnetically along the c axis. The application of pressure and charge doping can induce metal-insulator transitions (MIT) [9], as well as huge magnetoresistance (CMR $\sim 10^5$ %) accompanied by magnetic transitions [10]. The strong interplay between lattice distortions, transport properties, and magnetic ordering results in rich and interesting physical properties and potential applications in doping LMO systems. Besides MIT and CMR, doped LMO systems probe more fundamental physics, such as double-exchange mechanisms, strong electron correlations, strong electron-phonon interaction, cooperative JT distortions induced by orbital order associated with Mn^{3+}, and charge ordering, etc. Here, we briefly illustrate the complex phase diagram of these manganites using $La_{1-x}Sr_xMnO_3$ as an example. In the range of doping x < 0.1, $La_{1-x}Sr_xMnO_3$ is an insulating canted antiferromagnetic structure (CI). With increasing doping level x, a ferromagnetic insulating phase can be obtained at $x \sim 0.1$. This FM phase keeps insulating up to $x \sim 0.17$, in which the double-exchange carrier is localized (Anderson localization) but can still mediate the ferromagnetic interaction between neighboring sites and realize the ferromagnetic state in a bond-percolation manner. Above 0.175, $La_{1-x}Sr_xMnO_3$ becomes metallic and the Curie temperature T_c dramatically increases with doping x from 250 K at 0.175 to the highest $T_c \sim 370$ K at $x \sim 1/3$. When doping x reaches to 0.5, the metallic ferromagnetic state will be followed by an antiferromagnetic insulating (or bad metal) state, where its electrical conductivity dramatically decreases with the increase of Sr doping, as shown in Fig. 1.5 [76].

Magnetic and electronic properties of these manganites are governed by exchange interactions between the Mn ion spins. The primary interactions arise from the nearest two Mn spins separated by an oxygen atom and are controlled by the overlap between the Mn $d-$orbitals and the O $p-$orbitals. Two-type distinguished exchange interaction models have been proposed to try to explain most of the magnet-

ic and electronic properties. One is the superexchange interactions, which depend on the orbital configuration following the rules of Goodenough-Kanamori [28]. Generally, the superexchange interaction is antiferromagnetic for $Mn^{4+} - O - Mn^{4+}$, while it can be ferromagnetic or antiferromagnetic for $Mn^{3+} - O - Mn^{3+}$ [28]. Another is the exchange interaction of $Mn^{3+} - O - Mn^{4+}$, named double exchange, where the Mn ions can exchange their valence electrons by transferring the e_g electron of Mn^{3+} to the empty e_g orbital of Mn^{4+} through the $Op-$orbital. The probability of the e_g electron transfer from Mn^{3+} to a neighboring Mn^{4+} is proportional to $t_0 cos(\theta/2)$, where θ is the angle between the spin vectors of the Mn ions [29, 30, 31]. Double exchange induces a metallic and ferromagnetic ground state in manganites. The origin of the complex magnetic, electronic, and structural phase diagrams of manganites versus the doping level x and the averaged ionic radius of A-sites $< r_A >$ arises from the competition between double exchange ferromagnetism and superexchange antiferromagnetism with different θ angular dependence and TJ distortion. In addition, the crystal structure of the $La_{1-x}Sr_xMnO_3$ system also undergoes a series of transitions from orthorhombic to rhombohedral to tetragonal, even becoming monoclinic and hexagonal at some conditions, as shown in the detailed phase diagram of single crystals of $La_{1-x}Sr_xMnO_3$ [76]. Figure 1.4 shows that LSMO's T_c of 370 is the highest T_c at optimal doping among the perovskite manganites family. In addition, the bond theory indicates that the FM metallic phase of LSMO has a half-metallic nature with fully polarized spin properties, which has been demonstrated by spin-resolved photoemission measurements [14].

High T_c (above room temperature) and half-metallicity make LSMO one of the most promising materials for metal-oxide-based spintronic devices, magneto-tunneling junctions, magnetic memory, etc. Spintronics is an emerging field of nanoscale electronics involving the detection and manipulation of electron spin

based on multilayer film structure and is one of the most promising technologies for future low power computing and data storage [15]. For these device applications, it is necessary to master the growth of high-quality thin films with well controlled, tailored properties. To achieve these emerging oxide-based advanced multifunction devices, physical properties and growth mechanisms of epitaxially complex manganese oxide thin films should be completely understood. Although there are still numerous unresolved issues in these complex manganese oxides, especially in their thin films and heterostructures due to involved strain at the surfaces and interfaces which adds complexity, major progress has been made in the growth techniques, structural characterization, and physical properties of the thin films and heterostructures.

1.3.2 Physical Properties of Manganites Thin Films

Phase diagrams in Fig. 1.3, Fig. 1.4, and Fig. 1.5 show that the rich physical properties associated with the multitude of competing ground states can be tuned by doping, structural manipulations, or the application of the external stimuli, such as magnetic/electric fields, light, and pressure, etc. The epitaxial growth of oxide films have been attracting attention due to these superior properties that could have great use in developing multifunction active devices. While significant progress has been made in the epitaxial growth technology of oxides films in the past decades, it has become increasingly clear that thin films, heterostructures, and interfaces/surfaces of traditional metal oxides display much more diversity in their physical properties and phenomena than in their bulks. Many novel physical properties and functionalities that are absent in bulks emerge in heterostructures or heterointerfaces due to broken symmetry and spatial quantum confinement at the interface or surface, such as two-dimensional electron gas (2DEG) behavior and superconductivity, etc. Figure 1.6 illustrates that the unique properties can be

deliberately introduced by surface structuring and interfacial engineering of thin films and multilayer structures, providing additional degrees of freedom to tailor functional properties.

Artificially engineering the interface of complex metal oxides is emerging as a powerful approach to explore new physical phenomena in materials science and electronics technology. For example, it has been found that the electronic reconstruction at the interface between tow non-magnetic band insulating oxides $LaAlO_3/SrTiO_3$ (polar LAO layer and nonpolar STO layer) can give rise to a high-mobility quasi-two-dimensional electron gas [32, 33], magnetism [34, 35] and superconductivity [36, 37]. Charge transfer at the interface between Mott insulating antiferromagnets $LaMnO_3$ (LMO) and band insulator $SrMnO_3$ (SMO) is another example of interface engineering and can lead to localized ferromagnetic ordering near the interface[38]. In addition, interfaces breaking inversion symmetry can be polar, hence charge transfer can be induced at the interface to avoid potential divergence due to the polar catastrophe [19]. In LAO/STO and LMO/SMO heterostructures, many theories and experiments [19, 38, 39, 40] show that the electrical properties and even chemical compositions near interfaces can be changed dramatically by charge transfer due to the polar nature of the structure.

The potential applications of CMR manganites in spin electronic devices or magnetic sensors requires that their films be as well controlled in terms of physical properties as their bulk counterpart [41]. However, as mentioned above, manganites have strong interplay between their charge, spin, orbital, and lattice, and their physical properties are very sensitive to the structure, especially the MnO_6 octahedral distortions and O-Mn-O bond lengths and angles [42, 43]. Manganite thin films show dramatically different physical properties than that of their bulks due to uniaxial strain from substrates [49, 50, 51, 52, 53, 54, 55, 56, 57, 58, 59, 60], chem-

ical element diffusion at the interface [61, 62, 63], surface termination of the thin film [64, 65], surface segregation and reconstruction [66, 67, 68, 69, 70], and oxygen vacancies [71] during high temperature growth. It is important to understand the growth mechanism of the complex manganese oxides, their chemical components, and the structure of their thin films on the atomic scale, especially their interface and surface because they have very different chemical and physical environments than the interior of films.

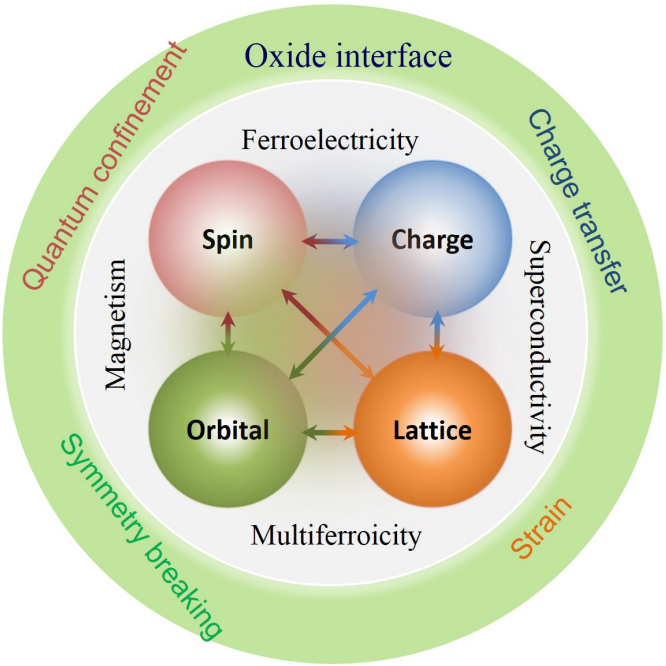

FIGURE 1.6: Schematic diagram showing the additional manipulation approaches to symmetry and degrees of freedom of correlated electrons that can be engineered at oxide interfaces.

1.3.3 Dead-layer in LSMO Thin Films

Since surface reconstruction, strain from the substrate, chemical element diffusion, and charge distribution occur at interface and surface, perovskite manganites thin films, especially ultra-thin films ($<$ 10 unit cells), have dramatically different physical properties from that of their bulk [18, 72]. Previous results show that epitaxial

LSMO with 1/3 Sr doping thin films grown on single crystal substrates show a non-ferromagnetic and insulating behavior when the thickness is less than certain unit cells ($\sim$ 2 to 3 nm for STO substrate, $\sim$ 10 nm for LAO with large lattice mismatch) [64, 65], the type of thickness used for the magnetic metal layer in GMR spin-valve devices. In other words, LSMO ultra-thin films (in several unit cells thickness) have serious degradation of both metallic and ferromagnetic functionalities compared with the bulk, shown in the phase diagram in Fig. 1.4. The degraded physical properties for these transition metal oxides thin films is referred to as the dead-layer phenomenon [44, 72, 73, 74, 75]. This dead-layer phenomenon is an obstacle which must be overcome before these manganese oxides can be applied for next generation nanoscale spintronics devices.

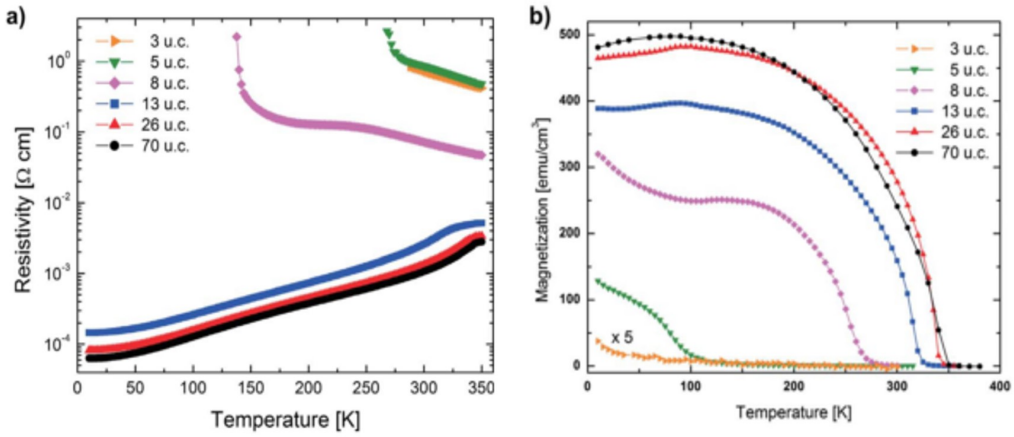

FIGURE 1.7: Temperature dependent resistivity (a) and magnetization (b) for $La_{2/3}Sr_{1/3}MnO_3$ (LSMO) films with different thicknesses, grown on STO (001) substrates. Adopted from [27].

The transport and magnetic measurements of ultrathin LSMO grown on STO (001) were systematically studied by M. Huijben et al. [27], and their results are shown in Fig. 1.7. In the LSMO/STO (001) thin films, thick films above 13 u.c. show a bulk-like metallic behavior over the temperature range, as well as a high

Curie temperature $T_C > 300$ K. When the thickness of the LSMO films decrease to less than 8 u.c, the LSMO films show insulating behaviors, as well as dramatically decreasing electrical conductivity. At the same time, the saturation magnetization and Curie temperature T_C also dramatically decrease when thickness of films is below the critical thickness 8 u.c. and is therefore defined as the dead-layer.

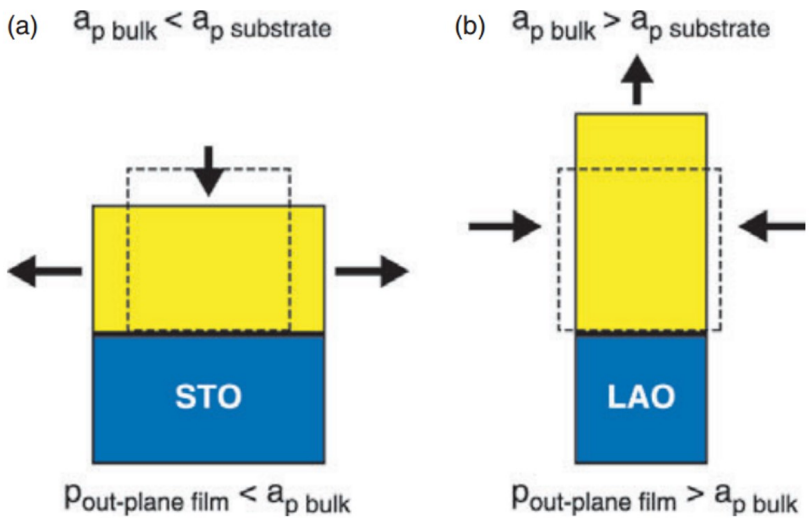

FIGURE 1.8: Schematic drawings of the lattice cell distortion of epitaxial film under tension (a) or compression (b). Adopted from [18]

Reducing the dead-layer behavior in LSMO thin films is of primary importance and has been attempted through optimizing the lattice match between LSMO film and substrate, growth conditions (Oxygen pressure), and tuning the interfacial chemical stoichiometry, etc [44, 72, 73, 74, 75]. For instance, the pervoskite LSMO ($x \sim 1/3$) bulk and several common pervoskite substrates have different lattice constants. Epitaxial LSMO films suffer compression or tensile strain from the substrate based on their relative lattice constants, which can be characterized by the degree of lattice mismatch $\xi = [a_{substrate} - a_{bulk}]/a_{substrate}$ along the interface. Positive ξ represents film suffering from in-plane tensile strain and compression strain along the out-plane growth direction, which is illustrated in Fig. 1.8 [18].

The deformation of epitaxial films comes from substrate mismatch strain, which can be characterized by utilizing high resolution transmission electron microscopy (HRTEM) and X-ray diffraction (XRD) alongside a common $\theta - 2\theta$ XRD scan or in-plane Φ-scan.

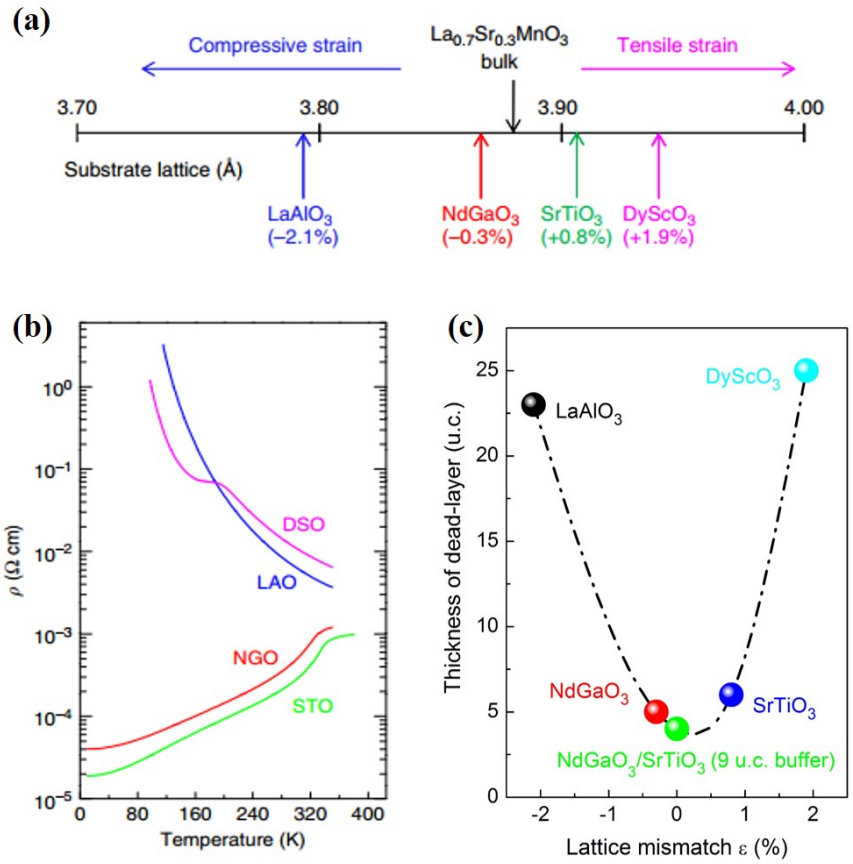

FIGURE 1.9: Relationship between the thickness of dead layer and lattice mismatch between LSMO and substrates. (a) LSMO films suffer from compressive or tensile strain based on different degrees of lattice mismatch between film and different type perovskite substrates; (b) Dependence of resistivity on temperature for LSMO films grown on substrates DSO, LAO, NGO, STO and NGO with 9 u.c. STO buffer layer; (c) Thickness of dead-layer *vs.* the degree of lattice mismatch ε. Adopted from [73, 75].

The most common substrates for CMR manganites are $SrTiO_3$ (STO, $a = 0.3905$ nm, cubic), $LaAlO_3$ (LAO, $a = 0.3788$ nm, pseudo-cubic), $DyScO_3$ (DSO, orthorhombic with $a = 0.5440$ nm, $b = 0.5717$ nm, $c = 0.7903$ nm) and $NdGaO_3$

(NGO, orthorhombic with $a = 0.5426$ nm, $b = 0.5502$ nm, $c = 0.7706$ nm). Lattice mismatch influences the values of the parameters, as well as the distortion of MnO_6 octahedra, as illustrated in Fig. 1.9(a). The degree of lattice mismatch between LSMO films and $LaAlO_3$ (LAO), $NdGaO_3$ (NGO), $SrTiO_3$ (STO), $DyScO_3$ (DSO) are -2.1%, -0.3%, 0.8% and 1.9%, respectively [44, 73]. Although the intrinsic origin of the dead layer still remains controversial, it is clear that the lattice mismatch between substrate and film plays an important role in physical properties of manganites. Many studies have found that, for thin films, lattice mismatch caused the structural modifications at their interfaces that affected their magnetic/electronic properties. Tensile or compressive strain induced distortion of MnO_6 octahedra that alters the Mn-O bond length and the Mn-O-Mn angle subsequently changes the main physical properties supported by double exchange and the Jahn-Taller effect. This can suppress ferromagnetism and reduce the ferromagnetic Curie temperature (T_c), analogous to the results from reducing the thickness of LSMO films growth on STO [50, 52, 54, 55].

The results of Fig. 1.9(b) show that both large compressive strain and tensile strain will induce subtle structural change and consequently affect the physical properties of LSMO films due to multiple comparable competing ground states and strong coupling between the lattice and electrons. Based on double exchange theory, the magnetic and electronic properties of LSMO are closely correlated to the $Mn-O-Mn$ bond angle and bond length of the MnO_6 octahedral. The strain on LSMO films from the substrate can be minimized, or even eliminated, by finely tuning the lattice constant of the substrates, for example by adding additional buffer layer between substrate and LSMO films. The relationship between the thickness of the dead layer and the degree of lattice mismatch ε was summarized in Fig. 1.9(C). For an LSMO film grown on NGO with a 9 u.c. STO buffer, the

strain effect on thin films can be minimized, but the film still has 3 u.c. of dead layer [75]. Some groups suggest that the dead layer of ultrathin LSMO films are due to phase separation related to structural inhomogeneities [52]. In addition, the authors pointed out that the phase separation phenomenon in LSMO was on the scale of a few nanometers, making it difficult to directly observe in experiment. Other recent evidence has also suggested that the distortion of MnO6 octahedra led to crystal-field splitting of e_g levels and lowering the $(3z^2 - r^2)$ orbital over the $(x^2 - y^2)$ orbital due to Jahn-Taller distortion. This gives strong electron-lattice coupling and causes orbital reconstruction at the interface [44, 46]. One study suggests that the dead-layer is caused by the hole depletion near the interface layers due to oxygen vacancy formation [71]. But in their results, the authors speculate that oxygen vacancies are partly caused by interfacial electric dipolar fields and lack any direct evidence to prove that oxygen vacancies exists at the interface. Furthermore, in some studies of dead layer thickness determined from transport and magnetization analysis, it was found that the critical thicknesses of electric and magnetic dead layers were different [27]. The thickness thresholds for metallicity and ferromagnetism are 7 u.c. and 4 u.c. respectively [27]. The conductivity of films increases with the thickness of the film, and the conductivity always is smaller than that of the bulk until the film is very thick ($>$ 40 u.c.). Recently ,it was also suggested that the dead layer may be associated with polar discontinuity-induced ion separation and electronic reconstruction at the interface and surface [16, 19, 20].

1.3.4 Surface Termination of LSMO Thin Films

The free surface of LSMO films is also of particular interest in this research. Similar to the interface, the surface of oxides often display different stoichiometry and chemical composition from their bulk due to the breaking down of long range

lattice periodicity, bonding, and chemical environment, resulting in an electrified surface-like interface that also profoundly affects electronic transport. In addition, it is normal for element segregation to take place at grain boundaries and surfaces in complex oxides [66, 67, 68, 69] and binary or ternary alloys [77, 78]. Research has shown that both the size difference and electrostatic interaction are responsible for segregation [67]. When growing LSMO on STO or other substrates, we would like to find what the final termination is for the LSMO films and whether or not we can replicate the substrate terminations. The answer to these questions are not only of concern when integrating half-metal LSMO thin films into spintronics applications, such as magnetic tunnel junctions where physical properties and functionalities are known to be largely determined by the chemical nature of the interface, but also is important in uncovering the underling physical mechanisms of these anomalous phenomena, and in the unique physical properties associated with their surface and interface effects. For instance, it was found that the emergence of quasi-two-dimensional electron gases (2DEG) and electric surface reconstruction in STO/LAO requires that the STO be TiO_2 terminated [16, 19]. Core-level photoemission spectroscopy studies show that electric reconstruction associated with the polarity discontinuity is the origin of the metallic electrons at the interface between the two band insulators LAO/STO. Heterostructures of LAO/STO show metallic conductivity with high mobility, as well as electronic reconstruction (Ti^{3+} signal) only for LAO/STO with TiO_2 termination, while LAO/STO with SrO termination still show insulating behavior[16, 19].

1.3.5 Polarity Discontinuity at Interface

Extensive efforts have been directed into the study of the intrinsic origin of the dead layer in LSMO/STO systems. Unfortunately, this problem still remains unresolved, and so far all attempts to completely eliminate the dead-layer behavior

have been unsuccessful. It seems that this unfavorable dead-layer is an inevitable consequence of the underlying physical mechanisms related to its interfaces, surfaces, and the complex oxide growth mechanisms. Analogous to the LAO/STO system, LMO or Sr-doped LMO is also a polar compound due to the existence of a polarity discontinuity [40, 70]. Therefore, many theories and experiments suggest that the polarity discontinuity at the interface may be the inevitable and intrinsic force responsible for the redistribution of charge and ions related to the physical properties and structure seen at the interface and surface, such as dead-layers, Sr diffusion at the interface, and Sr segregation at the surface.

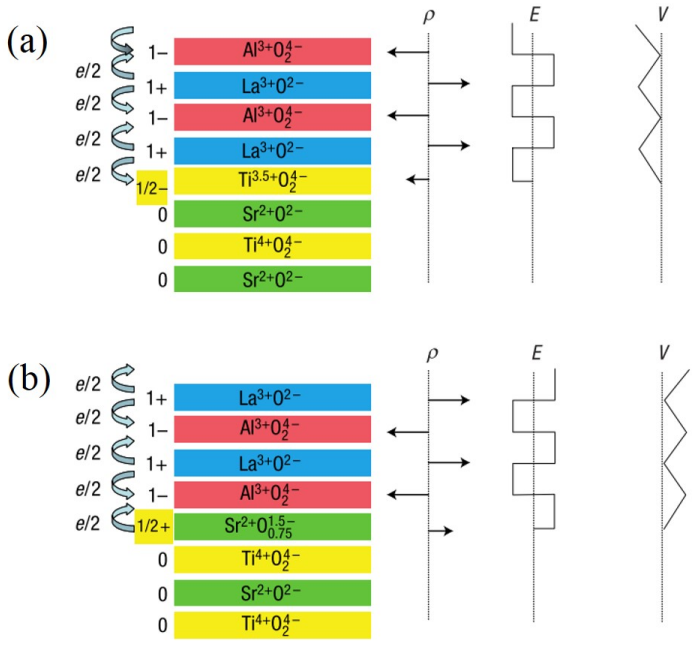

FIGURE 1.10: Schematic drawings of the polar discontinuniy and screening the depolarizing field inside LAO. (a). the electrical potential divergence at the LAO/STO interface with TiO_2 termination is avoided by electronic reconstruction through adding half an electron to TiO_2 termination layer in reducing the valence of Ti^{4+} ; (b) the electrical potential divergence at the LAO/STO interface with SrO termination is also avoided by removing half an electron from the SrO termination layer in the introduction of oxygen vacancies. Adopted from [19]

In heterostructures, there are interface dipoles resulting from band offset and bond polarizations. Consequently, a larger energy cost will arise from these polar discontinuities at abrupt heterointerfaces between layers with different polarities. However, the system responds to this energy cost by changing it electrical or structural properties, such as the creation of interface phases, or changing interface roughness with the creation of oxygen vacancies, element migration, or diffusion [19, 79, 80, 81]. It has been found that high-mobility electron gases corresponding to an electronic restructuring at the LAO/STO interface and an unfavorably roughening heterointerface are the results of avoiding an electrical potential divergence due to the inevitable polar discontinuities. In LAO/STO with the interface between polar and nonpolar layers, the polarity discontinuity induced potential divergence can be avoided by redistribution of charge (electronic reconstruction) and ions (such as oxygen vacancies, element diffusion, and segregation) across the LAO/STO interface, which has been discussed in detail by N. Nakagawa et al., in Fig. 1.10 [19].

1.4 Summary

Although many of studies and discussions related to the dead-layer phenomena have been reported, including interface-induced strain through changing different substrates, oxygen vacancy at the interface through changing oxygen growth pressures, charge redistribution driven by electrostatic potential at the interface, and even orbital reconstruction at interface, the origin of the dead-layer still remains highly controversial. Most of the previous reported work focused only on the external relationship between the thickness of dead-layer and growth conditions or different substrates. For LSMO thin films, detailed information about the precise chemical components and structure of the interface and surface on the atomic scale is still lacking. To better understand and explore the intrinsic origin of dead-layer

behavior, a series of $in-situ$ characterization tools combined with complex oxide growth capabilities, which are able to probe chemical components, surface/interface terminations, and the morphology and structure on the atomic scale are required. In this thesis, not only will the chemical composition and structure at interface between LSMO and STO on atomic scale be determined, but also the terminations and its thickness dependence will be analyzed quantitatively and discussed based on the results of angle-resolved X-ray photoelectron spectroscopy (ARXPS) and electron energy loss spectroscopy (EELS), as well as probing the local surface electronic states and its temperature dependence using scanning tunneling spectroscopy (STS).

Chapter 2
Experimental Methods

2.1 Introduction

Most devices are based on thin films or heterostructues, whose properties are strongly influenced by the film quality and surface/ interface qualities. Therefore, the deposition of high-quality films and the characterization of those thin films, during and after the fabrication process, is very important. For this thesis, films were grown through Laser Molecular Beam Epitaxy (Laser-MBE) methods with high powered laser beam ablation of the material from a target. Figure 2.1 depicts the system in our lab, which combines three sections: a cleaving chamber, growth chamber, and an *in-situ* analysis chamber. The cleaving chamber can be used to load and cleave samples, and the growth chamber houses the Laser-MBE setup including Reflection High Energy Electron Diffraction (RHEED). During the growth process, RHEED enables us to directly observe the growth dynamics and surface morphology.

Thin film characterization after the fabrication process can be divided into two categories: $in-situ$ characterization and $ex-situ$ characterization. After the fabrication of films in our growth chamber, films were immediately *in-situ* transferred into the analysis chamber, which includes components for X-ray photoelectron spectroscopy(XPS), Angle-resolved photoemission spectroscopy (ARPES), low-energy electron diffraction (LEED) measurements, and scanning tunneling microscopy/spectroscopy (STM/STS), which allows us to probe the materials' surface structures, chemical compositions, and electronic properties. These characterization tools detect electrons emitted or reflected from the surface, and therefore probe the topmost 1$\sim$10 nm of surfaces. Due to the surface sensitivity, those instruments

need to operate in high vacuum environments. By keeping the base pressure of the analysis chamber to 2×10^{-10} torr, surface contamination due to the adsorption of residual-gas molecules can be omitted over a given time period. The second group of possible measurements are the $ex-situ$ characterizations, including Scanning Transmission Electron Microscopy/Electron Energy Loss Spectroscopy (STEM/EELS) and Physical Property Measurement System (PPMS), which provide information about the structure and chemical composition of the entire sample and some transport measurements.

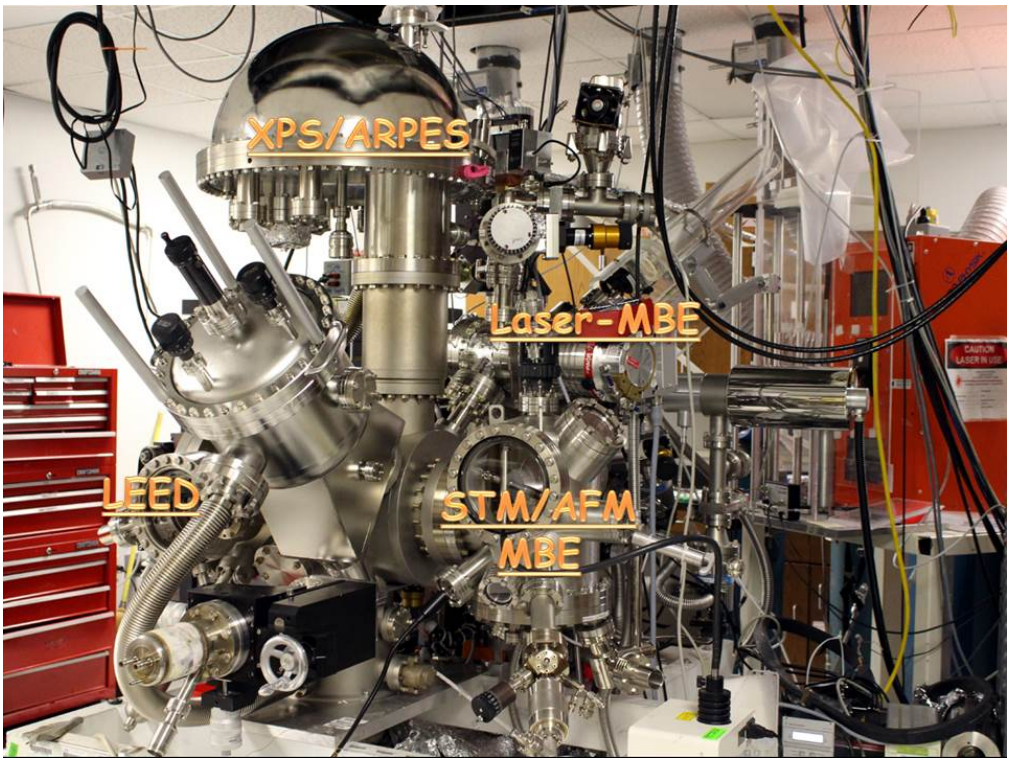

FIGURE 2.1: The system combines growth chamber and analysis chamber.

2.2 Film growth

2.2.1 Laser Molecular Beam Epitaxy (Laser-MBE)

Since the first laser was realized in 1960 by Maiman [82], many attempted to use lasers in film growth. It was finally accomplished in 1987 when a Bell Communica-

tions Research group successfully grew epitaxial high-temperature superconductor thin films [83]. After that, Pulsed laser deposition (PLD) has been widely used in the film growth of high-temperature cuprates and other complex oxides. Using this technique, novel materials that do not exist in nature can be designed and explored, such as superlattice films. The term Laser-Molecular beam epitaxy (MBE) was introduced to describe a PLD system with layer-by-layer growth capabilities, which also requires reflection high energy electron diffraction (RHEED) to monitor film growth.

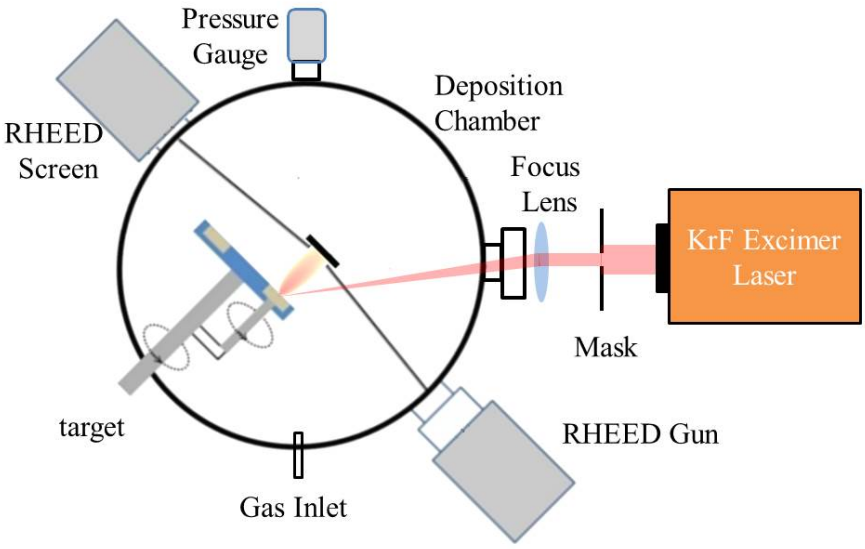

FIGURE 2.2: Schematic diagram of Laser-MBE setup

A typical setup for Laser-MBE is shown in Fig. 2.2. In the UHV chamber, six targets can be mounted in the target carousel, which allows us to grow multilayered films and superlattices. After being generated by the KrF laser and focused through a focus lens, the high powered pulsed laser beam is guided onto a target, which in turn delivers energy to the target, dissociating the target and forming a

plume. The plume expands rapidly with the fastest expansion direction along the normal direction to the target surface. By placing a substrate facing the target, materials of the plume can be deposited on the substrate to form a crystallized film. This deposition process occurs far from thermal equilibrium, and therefore the stoichiometry of the complex material can be preserved, which is the major advantage of Laser-MBE.

Many experimental parameters can influence film properties. Laser parameters such as energy, wavelength, pulse duration, and repetition rate can be altered to affect growth. Other conditions including substrate temperature, background gas, and pressure can also be important.

In our Laser-MBE system, we use a KrF excimer laser (COMPEx201) from Lambda Physik. It produces 248 nm light with pulse durations of 25 ns, maximum pulse energies of 700 mJ, and maximum pulse frequencies of 10 Hz. The commercially available premix gas (F2: 0.10%, He: 1.71%, Kr: 3.93%, Ne: 94.26%) is used as the excimer gas. In the UHV chamber, by precisely controlling the leak valve, the background gas can be changed, and gas pressure can be controlled from 3×10^{-10} torr to 0.1 torr, which is limited by the pressure requirements of the RHEED gun. The distance between the target and substrate is fixed at about 4 cm. The homemade heater allows us to change the substrate temperature from room temperature to 900 °C.

2.2.2 Reflection High Energy Electron Diffraction (RHEED)

RHEED is essential to Laser-MBE growth, which is a surface sensitive technique used to monitor the growth by probing the surface topography. The RHEED setup is schematically shown in Fig. 2.3(a). It consists of an electron gun and a phosphor screen to record the diffracted pattern. A high energy electron beam approaches the sample at a grazing angle, which for our system is about 2.5°. Some of the diffracted

electrons reach a phosphor screen and form a RHEED diffraction pattern, which is then captured by a charge-coupled device (CCD) camera. Our RHEED gun produces an electron beam energy up to 35 keV, which creates electrons with a mean free path of about 25Å. With an incidence angle of 2.5 °, the penetration depth is then about 1 for our samplesÅ, which is as small as one atomic layer and makes RHEED a surface sensitive diffraction technique.

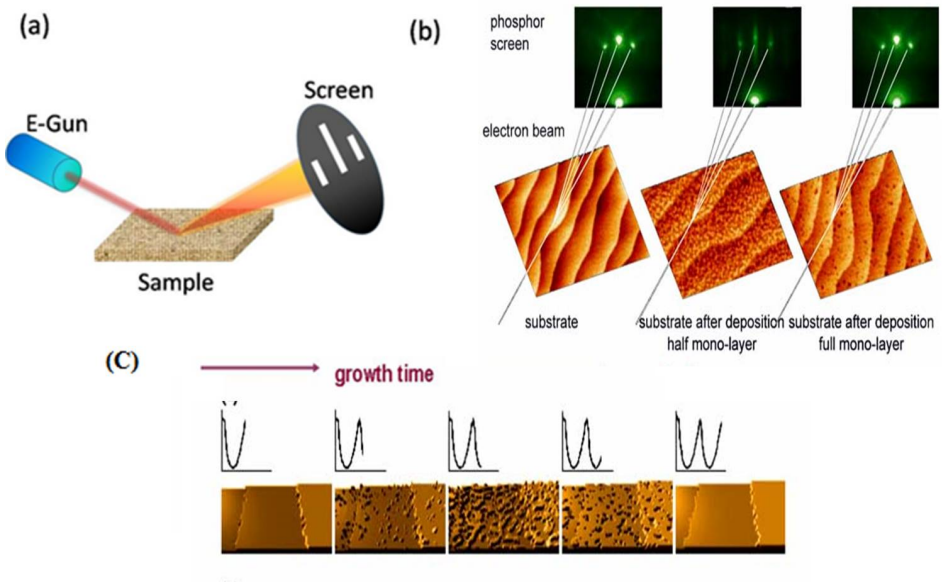

FIGURE 2.3: (a) Schematic diagram of RHEED setup. (b) RHEED patterns and AFM images during growth of one unit cell layer. (c) Ideal layer by layer film growth [84].

Figure 2.3(a) shows some RHEED patterns and response images recorded by Atomic Force Microscopy (AFM). Due to the grazing angle of the electron beam, RHEED patterns are very surface sensitive, which only gathers information from the surface layer of the sample. According to the surface structure, surface morphology, and the incident electron wavelength, the diffracted electrons interfere and create specific diffraction patterns, which provides information about not only the surface symmetry but also the surface topography.

The relation between the surface topography and RHEED pattern is shown in Fig. 2.3 (b) and (c). In Fig. 2.3 (b), due to the substrate being covered by a complete monolayer before growth, the RHEED pattern intensity is strong. With the deposition of a film, an incomplete monolayer begins to form, so the intensity of the spots decreases. As the film grows, it eventually completes a full monolayer, and as it does, the intensity of spots becomes strong again. Figure 2.3 (c) shows an ideal layer-by-layer growth process and corresponding oscillation curve. During film growth, RHEED is used to provide information on the film flatness and crystallization. By tracking the intensity of the spots of the reflected pattern, we can observe the RHEED oscillations, which is used to evaluate the growth rate, the number of grown layers, and directly observe the growth dynamics.

2.3 $In-Situ$ Characterization

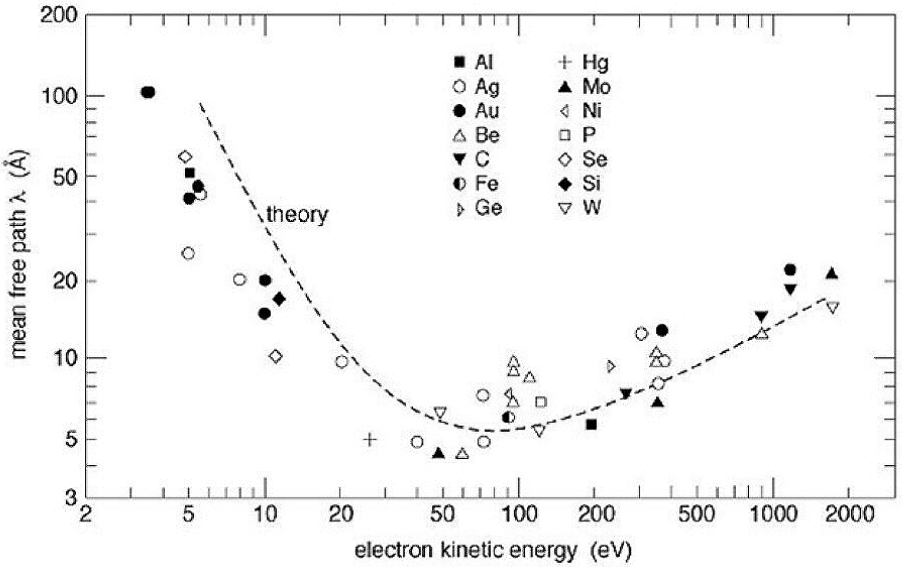

FIGURE 2.4: Theory predicted mean free path depends on electron energy (dash line) and mean free path of electrons in solid as a function of their energy. [85].

The analysis chamber contains some surface sensitive instruments, which enable us to $in-situ$ probe the structure, chemical composition and electronic properties

of the film surface to several layers deep. For different equipment, the probing depth differs depending on the sample, beam energy, and direction. Many experiments can be performed to measure the attenuation length in different materials with different energies, where the attenuation length is equivalent to mean free path. Figure 2.4 shows a collection of experimental determinations of mean free path as a function of energy for different metals.

2.3.1 Low Energy Electron Diffraction (LEED)

LEED is a surface sensitive technique for the determination of the surface structure of crystalline materials. Figure 2.5(a) shows a schematic diagram of LEED setups, which shows a collimated beam of low energy electrons produced by an electron gun which reach a fluorescent screen, where a LEED pattern formed by diffracted electron spots can be observed. The energy of the electron beam ranges from 20 to 200 eV, which therefore determines the electron's wavelength via the de Broglie relation:

$$\lambda = h/p = h/mv = h/\sqrt{2mE} \tag{2.1}$$

where λ is the wavelength of a particle with momentum p, mass m, velocity v, and energy E. h is Planck's constant. From this equation, for an electron with kinetic energy of 150.4 eV, its wavelength is 1 Å. That is:

$$\lambda_e[\mathring{A}] = \sqrt{150.4/E[eV]} \tag{2.2}$$

Similarly, the wavelength of electrons with kinetic energy 20-200 eV ranges from 2.7-0.87 Å, which is comparable with the lattice constant of a crystal. The penetration depth is several angstroms, estimated from Fig. 2.4, which enables LEED to be an excellent probe for the surface structure of a crystallized sample. Qualitatively, the LEED diffraction pattern can be analyzed to get information on the

symmetry of the surface structure. Figure 2.5 (b) is the LEED pattern of parent $Sr_3Ru_2O_7$ at 190 eV, where the surface has a $\sqrt{2} \times \sqrt{2}$ reconstructed pattern. For quantitative analysis, the electron beam energy can be changed, which produces a shifted diffraction pattern. Simply by changing the wavelength of electrons, the intensity of different spots can be tracked and recorded as a function of incident electron beam energy to generate Intensity-Voltage (I-V) curves shown in Fig. 2.5(c). These are used in theoretical calculations to determine accurate information on the atomic surface positions. Full dynamic calculations are computationally costly, so a perturbational tensor LEED (TLEED) approximation has been developed and implemented by Rouse and Pendry [86, 87, 88, 89]. In the process of I-V curve refinement, the so-called reliability factor (R_P-factor) is used to quantitatively evaluate the quality of a certain model between the theoretical and experimental I-V curves. The R_P-factor used in this work is one developed by Pendry [90]. R_P is based on logarithmic derivatives of the IV spectra intensity $I(E)$:

$$L = \frac{1}{I(E)} \frac{dI(E)}{dE} \tag{2.3}$$

When the IV curve is near a minima with $I(E) \approx 0$, a singularity occurs in the logarighmic derivative. To avoid such singularities, a Y function is introduced:

$$Y = \frac{L}{1 + L^2 V_{oi}^2} \tag{2.4}$$

where V_{oi} is the imaginary part of the optical potential that is used to keep the function finite within the range of $\pm 1/2V_{oi}$. While an energy dependence of $Voi(E)$ is introduced in the calculation of the theoretical IV spectra as outlined above, a constant average value (V_{oi} = - 4eV) is assumed in the calculation of R_P.For a particular I-V beam, R_P is given by:

$$R_p = \frac{\int (Y_{\text{th}} - Y_{\text{exp}})^2 dE}{\int (Y_{\text{th}}^2 + Y_{\text{exp}}^2) dE} \tag{2.5}$$

where Y_{exp} and Y_{th} are the Y functions for the experimental and theoretical beams respectively, and V_{oi} is the imaginary part of the electron self-energy.

If $R_P = 0$ there is perfect correlation between the theoretical and experimental I-V curves. $R_P = 1$ means that theory and experiment are completely uncorrelated. The lower R_P factor acquired, the better is surface structural determination. Usually, an R_P of about 0.3 is sufficient to corroborate a certain structure.

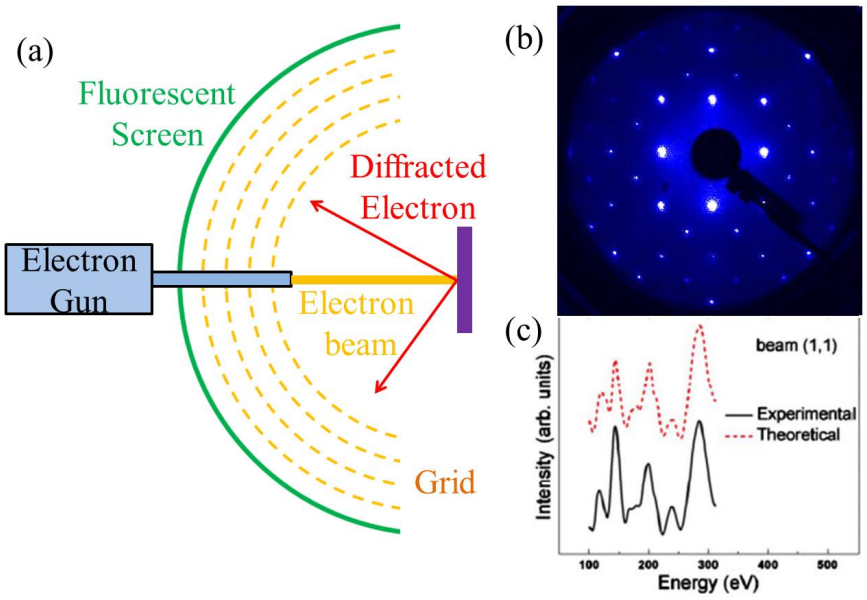

FIGURE 2.5: (a) Schematic view of LEED setup.(b) LEED diffraction pattern of $Sr_3Ru_2O_7$ measured at 190 eV. (c) LEED-IV curve of (1,0) diffraction spot.

The LEED used in this project is an Omicron LEED. It works in our UHV system where the pressure is maintained at 3×10^{-10} Torr at room temperature. LEED I-V data acquisition is done with a high resolution camera and LabView programmed software.

2.3.2 Angle resolved X-ray Photoelectron Spectroscopy (ARXPS)

Based on the photoelectric effect, photoelectron spectroscopy uses photons to ionize the sample and emit electrons, which can be analyzed to study the composition and electronic state of a sample surface. Traditionally, there are two types: X-ray photoelectron spectroscopy (XPS) and Ultraviolet Photoelectron Spectroscopy (UPS). UPS creates electrons of energy 10-45 eV to study valence levels, which is not utilized here. XPS is based on a soft x-ray source with a photon energy range of 200-2000 eV to analyze core levels, which can be used to determine the elemental composition, empirical formula, chemical state, and electronic state of the elements that exist within a material. The standard detection limits range from 0.1 to 1.0 atom%.

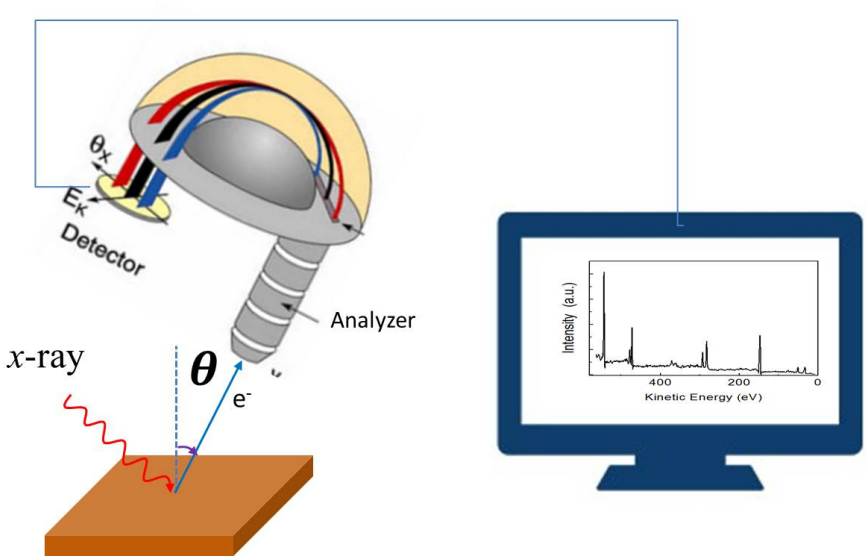

FIGURE 2.6: Schematic drawing of a typical ARXPS setup with photon source.

Figure 2.6 depicts the schematic of an ARXPS setup, which shows a beam of photons produced by the X-ray source incident on the sample. The X-rays are usually generated by high velocity electrons bombarding Al or Mg anodes, which produce emission photon energies of 1486.7 eV or 1253.6 eV respectively. To get a

better signal, a monochromator can be used after the X-ray source, which removes any continuous background Bremsstrahlung radiation or "white radiation". The monochromator can also help further focus the x-ray beam. After the monochromator, the photon linewidth is narrow, and therefore the ARXPS resolution can be improved. When the photons are absorbed, the electrons are emitted from the sample and detected by the analyzer. Based on the kinetic energy and number of electrons, the spectrum of electron intensity versus binding energy can be determined live.

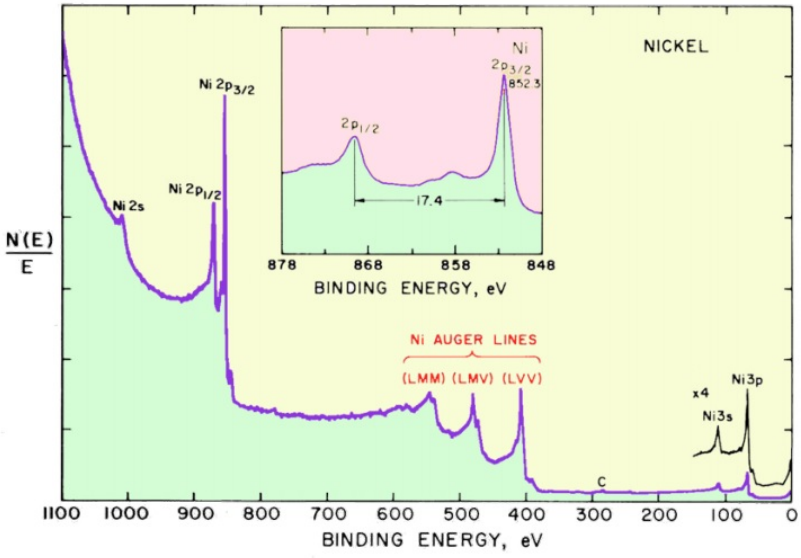

FIGURE 2.7: XPS spectra of metal Ni irradiated with Mg source $K\alpha_{1,2}$ ($\hbar\omega$=1253.6 eV) [93].

In ARXPS measurements, the energy of photon is known so that the electron binding energy of each emitted electron, which is the difference between the energies of the final and initial states, can be determined using an equation based on the work of Ernest Rutherford [96]:

$$E_b = E_p - (E_k + \Phi) \tag{2.6}$$

where E_b is the binding energy (BE) of the electron, E_p is the energy of the X-ray photons being used, E_k is the kinetic energy of the electron as measured by the instrument, and Φ is the work function of the spectrometer. For the analyzer, the work function changes and therefore needs to be calibrated with a standard sample, which for our system is done with a clean Au sample with a $4f$ peak.

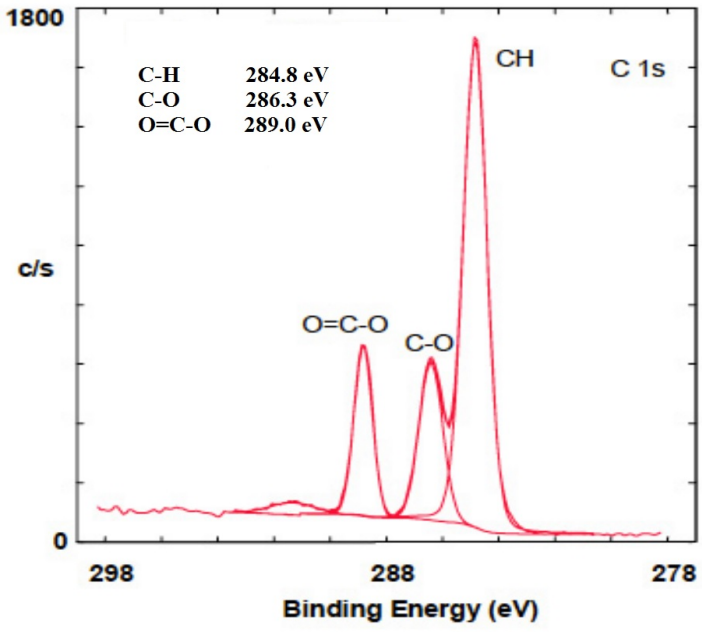

FIGURE 2.8: The bonding energy of C 1s peaks with different chemical states.

The X-ray photoelectron spectrum consists of a few basic types of peaks: (1) peaks from core levels, (2) peaks from valence levels, (3) peaks from X-ray excited Auger decay (Auger series), and (4) other peaks, such as multiple splitting, ghost peaks, and satellite peaks [92]. Figure 2.7 is a typical XPS spectrum for metallic Ni, which contains: the valence band (3d, 4s) at E_B of several eVs; very weak 3p, 3s, and 2s peaks at about 66, 110 and 1008 eV respectively; Auger peaks arising from x-ray induced Auger emission marked with LMM, LMV, and, LVV; and an intense 2p peak and its satellite peaks around 860 eV, which is further expanded and shown in the inset of Fig. 2.7. Here the descriptions of the XPS peaks (4s,

3d, 3p, 3s, 2s, and 2p) are based on the electron configuration of the atoms. The 2p peak is split into $2p_{1/2}$ and $2p_{3/2}$ arising from spin-orbit coupling. Two possible states, characterized by the quantum number j ($j = l + s = l \pm 1/2$), arise when $l \neq 0$, where the intensity ratio between two peaks with $j_+ = l+1/2$ and $j_- = l-1/2$ is given by $(l + 1)/l$, based on the degeneracy of each spin state [95]. Spin-orbit splitting values can be found in a variety of databases [93, 94], which are needed when fitting spectra.

Satellite peaks are important phenomenon in XPS quality determination for many reasons. Surface charging, shake-off and shake-up effects (i.e. a sudden change in Coulombic potential as the photoejected electron passes through the valence band), plasmon electronic excitation, and multiple X-ray source photon energies can all observed with satellite peaks.

Chemical shifts are another possible signature in XPS, which includes final state and initial state chemical shifts. The final chemical shifts are due to charging effects in an insulating sample, which can cause the peaks to shift to higher binding energies. The initial state chemical shifts can be used to distinguish different oxidation states and chemical environments. For the same element, the binding energy of a core electron can be different for different samples, and the difference can be from one tenth of an eV to a few eV. The exact binding energy of an electron is determined by the core level of the electron, the oxidation state of the atom, and the local chemical and physical environment. For an atom, a higher positive oxidation state means a higher positive charge for the atom and more Coulomb interaction, which therefore requires the most energy for electrons to escape. As a result, a higher positive oxidation state means the core level has a higher binding energy, which is shown in Fig. 2.8. Three different carbon chemical bondings can be clearly identified for C 1s peaks. Higher oxidation states have higher binding

energies in C 1s core levels, though the energy differences are within 1 eV. The line widths are also different, which is related to the lifetime of the photoelectrons coming from the specific core levels. Although the binding energy can be changed due to the chemical shift, the binding energy difference between the two spin-orbits of one element remains the same.

In X-ray photoelectron spectroscopy, the contribution to the signal intensity I_A by the layer thickness dz at the depth z is given by [97]:

$$dI_A(z,\theta) = T_A \sigma_A n_A(z) exp(-z/\lambda_A cos\theta) dz \tag{2.7}$$

where T_A is the transmission coefficient of the analyzer, σ_A is the photoionization cross-section, λ_A is the inelastic mean free path (IMFP) of analyzed photoelectrons, and θ is the emission angle shown in Fig. 2.6.

Further assuming that the value λ_A depends only on the kinetic energy of photoelectrons, we obtain the intensity I_A of an element A [98]:

$$I_A(\theta) = T_A \sigma_A \int_0^\infty n_A(z) exp(-z/\lambda_A cos\theta) dz \tag{2.8}$$

The XPS intensity ratio I_A/I_B for elements' A and B core level peaks is defined as [99]:

$$\frac{I_A(\theta)}{I_B(\theta)} = \frac{T_A \sigma_A \int_0^\infty n_A(z) exp(-z/\lambda_A cos\theta) dz}{T_B \sigma_B \int_0^\infty n_B(z) exp(-z/\lambda_B cos\theta) dz} \tag{2.9}$$

To quantitatively analyze ARXPS data $I_A(\theta)/I_B(\theta)$, Eq. 2.9 and relative parameters are used. σ can be found in XPS handbooks and T is related to the analyzer used. IMFP λ is the only unknown parameter here.

The predictive equation for the Inelastic mean free path (IMFP) used in this thesis is called TPP-2M, which is name after S. Tanuma, C. J. Powell, and D. R. Penn. The TPP-2M equation is a function of electron energy E (eV) and is described by [100]:

$$\lambda = \frac{E}{E_p^2[\beta ln(\gamma E) - (C/E) + (D/E^2)]} \tag{2.10}$$

The parameters for IMFP calculations include the following:

$$\beta = -0.10 + 0.944(E_p^2 + E_g^2)^{-1/2} + 0.069\rho^{0.1}$$

$$\gamma = 0.191\rho - 1/2$$

$$C = 1.97 - 0.91U$$

$$D = 53.4 - 20.8U$$

$$U = N_v\rho/M = E_p^2/829.4$$

$$E_p = 28.8(N_v\rho/M)^{1/2}$$

Here, E_p is the free-electron plasmon energy (in eV).

A Specs X-ray source XR 50M with Al anode (Al Kα 1486.6 eV), Specs FOCUS 500 X-Ray Monochromator, and a Specs PHOIBOS-150 analyzer are equipped for ARXPS in our lab. The overall energy resolution for the XPS spectra is 0.15 eV, which is based on the X-ray source line width. The kinetic energy of a photoelectron is relatively low (<1.5 KeV), so only a low number of electrons which escape from the top 3 to 30 nm of a material are analyzed.

2.3.3 Scanning Tunneling Microscopy/Spectroscopy (STM/STS)

Scanning tunneling microscopy (STM) was developed by Gerd Binnig and Heinrich Rohrer at IBM in 1982, garnering the 1986 Nobel prize for their invention [101]. STM is a technique based on quantum tunneling, which is the phenomenon through which a particle can "tunnel" through a barrier that it classically could not

surmount. STM can image surfaces in real space with the atomic resolution. Figure 2.9 (a) shows images from the omicron STM in our lab, and (b) is a schematic view of an STM setup. When the tip and sample are separated by distances on he order of nanometers and a bias is applied between them, electrons can tunnel through the vacuum separating them. The tunneling current can be monitored. A feedback control is essential in STM to keep the current at some constant by moving the tip height. When the tip moves in plane, the distance between the tip and sample can change, so to keep the current constant, the vertical position of the tip will change by utilizing the feedback control. A typical STM image is recorded by monitoring the tip position, the vertical height z as a function of location (x,y).

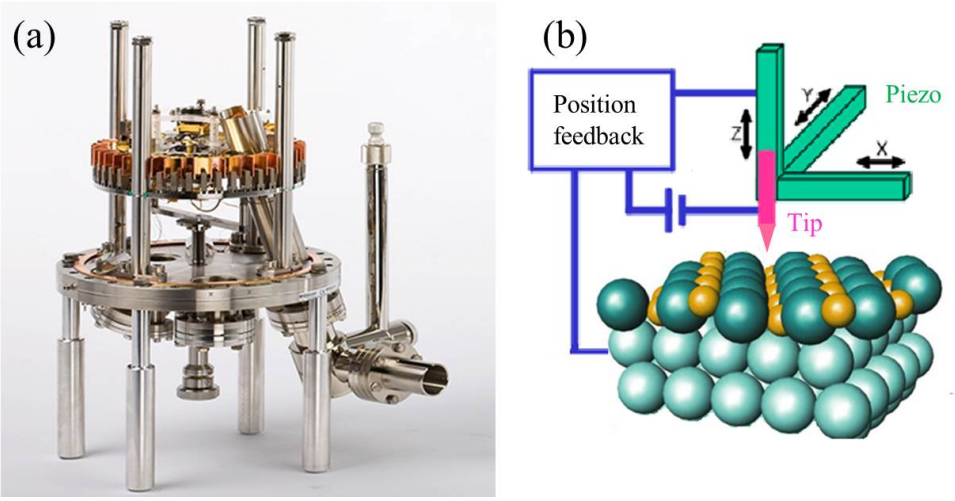

FIGURE 2.9: (a) An image of Omicron VT-STM. (b) Schematic view of STM setup.

In the quantum mechanics, electrons have wavelike states described by wave function ψ. In 1D cases, ψ satisfies Schrödinger's equation:

$$-\frac{\hbar}{2m}\frac{d^2}{dz^2}\psi(z) + U(z)\psi(z) = E\psi(z) \tag{2.11}$$

where $\hbar$ is the reduced Planck's constant, z is the position, m is the mass of an electron, E is the electron energy, and $U(z)$ is the energy barrier. In classical

mechanics, when $U(z) > E$, the particle cannot cross the barrier. However, in quantum mechanisms, the Eq. (2.11) has a solution in this case:

$$\psi(z) = \psi(0)e^{-kz} \tag{2.12}$$

Here, $k = \sqrt{2m(U-E)}/\hbar$. U is related to the work function and any modification to the tunneling barrier due to the crystallographic orientation, sample local topography, tip sample angle, etc. If the applied bias $V \ll U$, $k \approx \sqrt{2m(U)}/\hbar$, and the tunneling probability of an electron behind the barrier of width d can be given by:

$$|\psi(d)|^2 = |\psi(0)|^2 e^{-2kd} \tag{2.13}$$

Then the tunneling current is proportional to the probability of electrons inside the barrier:

$$I \propto \sum_{E_f - eV}^{E_f} |\psi_n(0)|^2 e^{-2kd} \tag{2.14}$$

This negative exponential function of the current I and distance d between tip and sample is the key for the atomic resolution. For example, when $U = 4$ eV, the decay constant k is about 1Å^{-1}. When tip position z changes 1Å, the current decay changes about $e^2 = 7.4$, nearly one order of magnitude in the current. Thus, any topographic height change will be amplified through the tunneling current, which gives atomic resolution for STM images.

In addition to imaging the surface topography, STM allows one to probe the local density of states (LDOS) on surfaces. When the bias V is small enough, at a location z, the LDOS ($\rho_{z,E}$) of the sample is defined as:

$$\rho_{z,E} = \frac{1}{V} \sum_{E-V}^{E} \mid \psi_n(z) \mid^2 \tag{2.15}$$

So that

$$I \propto \sum_{E_f - eV}^{E_f} LDOS(d, E) \tag{2.16}$$

The current depends not only on z but also the integration of the LDOS at an energy window near the Fermi surface in Eq. 2.16, which indicates that STM images are related to both the morphology of the surface and the electronic properties of the surface. Equation 2.16 clearly shows the relation between the tunneling current I, the bias voltage V, and the tip-sample distance z. Therefore, three kinds of spectroscopies can be used: 1) $I - z$ curves with constant V, which can be used to obtain the local work function; 2) $V - z$ curves keeping I constant ; 3) with z constant, scanning $I - V$ curves, which are widely used and reflect any conductance variations over the sample. Further, by applying two different biases, STM can probe the filled states with positive bias, and the empty states with the negative bias [103].

If the derivative of I with respect to the bias V is taken, the following equation can be obtained:

$$\frac{dI}{dV} \propto LDOS(d, E) \tag{2.17}$$

Equation (2.17) shows the capability of STM to probe the electronic properties of sample surfaces. Technically, dI/dV as a function of applied voltage can be obtained by the $1st$ derivative of the I/V curve. The direct and more precise way to detect the dI/dV signal is done using a lock-in amplifier. A small high frequency *sine* signal is added to the bias. This small modulation causes a response in the tunneling current. By using a lock-in amplifier, the first harmonic response frequency can be extracted, which is proportional to dI/dV.

However, dI/dV is V-dependent, which may distort the features in the STM. Stroscio et. al. proposed a simple but effective solution to this problem [102]. They

normalized dI/dV by dividing it by I/V, which yielded $d(lnI)/d(lnV)$, effectively canceling out the V dependence. However, this normalization is both unnecessary and undesirable at small bias, in which case, the I/V curve is well behaved and (dI/dV)/(I/V) is identically equal to unity for ohmic systems and carries no information.

Our variable temperature scanning tunneling microscopy (VT-STM) is a newly designed Omicron combination of STM and QPluse AFM (Atomic force microscopy), which allows imaging of both conductive and insulating surfaces, and can reveal electronic inhomogeneities and local structural reconstructions.

2.4 *Ex-situ* Characterization

By using the previous *in-situ* measurements, we are able to study film surfaces. However, for information from deeper inside the film or near the interface, other techniques are needed. Transport and magnetic measurements using Dr. Rongying Jin's equipment were obtained, and transmission electron microscopy was done at Brookhaven National Lab.

2.4.1 Scanning Transmission Electron Microscopy/Electron Energy Loss Spectroscopy (STEM/EELS)

Scanning transmission electron microscopy (STEM) is a type of transmission electron microscope (TEM) that is widely used to directly image the position of atoms in crystallized samples.

The history of TEM can be traced back to 1925 when Louis de Broglie first theorized the wave-like properties of electrons [104]. The first STEM was realized in 1938 by Baron Manfred von Ardenne in Berlin[105]. In the 1970s, Albert Crewe developed the field emission gun, and created a modern STEM using this technique coupled with a high-quality objective lens [106]. He also demonstrated STEM's ability to image atoms using an annular dark field detector.

An illustration of the STEM instruments used is schematically shown in Fig. 2.10(a). Similarly to optical microscopy, STEM uses an electron beam as the "light" source and a magnetic lens instead of an optical lens. By using a condenser lens, the electron beam can be focused to a small spot, though it is not small enough for atomic resolution. The aberration corrector is essential for further focusing the beam to an ultra narrow spot smaller than 1 Å, which is the main factor limiting the resolution of STEM. By changing the scanning coils, the highly focused electron beam is raster-scanned across the sufficiently-thin material. Various types of scatterings are collected as a function of position.

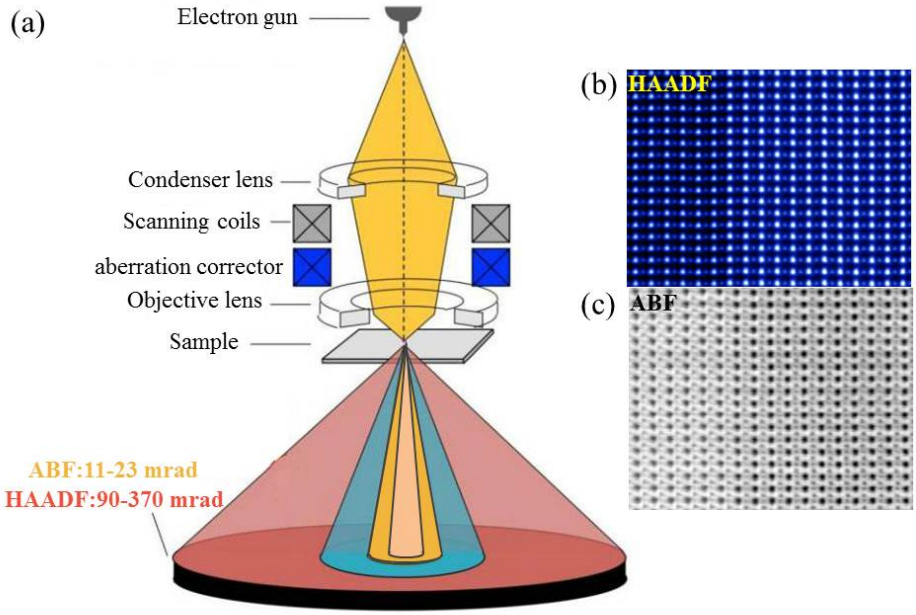

FIGURE 2.10: (a) Schematic view of STEM setup. (b) HAADF and (C) ABF images of LSMO film on STO(001).

High angle annular dark field (HAADF) imaging is widely used in STEM, which is formed by very high angle beams and incoherently scattered electrons in a ring-shaped circumference from 90 to 370 mrad. The image intensity of the HAADF

image is approximately proportional to Z^2, which typically results in easier visualization of heavy elements. Because the collected electrons are incoherent, the atom positions can be directly measured from the images. For many important materials, light elements such as oxygen, nitrogen, lithium, and hydrogen are common components, but these are unable to be identified with HAADF images.

The Annular bright field (ABF) images is another method in STEM, which preferentially receives the ring-shaped circumference from 11 to 23 mrad. Different from HAADF images, ABF images easily and clearly see lightweight elements. However, ABF imaging is less advantageous in some applications due to it's strong dependence on both thickness and focusing, making interpretation of ABF images more complicated.

TEM was originally designed to give structural information about a specimen. However, the interaction between incident electrons and sample allows STEM to also probe chemical information and electronic structure. When electrons travel through a specimen, some of them can be inelastically scattered. Inelastic interactions include phonon excitations, inter and intra band transitions, plasmon excitations, inner shell ionizations, and Cherenkov radiation. An electron spectrometer can be used to measure any changes in the energy distribution of the inelastically scattered electrons, which is the crux of Electron Energy Loss Spectrum (EELS) [107] techniques. The energy loss is due to inner-shell ionizations, which are characteristic for different elements, and this enable EELS to detect elemental components and atomic bonding states in a material.

Cross-sectional STEM samples were cut into $\sim$ 80 nm thicknesses by a focused ion beam (FIB) with Ga+ ion milling, and then nanomilled with Ar+ ions to remove surface damage and further thin the sample to about 50 nm. All the samples were studied under a double-aberration-corrected 200 kV JOLE ARM equipped

with a dual-energy-loss spectrometer. Dural EELS mapping across the interface was collected with a dispersion of 1eV. The STEM conditions were optimized for EELS spectroscopy with a probe size of $\sim$ (spot size 4), a convergence semi-angle of 20 mrad, and a collection semi-angle of 88 mrad. Line-scanning EELS spectra were obtained across the interface with a step size of 0.12 Å, and a dwell time of 0.05 s/pixel.

2.4.2 Physical Property Measurement System (PPMS)

The resistivity of the film as a function of temperature $\rho(T)$ is measured by a commercial Quantum Design Physical Properties Measurement System (PPMS) shown in Fig. 2.11(a). PPMS is designed to perform a variety of measurements, such as determining specific heat, thermal transport, alternating current (AC) susceptibility, and transport measurements.

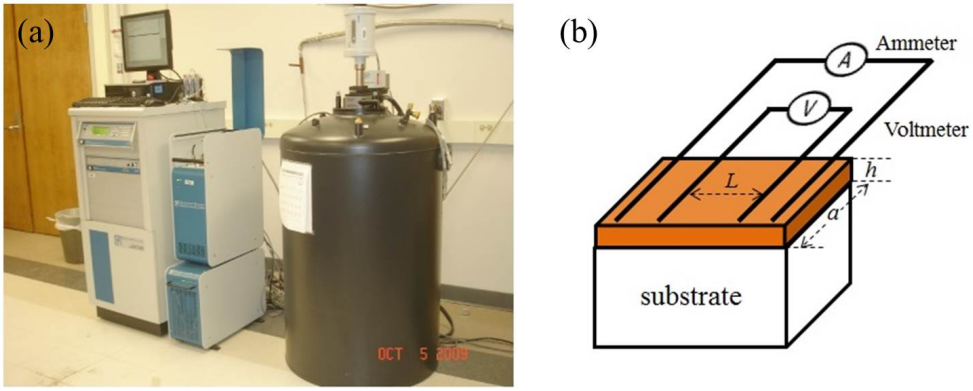

FIGURE 2.11: Instrument of Quantum Design PPMS. (b) Schematic diagram of four probe method.

By using PPMS, the direct current (DC) resistance R can be measured using a four-probe method. The setup is shown in Fig. 2.11 (b), which consists of the probe arrangement, sample constant current generator, and digital voltage. The four probe method is a widely used standard for the measurement of resistivity, due to its ability to ignore contact resistance in the measurement. The film sample

is grown on an insulating substrate with length a and thickness h, which can range from a few to several hundred layers. Four probes are arranged linearly in a straight line, the two outside probes having constant current I passing through and the middle two measuring the potential drop V across distance L. The resistivity ρ of the film is calculated by

$$\rho = R \cdot (a \cdot h)/L = \frac{V}{I} \cdot (a \cdot h)/L \tag{2.18}$$

Compared with two probe methods, four probe measurement results are more accurate and can avoid the influence of ohmic contacts.

2.4.3 Summary

An important condition for modern materials physics and nanoscience is control of materials to atomic dimensions. For complex oxides, Laser-MBE has proven to be a growth technique through which the deposited material can be controlled at the atomic scale. Stoichiometric transfer, high deposition rate, and tunable energy of the arriving particles are parameters which enable us to control the film growth with layer-by-layer growth feasible for various complex oxides to a surface roughness of only one unit cell. ARXPS and LEED can be used to determine the surface chemical composition and structure of the thin films and provide some insight into the their effects on the eventual film properties. For information on the interior, both for chemical composition and structure of the thin films, we need to use STEM/EELS to analyze the samples. The surface morphology and local electronic properties of samples can be studied by using STM , while PPMS enables us to probe properties of the whole film. Combining these $in-situ$ and $ex-situ$ analysis tools, we are able to systemically study and evaluate the properties of thin films in detail.

Chapter 3

Substrate treatment and LSMO film growth

3.1 Introduction and motivation

$SrTiO_3$ (STO) is an insulator with a band gap of 3.2 eV. The structure of STO is cubic perovskite with a lattice constant of a= 3.905 Å. Self-doping with oxygen vacancies or element doping by Nb result in an n-type semiconductor, which makes STO suitable for $in-situ$ analysis to avoid any charging effects. STO is a widely used substrate material for the growth of thin films and heterostructures due to its compatible cubic perovskite structure and lattice constant. Many interesting new properties appear at the interface of STO with other transition metal compounds, including two-dimensional electron gas and superconductivity which appear at the interface between STO and $LaAlO_3$ films [32, 36].

STO (001) has a controllable termination layer with either TiO_2 or SrO. The atomically flat TiO_2 terminated surface can be obtained by using a HF buffer solution etching and $in-situ$ or $ex-situ$ annealing [110]. SrO terminated STO is usually obtained by high temperature annealing [109] or depositing a SrO layer on a TiO_2 (001) surface termination [111].

STO plays an important role in the film growth and resultant properties. A theoretical calculation suggests that a termination layer of STO can change the interface electronic and magnetic properties of STO and $La_{2/3}Sr_{1/3}MnO_3$ interfaces [112]. More importantly, surface defects, polarity, reconstruction, and termination layers could strongly affect the properties of films grown on STO.

$La_{2/3}Sr_{1/3}MnO_3$ (LSMO) is an attractive material for rich physics and potential technological application [14, 15]. LSMO has rhombohedral structure, with an angle of 90.26° and a lattice parameter of 3.88 Å. However, some possible applications

are limited by the LSMO ultra-thin film properties, with different behaviors manifesting depending on the substrates and growth conditions [27, 44, 50, 52, 72, 113, 114]. By studying the relation between the growth modes, oxidation levels, and material properties, the optimized growth conditions for LSMO films were found [75], which enable us to minimize the extrinsic influences on the LSMO properties and probe more intrinsic characteristics.

In this chapter, we investigate the influence of growth and oxygen concentration on the transport properties of LSMO films grown on STO. Epitaxial oxide thin film growth requires the use of crystalline substrates. Achieving atomically flat substrates is essential for high quality film growth. In section 3.2, different treatments of STO are presented, and the best treatment of TiO_2 terminated STO (001) is determined using ARXPS and STM. The growth and structural properties of LSMO films on STO substrates are described by using experimental tools XRD, RHEED, and STM in section 3.3, which also includes transport studies of these films.

3.2 The treatment of $SrTiO_3$ substrate

In this thesis research, Only LSMO thin films grown on STO(001) were systematically studied. STO was chose as substrate because STO is cubic (a=3.905Å) with only 0.5% lattice mismatch with LSMO (a=3.88 Å). For the transport and magnetic measurements, the substrates used were non-doped STO. For the XPS, LEED, STM/STS, and STEM/EELS measurements, 0.1wt% Nb doped STO was used as the substrate. All STO substrates are single crystals bought from CrysTec GmbH of Germany, which have a size of 5 mm × 5 mm × 0.5 mm.

To get an atomically flat substrate, STO was sonicated in acetone for 2 minutes, then Ethanol for 2 minutes, then Milli-Q water for 2 more minutes. The sample is then dried using ultra pure N_2 gas and then etched in a buffer NH_4FHF (BHF)

solution (from Alfa Co.) for 30s. Finally, the sample is dried again and annealed in the vacuum chamber or tube furnace. To study the two different annealing methods, we studied and compared the morphology and surface chemical composition of STO with different treatments.

First, we annealed STO in the growth chamber with 10^{-4} Torr Ozone at different temperatures. When the annealing temperature increased to about 900 °C, the STO surface morphology changed, showing straight step edges with the step height $\sim$ 0.39 nm, as seen in Fig. 3.1 (a) and (b), which suggest that STO annealed in the chamber has a single termination.

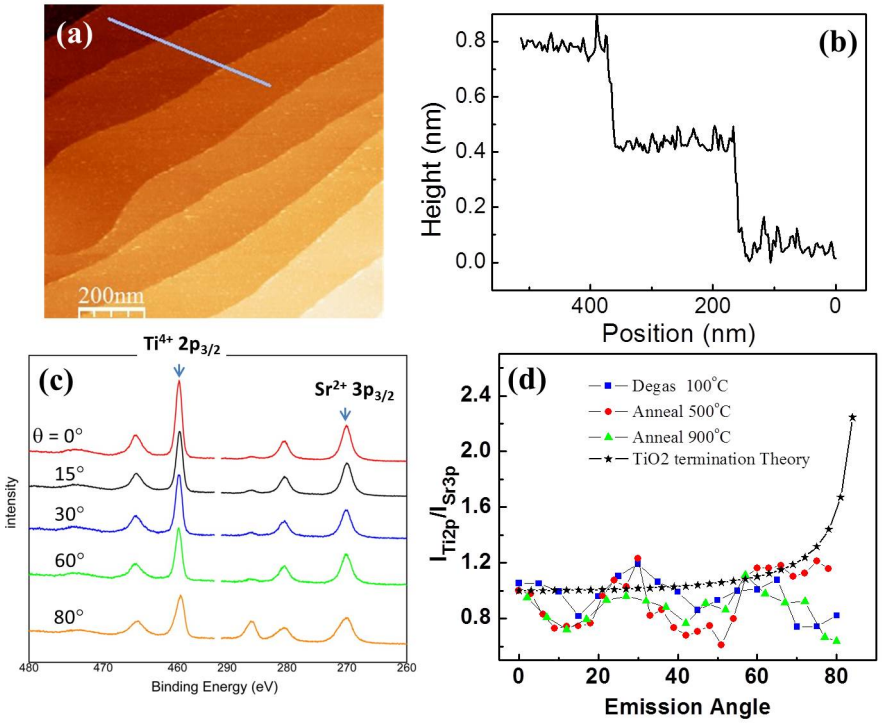

FIGURE 3.1: (a) STM image and (b) height profile of STO annealed at 900 °C for 1 h with 10^{-4} Torr Ozone. (c) Angle resolved spectra of Ti 2p and Sr 3p peak. (d) Angle dependence of intensity ratios Ti2p/Sr3p, degassed in UHV for 1 hr at 100 °C (Rectangle), and annealed in 10^{-4} Torr Ozone for 1 hr with 500 °C (circular) and 900 °C (triangle). The pentagram is the theory result of STO with TiO_2 termination.

To study chemical composition of STO, ARXPS was performed with the STO substrate. The actual data collection was taken with an angle step of 5°. Selected raw data with 0°, 15°, 30°, 60° and 80° are shown in Fig.3.1(c). From the raw data, for different angles, the intensity ratio of Ti2p/Sr3p can be determined, which can be plotted with the angle dependence of these intensity ratios in Fig.3.1(d). Figure 3.1(d) shows that the change in intensity for different core levels are not monotonic, but rather have a sudden change at 18.4 °, 26.5 °, 45 °, and 63.4 ° , which is related to forward scattering contributions based on the crystal structure.

TABLE 3.1: Parameters to calculate the IMFP of characteristic curves for STO.

Valence electrons number N_v	24	Band gap E_g (eV)	3.25
Density ρ ($g.cm^{-3}$)	5.12	Molecular weight M (g/mol)	183.49

TABLE 3.2: List of parameters of Sr 3p, Sr 3d, Ti 2p and O 1s core levels for STO ARXPS calculation.

Element	Shell	Cross section σ	Mean free path λ (Å)	Transmission coefficient T
Sr	3p	6.62	22.85	40.42
Sr	3d	5.05	24.80	39.10
Ti	2p	7.81	20.07	42.56
O	1s	2.92	19.01	43.30

For TiO_2 terminated STO, the angle dependence of intensity ratios Ti2p/Sr3p can be calculated by Eq. 2.9. First, to calculate the inelastic mean free path (IMF-

P), Table 3.1 contains the related parameters needed. Combing Equation 2.10 and Table 3.1, the IMFP for different cores of STO are calculated and list in Table 3.2, which includes other parameters for relative intensity ratio calculation.

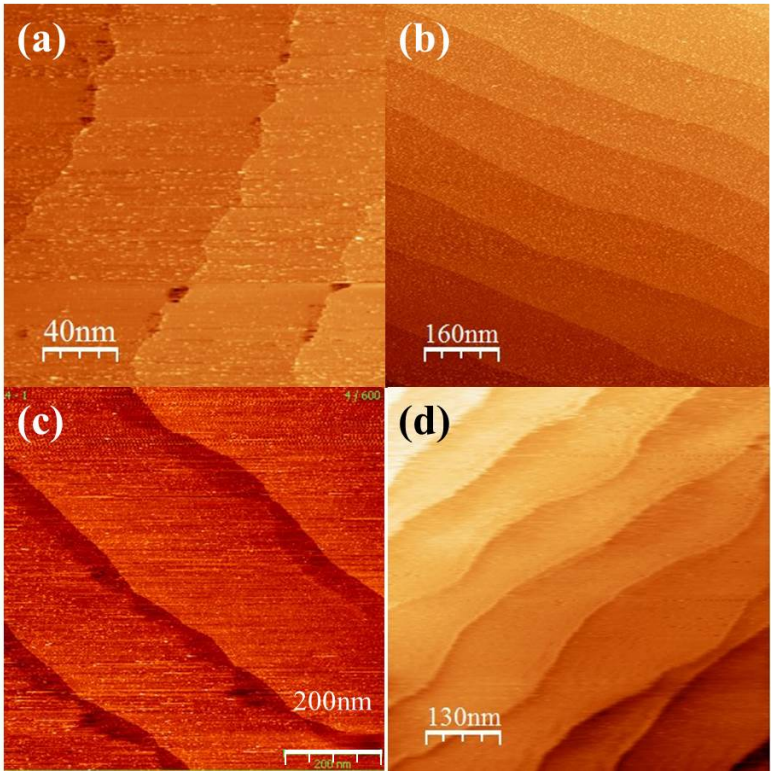

FIGURE 3.2: The morphologies of STO substrates are annealed at different temperature (a) 800 °C (b) 900 °C (c) 950 °C and (d)1000 °C.

For TiO_2 terminated STO, the theory calculated angular dependence of the intensity ratio of Sr3p/Ti2p is drawn as open pentagram in Fig. 3.1 (d), which shows obvious increasing at larger emission angles. Different from the theory result, experimental Ti2p/Sr3p shows a slight drop at larger emission angle, which is likely due to missing Ti or partially left over Sr on the surface. One group reported that TiO_2 termination of STO can be achieved by annealing STO at 750 °C with 7.5 $\times$ 10^{-5} torr O_2 [108]. Although our STM pattern and line profiles also suggest that STO treated at 900 °C has a single termination, ARXPS demonstrates that STO

annealed in vacuum chamber with a low oxygen/Ozone environment cannot have perfect TiO_2 termination, as it is substantially Ti deficient.

To get better TiO_2 terminated STO, we then attempted to anneal the substrate in the furnace with an O_2 base pressure of $\sim$ 1.45 PSI for 3 hr, with warming and cooling at a rate of 100 °C/h, and then degas it in the UHV chamber with $\sim$ 300 °C before finally preparing for STM and ARXPS measurements.

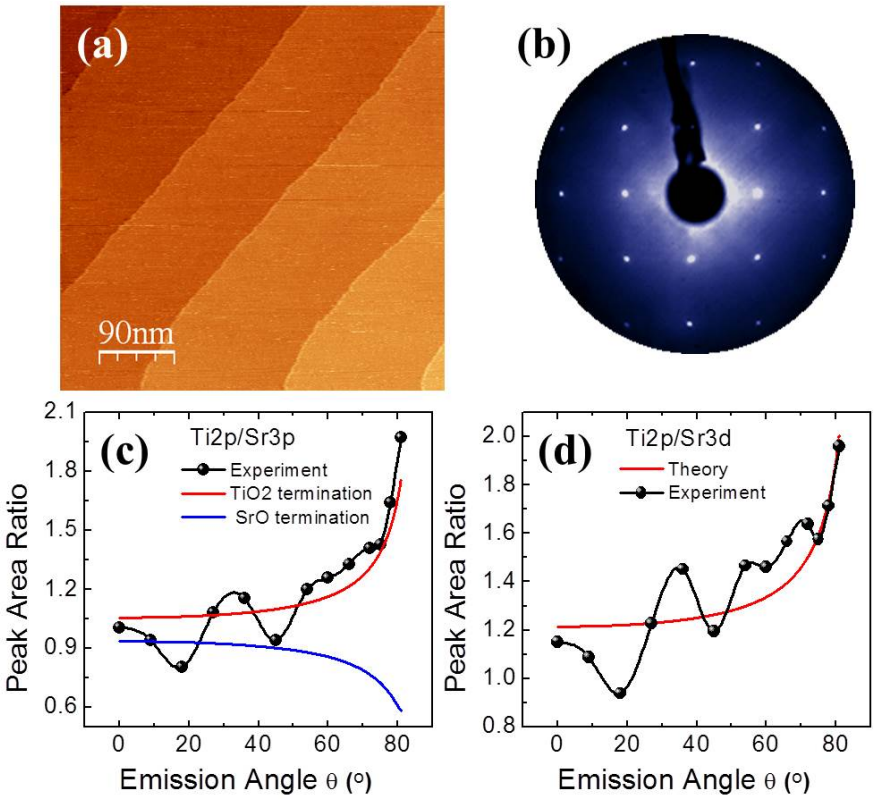

FIGURE 3.3: Surface morphology, structure and termination characterizations of STO $ex-situ$ annealed at 900 °C for 3 hr with $O_2 \sim 1.45$ PSI. (a) STM image; (b) 1×1 LEED pattern; (c) and (d)Experimental data and theoretical calculation based on TiO_2 or SrO termination of the angle dependent intensity ration of Ti2p/Sr3p and Ti2p/Sr3d.

The obtained surface morphologies of STO with respect to different annealing temperatures are displayed in Fig.3.2. For STO annealed at 800°C for 3 hours, the step edge is still not straight shown in Fig.3.2 (a), indicating that an annealing

temperature of 800 °C is not enough. When the substrate annealing temperature was increased to 900 °C, the step edge straightened out, as seen in Fig.3.2 (b). However, when the annealing temperature keeps increasing, large-scale STM images of STO (c) and (d) show obvious low-lying regions with about 0.5 u.c. height difference along the terraces edging, which indicates the appearance of local SrO termination [109].

For the STO substrates $ex-situ$ annealed with the high O_2 pressure, 900°C is the best treatment temperature. The surface morphology clearly shows more straight terrace step edges with the atomically flat surface shown in Fig.3.3(a). There is no reconstruction of the STO surface, which is confirmed by the sharp 1 $\times$ 1 LEED pattern in Fig.3.3 (b). To further check the termination, 900°C treated STO is characterized by ARXPS, and the results are shown in Fig.3.3 (c) and (d).

From the raw ARXPS date for STO, the intensities of different core peaks (Ti2p, Sr3p, and Sr3d) can be calculated, which further can be used to calculate experimental results for the angle dependent intensity ratio of Ti2p/Sr3p (black) shown in Fig. 3.3(c). Different from the $in-situ$ treatment of STO, for the $ex-situ$ treated STO, the ratio of Ti2p/Sr3p increases at larger emission angle, and the drops in the ratio around 18 ° and 45° are due to the forward scattering effect. Comparing the experimental results with the theoretical calculation results of the angle dependence of Ti2p/Sr3p with TiO_2 (red line) or SrO termination (blue line), we can see that the 900 °C treated STO (001) obviously has TiO_2 termination. The experimental result and theoretical calculation of Ti2p/Sr3d as the function of emission angle are also shown in Fig. 3.3(d), and these also support a TiO_2 termination conclusion.

In summary, we investigated the surface of HF-etched $SrTiO_3$ (001) substrates. It is found that $in-situ$ annealed STO with lower Ozone pressure has a Ti deficient

TiO_2 termination surface. Although, after treatment at 900 °C inUHV chamber with lower pressure Ozone, STO shows an atomically flat surface in STM and the line profile shows a 1 u.c. terrace height difference, ARXPS shows an obvious Ti defect, which indicates that STO treated with low gas pressure cannot achieve both the correct stoichiometry and an atomically flat surface at the same time. To achieve better substrates, $ex - situ$ annealing of STO with a higher O_2 base pressure at $\sim$ 1.45 PSI was performed. After a 900 °C treatment temperature, the surface of STO was checked using STM imaging. Further, the surface shows a 1×1 LEED pattern with no reconstruction. By comparing the experiment results and theory calculations, ARXPS also shows that the $ex - situ$ annealed STO is terminated with TiO_2 without any Ti deficiency, which is different from $in - situ$ low O_3 pressure treated STO.

3.3 High quality LSMO film growth

In this section, the growth of the LSMO thin films is described. With perfect TiO_2 terminated STO, obtained with the method described in the previous section, the growth of the thin films using PLD is described. $In - situ$ RHEED measurements were used to reveal the two-dimensional (2D) layer-by-layer growth mode for LSMO film growth. Finally, the surface morphology was further characterized by STM and LEED, which shows smooth and well ordered surfaces.

3.3.1 LSMO film growth

LSMO films were deposited on TiO_2 terminated STO (001) by using our Laser-MBE system with a stoichiometric LSMO target. A KrF excimer laser (248 nm) at a laser frequency of 3 Hz and laser energy of 1 J/cm^2 was used. The spot size of the laser beam on the target was 0.021 cm^2. During the growth, a mixture of 99% O_2 + 1% O_3 gas was applied.

To obtain layer-by-layer growth for LSMO films, an optimized growth temperature window was explored and was found to at $\sim$ 700 °C. When higher temperature is used for film growth, the RHEED oscillation became unstable after a short time. While, for the lower growth temperature, the film growth became 3D, which indicates poor crystal quality of the films. As the results, the LSMO growth temperature was chosen to be around 700 °C, which maintains a layer-by-layer growth mode.

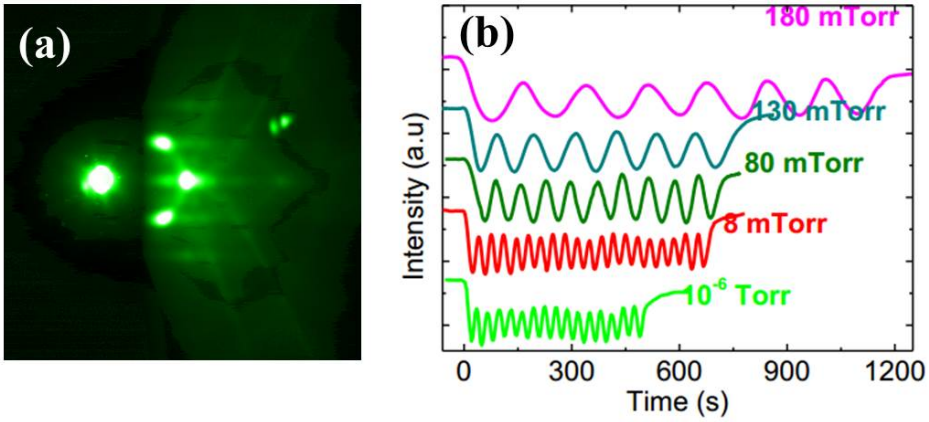

FIGURE 3.4: (a) RHEED pattern of STO before film growth. (b) RHEED intensity oscillation pattern at various oxygen partial pressures.

With the optimized growth temperature, layer-by-layer epitaxial growths of LSMO films were obtained. Figure 3.4 (a) shows the 2D RHEED diffraction pattern for the STO substrate. By monitoring the variations in RHEED intensity, the LSMO film growth dynamics can be studied. A layer-by-layer growth mode was obtained for all pressures ranging from high vacuum (10^{-6} Torr) to high pressure around 130 mTorr, which can be observed in the RHEED intensity oscillation in Fig. 3.4 (b). The oscillatory behavior of RHEED also demonstrates that, keep-

ing other conditions the same, higher gas pressure results in slower LSMO growth rates, which is read from the period of the intensity oscillations.

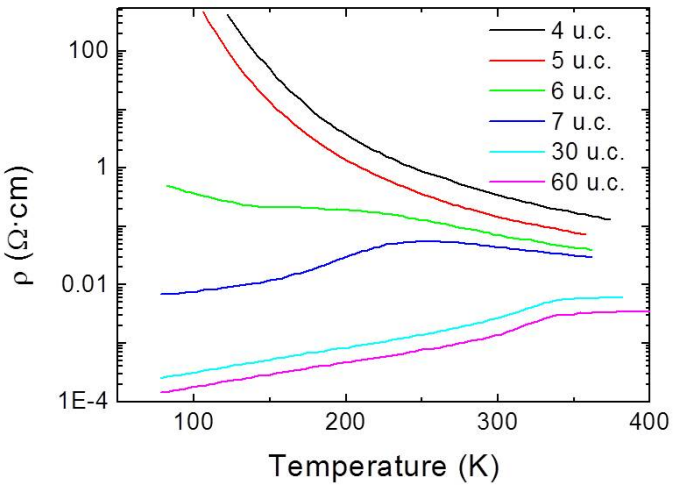

FIGURE 3.5: Temperature dependent resistivity for LSMO films with different thicknesses grown at 80 mTorr. [75]

For the LSMO films grown with 80 mTorr pressure, the temperature dependence of the resistivity for variable films thicknesses is given in Fig. 3.5. Thicker films show a bulk-like metallic behavior below $\sim$ 360 K, approaching or achieving the resistivity of the bulk in the thicker samples, similar to other group results [27]. The Curie temperature of the films increases with film thickness up to $\sim$ 360 K for the 60 u.c. film, which is close to the Curie temperature $\sim$ 369 K in the bulk crystals. When the film thickness decreases, the LSMO film resistivity increases drastically for the whole temperature range. For 6 u.c. LSMO film, the continuous resistance decreases as we increase the temperature, which indicates that the 6 u.c. LSMO film is insulating. However, for 7 u.c. LSMO, the resistivity behavior is completely different from 6 u.c., where now the LSMO resistivity decreases with the temperature below around 250 K, indicating metallicity.

LSMO film transport properties strongly depend on the growth pressure and film thickness. LSMO films with different pressures are grown, and the transport properties are measured. Our group's previous results show that, for certain growth pressures, LSMO films become less metallic with a decrease in thickness [75]. Below a certain critical thickness (t_c), LSMO films are "dead" and become insulators. Higher Ozone growth pressures enhance the conductivity and favor a metallic ground state, through which it can be concluded that oxygen deficiency plays an important role in the dead layer, and drives the films to be more insulating. Although the dead layer decays with increasing growth pressure, the dead layer cannot disappear, and is minimized at 6 u.c., which can be achieved with a growth pressure of $\geq$ 80 mTorr. When the growth pressure is $\geq$ 80 mTorr, oxygen deficiency is not the key issue for LSMO films. Due to this optimization, 80 mTorr is chosen as the oxygen pressure for our film growth.

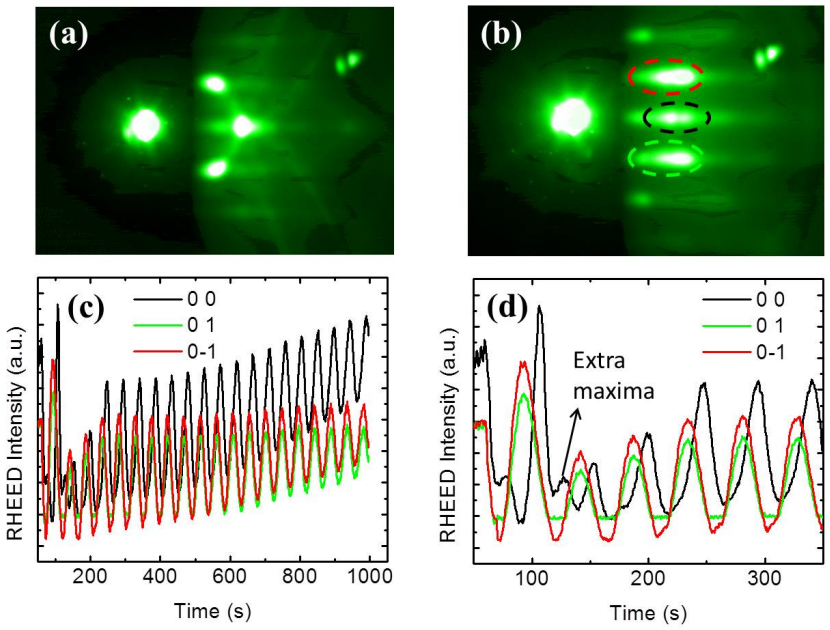

FIGURE 3.6: (a) RHEED images in the (100) direction for STO substrate. (b) RHEED images in the 20 u.c. LSMO films. (c) Typical RHEED intensity oscillations for 20 u.c. LSMO growth on STO (001) (d) Zoom in of the RHEED oscillations from (c) .

Figure 3.6 shows the experimental RHEED results for the STO substrate and 20 u.c. LSMO film growth. Figure 3.6 (a) is a typical experimental 2D RHEED pattern obtained from a single crystal STO (001), which clearly shows a good crystallized substrate and flat surface. During film growth, by tracking the reflection spots in Fig. 3.6 (b), the RHEED oscillations can be obtained, which is shown in Fig. 3.6(c). Based on the RHEED oscillation, the growth rate is calculated to be 46.5 $\pm$ 0.5 s/u.c., which strongly depends on the growth conditions. A significant phase shift in the RHEED oscillations between the specular spot at (0,0) and the other two spots at (0, 1) and (0, -1) can be observed. Given the same incident electron energy and growth conditions, phase shift depends on the incidence angle [115].

If we closely examine the first layer growth of LSMO film in the RHEED oscillations in Fig. 3.6 (d), we can see that an extra maxima appears between two oscillation peaks of the specular spot, which can only be observed within a small region of the glancing angle of the incident beam. To better understand the extra maxima, quantitative results for each peak and the extra maxima are obtained and shown in Fig. 3.7. Within the error bar, for different layers, the growth times (i.e. specular peak positions) are the same at about 46.5 s. For the extra maxima, the growth time, which is calculated by the difference between the current maxima and previous peak, seems to gradually change with thickness. However, considering that the time when oscillation minima appear is near the extra maxima, and therefore affects the position of the maxima, the smallest peak at position 3 u.c. provides the most trustworthy extra maxima time of 23.1 $\pm$ 1 s, which is about half of the 1 u.c. growth time. Although extra maxima were observed, the extra maxima for LSMO film growth only appear in the first several layers, when compared with the dynamical RHEED theory calculation and explained as a perfect monolayer-by-monolayer growth mode [115]. The RHEED pattern also changes

dramatically, which could be related to the mixed termination, though this aspect requires further study.

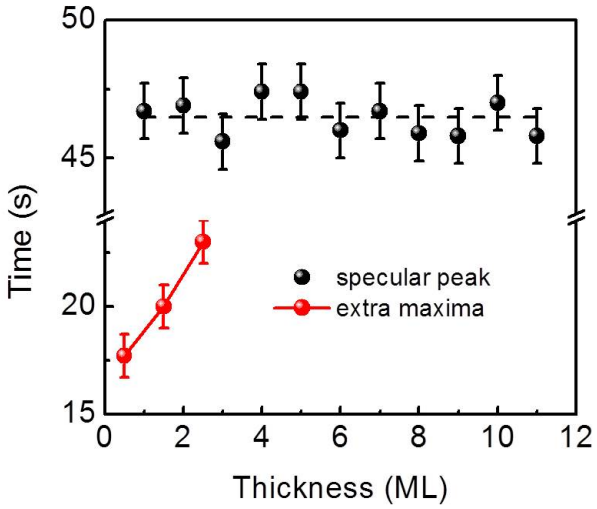

FIGURE 3.7: Specular and extra maxima growth time for different thicknesses.

3.3.2 LSMO film quality characterization

The optimized LSMO film growth conditions are determined to be $\sim$ 700 °C with 80 mtorr mixed Ozone gas. In this section, the high quality of our LSMO films are demonstrated, which in turn minimizes extrinsic influences on films properties.

As mentioned above, the transport measurements in Fig. 3.5 already show a dead layer of 6 u.c., which currently is minimized for LSMO films grown on a STO (001) substrate. Higher gas pressure cannot further reduce the thickness of dead layer, which shows that oxygen deficiency does not drastically influence LSMO films grown under optimized conditions.

In addition to the layer-by-layer growth mode for LSMO films being confirmed through RHEED oscillations in Fig. 3.4, the surface morphology of the LSMO thin films were further investigated by STM images. Different from transport measurements, which measure LSMO films grown on non-doped STO, for the STM

scanning, a more conductive 0.1wt% Nb-doped STO substrate was used. Figure 3.8 (a) shows the surface morphology of a 12 u.c. LSMO ultrathin film. Clear terraces with a width of about 70 nm are observed. A single step height of $\sim$ 0.39 nm can be found in our STM image, indicating a single termination surface. For layer-by-layer growth, it is difficult to determine the exact moment to stop growth, which can cause some small extra patches to be found on the surface, as seen in our image.

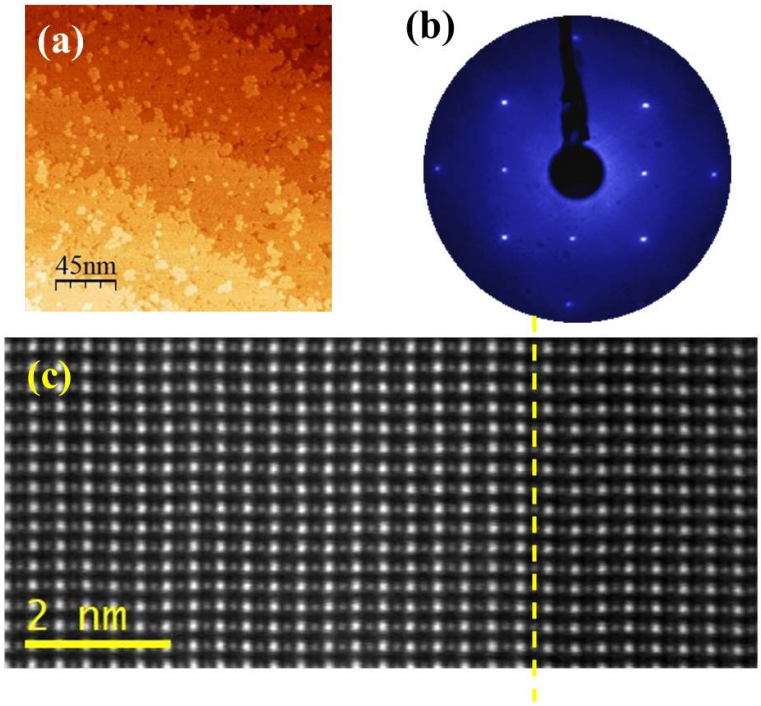

FIGURE 3.8: (a) The STM image of the surface morphology of a 12 u.c. LSMO film. (V=1.0 V, I = 20 pA, T = 300 K) (b) LEED pattern of 12 u.c. LSMO film at RT at 95 eV. (c) HAADF-STEM image near the interface of 40 u.c. LSMO grown on STO (001) taken along [110]. The dish line indicates the interface between LSMO film and STO substrate.

Figure 3.8 (b) depicts the LEED pattern at 95 eV for an LSMO film, which demonstrates the good crystallization of the film. The 1×1 characteristic and lack of any reconstruction pattern can be observed on the LSMO films' surface. The

microscopic structure was further investigated by STEM in Fig. 3.8 (c), which is part of a high-resolution TEM image of the cross-sectional structure of 40 u.c. LSMO films grown on STO (001). The film was crystalline and the LSMO/STO interface is seen to be very sharp. Looking at the entire image, no obvious peak splitting due to the small mismatch was found, indicating that the LSMO film is very high quality and uniformly epitaxial.

3.4 Summary

In this chapter, we investigated different treatments to achieve the most atomically flat TiO_2 termined STO (001) possible. Before annealing, the STO substrate was cleaned and HF etched. It is found that, for $in-situ$ treatment with low oxygen/ mixed Ozone gas pressure, the annealed STO substrate has an oxygen deficient TiO_2 termination surface. This surface is not stable, and so the 1×1 surface easily reconstructs when the annealing temperature is raised above 500 °C. Using ARXPS, we can prove that, different from the $in-situ$ treatment, the $ex-situ$ annealing with high oxygen pressure can keep the film stoichiometric and maintain an atomically flat substrate surface at the same time, making it the better treatment for STO (001) substrates.

We also optimized the growth conditions of LSMO films on STO substrates by changing parameters such as growth temperature and Ozone pressure. It is found that an ideal layer-by-layer growth can be achieved with a growth temperature of $\sim$ 700 °C. At the growth temperature of $\sim$ 700 °C, a minimized dead layer of 6 u.c. can be achieved by growing with mixed Ozone at $\geq$ 80 mTorr. With these optimized growth conditions, the atomically flat surface of LSMO films is confirmed by STM, which is also proved to be no reconstruction by LEED. The STEM results further demonstrate the high quality of LSMO films, which are well-crystallized and no obvious disorder and dislocation. By using this optimized substrate treatment and

growth process, we are able to minimize the extrinsic effects on LSMO films, which will allow us to further investigate the intrinsic properties of LSMO films.

Chapter 4
Layer-by-layer composition

4.1 Introduction and motivation

In the last few decades, it has become increasingly clear that surfaces, interfaces, thin films, and heterostructures of transition metal oxides (TMOs) display a rich diversity of fascinating properties that are related, but not identical, to their bulk phenomena [116, 42, 117, 118]. New states of matter, which are inaccessible in the corresponding bulk compounds, have been discovered at interfaces. Examples include surface-tailored purely electronic Mott transitions [119, 120], interface-induced superconductivity [32], two-dimensional electron gases [36], orbital reconfiguration [121], and interface-controlled ferroelectric polarization [122], as well as dimensional crossover driven metal-insulator transitions [33, 123]. Such emergent phenomena herald a possible new generation of oxide-based electronics [124]. Oxide devices involve the fabrication of thin films, superstructures, and junctions. The design of virtually all electronic devices begins with an understanding of interface barrier formations, electronic/magnetic structures, and control of the structure, composition, and interface [125].

Understanding the nature of the emergent phenomena in these artificially structured materials requires thorough study of their structure-property relationships. While the essential starting point should be the characterization of lattice structure and chemical composition, the termination (final atomic configuration) of each deposited layer, and possible induced distortion at the interfaces, as well as imperfections such as vacancy, defects, impurity, etc., are crucially important for emergent properties. Even in the most studied TMO system, $LaAlO_3/SrTiO_3$, many proposed mechanisms for these observed phenomena are still hotly contest-

ed, including polarity effect [19], cationic mixing [126, 127], and intrinsic doping due to the existence of oxygen vacancy [128, 129], as well as thickness-dependent polar distortion [130] and the exponential decay of lattice relaxation effects [131]. The exciting observations, as well as many remaining unresolved issues, point to a consensus that many TMO interfaces are more complex than previously realized, and motivate new approaches to both materials growth and characterization.

In this chapter, we report on our study on the chemical composition variation with atomic layer precision in ultrathin films of doped manganite material $La_{2/3}Sr_{1/3}MnO_3$ (LSMO) using a combination of *in*− and *ex*− *situ* microscopy and spectroscopy. Our results reveal that there is a substantial increase in the Sr concentration from its bulk value both at the interface and in proximity to the film surface. The deviation at the interface with the STO (001) substrate is mainly due to single unit cell intermixing, while the deviation in proximity to the film surface is because of Sr surface segregation. As the substrate surface is terminated, the LSMO film surface experiences a gradual self-organized conversion from a MnO_2 to (La/Sr)-O layer termination with increasing thickness. Such layer-by-layer variation in composition and its dependence on film thickness should have an immense impact on the physical properties of epitaxial films and heterostructures.

Manganite perovskites have been extensively studied for more than half a century due to their potential applications in solid electrolytes, magnetic sensors, spintronics, and even catalysts, as well as due to their rich physics such as colossal magnetoresisitance, charge ordering, half-metallicity, and phase separation, all of which are related to the close coupling among the charge, lattice, orbital, and spin [8, 132, 133, 134]. One particularly interesting manganite is LSMO because of it has the highest Curie temperature T_c ($\sim$ 369 K in the bulk crystals) and the most itinerant electronic character among the manganites [135], showing functionalities

for promising technological applications. Ironically, for LSMO ultrathin films, its metallic states and ferromagnetic ordering are greatly suppressed [136, 27], which is very different from the bulk and is usually referred to as a 'dead layer'. The critical thickness of the dead layer depends on the strain and oxygen stoichiometry [75]. However, the intrinsic origin of the dead layer still remains highly controversial. It has been suggested that the dead layer is caused by nanoscale phase separation due to spatial structural inhomogeneity [137], but why such inhomogeneity occurs in ultrathin films only is unclear. Others have suggested that the dead layer is related to orbital reconstruction because of the MnO_6 octahedron distortion at the interface [44, 138]. Due to the rich doping-dependent phase diagram including the metal-insulator transition, ferromagnetism, antiferromagnetism, and charge ordering in $La_{1-x}Sr_xMnO_3$ [76], chemical composition variations can be vital in understanding the different properties between films and the bulk. Although Sr segregation at surfaces has been suggested [66, 139, 140, 141], there is no clear picture about the layer-by-layer chemical composition profile in LSMO films.

4.2 LSMO film interface composition from TEM

By using PLD, epitaxial LSMO films with different thicknesses were deposited on atomically flat TiO_2 terminated 0.1 wt% Nb-doped STO (001) substrates. The growth conditions for high-quality LSMO films are discussed detailed in the chapter 3, the quality of which has been confirmed through RHEED, LEED and STM.

The well-ordered structure and high quality of the LSMO films can be further confirmed by scanning transmission electron microscopy (STEM). Figure 4.1(a) displays high-angle annular dark field (HAADF) STEM image taken along [110] for 40 u.c. LSMO. These images are atomic number(Z)- contrast images, powerful for structure determination and defect identification such as dislocated cores. For LSMO, the atomic numbers are: La(57) > Sr(38)>Mn(25)> Ti(22) > O(8). Under

these conditions, the bright dots observed in the right part of Fig. 4.1(a) correspond to the projection of LSMO films. The left part of STEM figure depicts the STO substrate. From the STO portion, it is worth noticing that these two types of atoms give rise to the different kinds of contrast dots. The brighter dots seen in the STO exclusively correspond to the projection of Sr atomic columns, whereas Ti columns are imaged very weakly. Similarly, for the LSMO films, the bright dots correspond to the projection of Sr/La atomic columns, while the weak dots are Mn atoms.

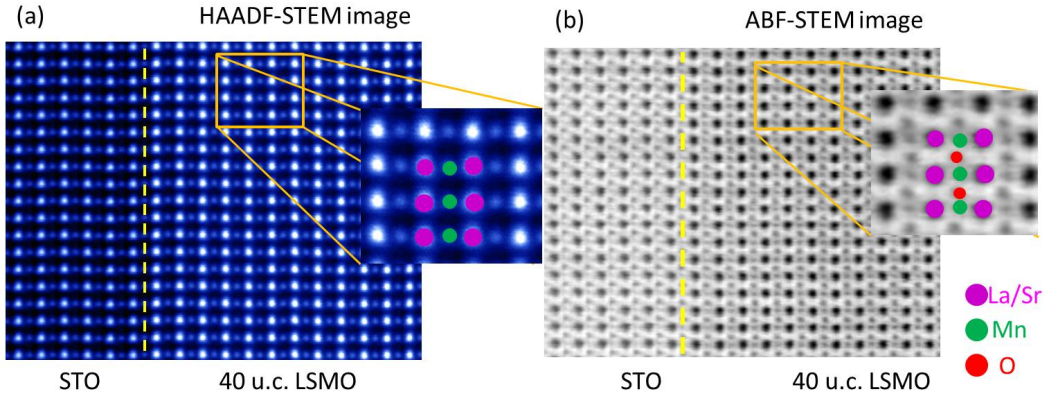

FIGURE 4.1: (a) HAADF-STEM image and (b) ABF-STEM of 40 u.c. LSMO grown on TiO_2 terminated STO interface along [110]. A zoom-in ABF-STEM (Right) images and a structural model from the marked area shows the position for La/Sr, Mn and O atoms.

Although the light element O cannot be observed in HAADF-STEM images, both light and heavy element can be imaged through ABF-STEM, as shown in Fig. 4.1(b). By comparing with the HADF-STEM images, we can are clearly see the extra atoms in the ABF images, which correspond to the O atoms. The right inset is a zoom-in image from the marked area. For the marked area, a structural model with the position for La/Sr, Mn, and O atoms is also given, which shows that the Mn and O atoms are not along a straight line nor is the Mn-O bond angle 180^o.

Both the HAADF- and ABF-STEM images in Fig. 4.1 solidly confirm the continuity of the perovskite stacking sequence without obvious dislocation or defect by surveying over different areas and films. We also checked 8 u.c. and 4u.c. LSMO films grown on STO in the [100] direction in Fig. 4.2, both of which still show an ordered structure. For all HAADF-STEM images, the unambiguous Z-contrast difference in the brightness of imaged A-site atoms (Sr in STO side vs. La/Sr in LSMO side) indicates atomically sharp interfaces between the STO and the LSMO films.

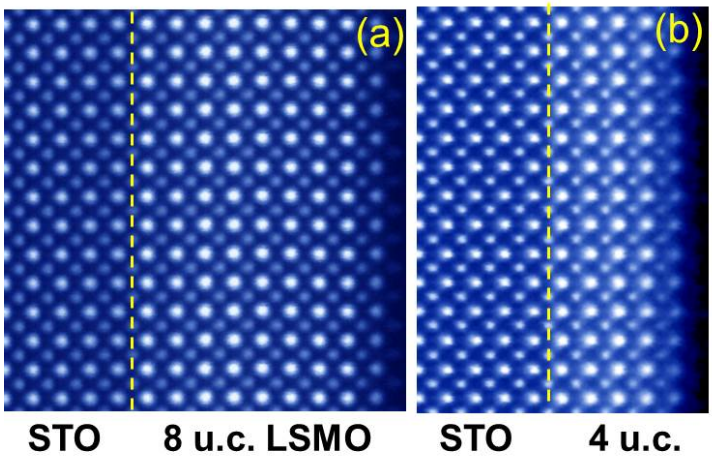

FIGURE 4.2: (Color online) HAADF-STEM image for La, Sr, Ti and Mn of LSMO/STO interface for (a) 8 u.c. taken along and (b) 4 u.c. taken along [100], respectively.

To achieve more quantitative interface concentration results, electron energy loss spectroscopy (EELS) is applied to the LSMO films. After background subtraction and de-convolution for removing the multi-scattering effects, the La $M_{4,5}$, Sr $L_{2,3}$, Mn $L_{2,3}$ and Ti $L_{2,3}$ edges of EELS spectra were integrated to provide elemental profiles, which are superimposed onto the corresponding atomic sites in the HAADF images shown in Fig. 4.3. Here, (a), (b), (c) and (d) are results for 4 different local areas of one same sample.

The stacking sequence near the LSMO/STO interface is the first information obtained from EELS in Fig. 4.3. In the previous section, the HADF-STEM images demonstrated the continuity of the perovskite stacking sequence of LSMO films on the STO substrate. As a result, there are two possible configurations: (1) ...-SrO-TiO_2-(La/Sr)O-MnO_2-... and (2) ...-TiO_2-SrO-MnO_2-(La/Sr)O-... At the interface of 8 u.c. LSMO/STO, the La signals (blue) propagate further into the interface than the Mn signals (purple), demonstrating that all LSMO films have stacking sequence ...-SrO-TiO_2-(La/Sr)O-MnO_2-... at the interface. This result is consistent with the substrate treatment which achieved TiO_2 terminated STO.

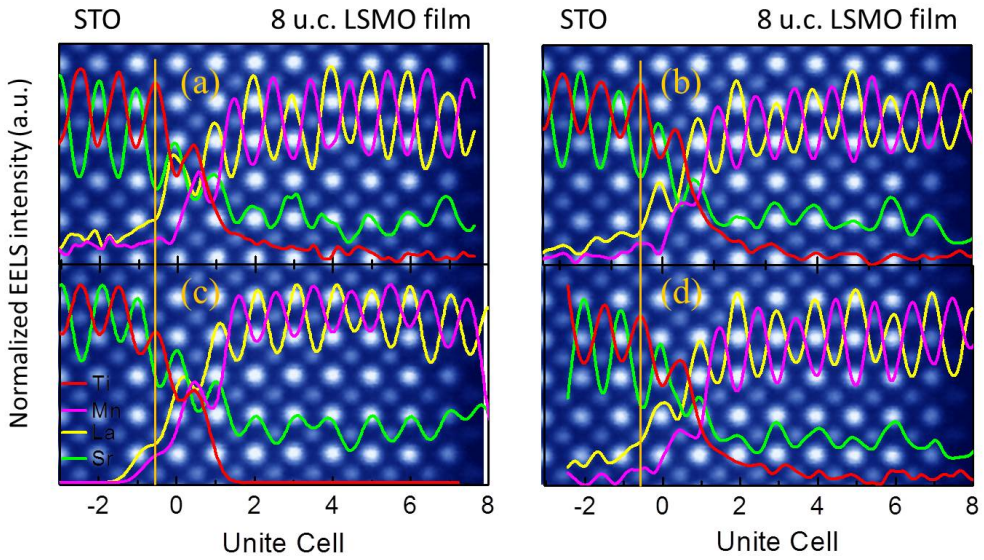

FIGURE 4.3: Profiles of chemical composition as a function of distance for 4 different areas of the 8 u.c. LSMO/STO interface extracted from the La-M edge, Ti-L edge, and Mn-L edge.

Although very sharp interfaces are observed in the HADF-STEM images in Fig. 4.1 and Fig. 4.2, the elemental profiles still show a 1 - 2 u.c. interfacial intermixed region and a significant deviation of Sr concentration at the interface. For the B-site, about 20% Mn is detected in the TiO_2 termination layer at -0.5 unit cell

(u.c.); about 45% and 15% Ti intermixes into the first and second MnO_2 layers with positions 0.5 u.c. and 1.5 u.c. respectively.

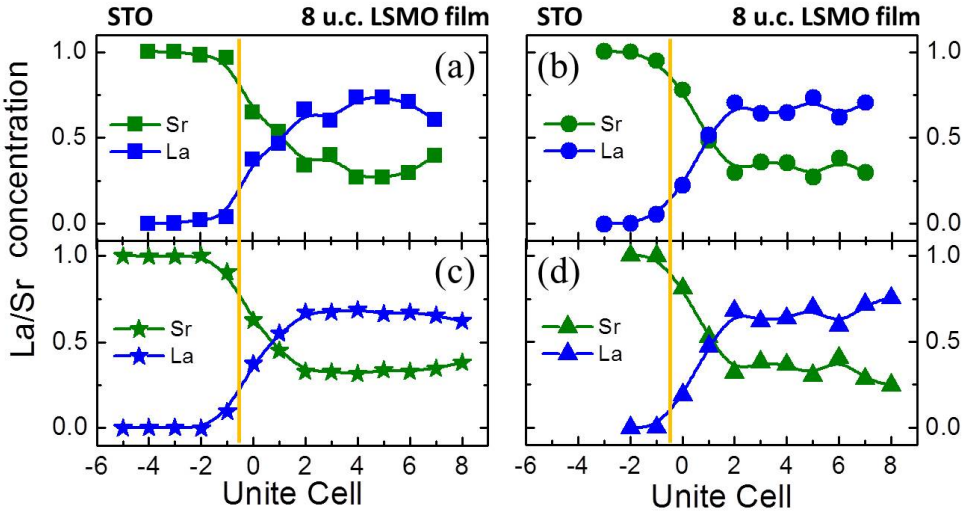

FIGURE 4.4: (Color online) The concentration profiles for La and Sr as a function of distance (unit cells) from the interface obtained from Fig4.3.

To quantitatively analyze the Sr/La ratio evolution, the atomically resolved concentrations are derived from the elemental intensity profiles, as shown in Fig. 4.4, which are based on the 4 different samples of the EELS results in Fig. 4.4 and calibrated by the 40 u.c. LSMO film results. Since the 40 u.c. LSMO shows the same transport/magnetic properties as the LSMO bulk with an Sr doping of 0.33, the composition of the interior layers in the 40u.c. film can be used as the standard for all film calibration.

To get more a precise Sr/La ratio, we need to get rid of some extrinsic influences. First, the areas including the step, which always exist in the substrate and are shown in Fig. 3.1, need to be avoided. Figure 4.5 (a) is a schematic view of the STEM specimen including the terrace. The cutting and step direction is along b, and the STEM/EELS measurement direction is along a. For the STO substrates, the terrace width is about 70 nm. While, for the STEM specimen preparation, typi-

cal sample thickness is about 40 nm. The probability of the EELS/STEM including the step information is strongly dependent on the sample cutting direction. If the STEM specimen is cutting along the step direction, there is about a 57% chance for the specimen to include step information in the STEM and EELS results.

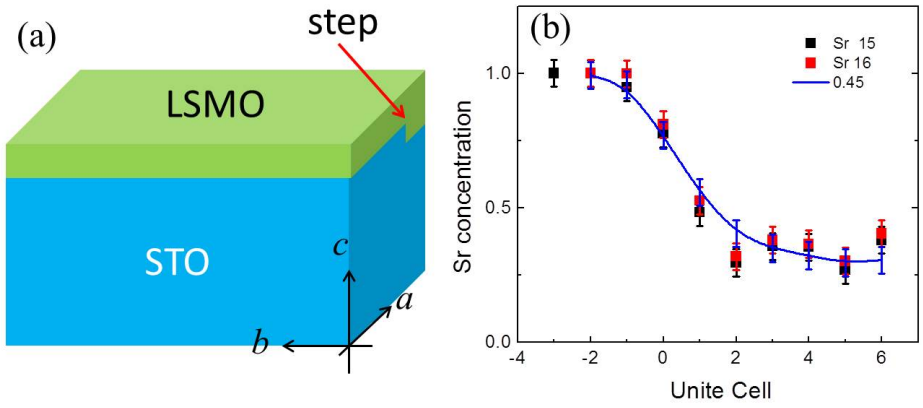

FIGURE 4.5: (Color online) (a) The STEM specimen includes a step. The cutting and step directions are along a; the STEM/EELS measurement direction is along b. (b) Based on sample (a) and (c) in Fig. 4.4 results and simple model of step, fitting results for sample (b) and (d) in Fig 4.4 are given.

If the step-included specimen is measured by STEM/EELS, the interface concentrations will not be intrinsic. Figure 4.4 illustrates this, including four sets of data, where in the first (La/Sr)O layer at the interface, the Sr concentrations in samples (a) and (c) are about 0.6 while samples (b) and (d) have a 0.8 doping. Another possible explanation for the samples differences are that the 8 u.c. LSMO film is not uniform. Other samples grown under the same conditions, such as 40 u.c. and 4 u.c. films, do not have such problems, which indicates that nonuniformity is intrinsic from the sample. Using the (a) and (c) sample results to model the step, the fit results with steps and samples (b) and (d) are shown in Fig. 4.5 (b). The error bar is 0.05, which is based on the Sr concentration deviation from the averaged results in the region from 2 u.c. to 6 u.c. in the Fig. 4.4. Figure. 4.5

(b) demonstrates that the difference in interface concentrations between samples (a), (c) and (b), (d) can be explained by the sample having a step, as found in our results.

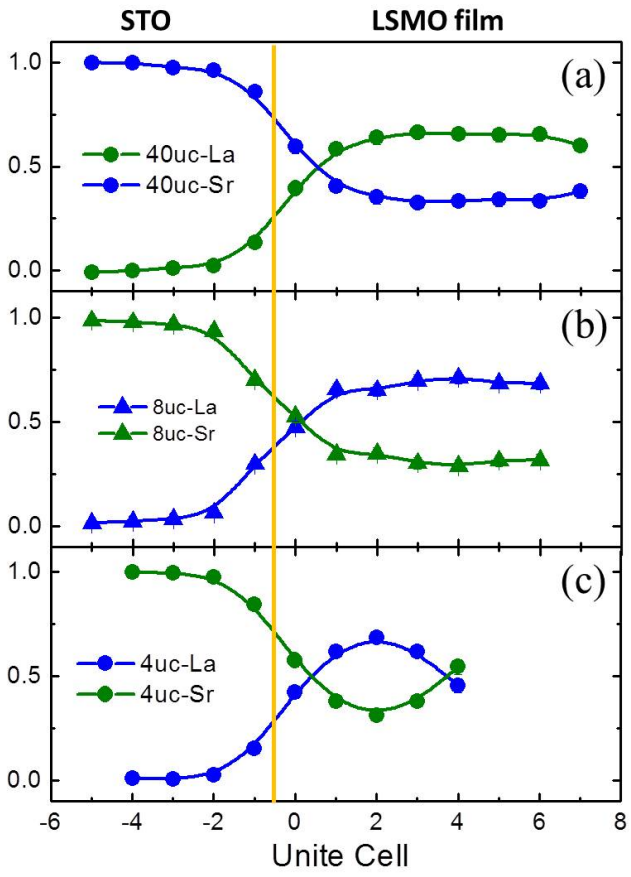

FIGURE 4.6: (Color online) Averaged EELS elemental concentration profiles for La/Sr as a function of distance (unit cells) from the interface between (a) 40 u.c., (b) 8 u.c., (c) 4 u.c. LSMO, and STO substrate.

After eliminating the step influence, three different EELS results for different films were averaged, as shown in Fig. 4.6, which give us more precise information. At the interface, the gradual change in Sr concentration can effectively reduce the diverging potential force from the polar discontinuity based on the electrostatic potential calculation [70]. For both thick and thin films, Sr concentrations reach ~ 0.60 with about 80% deviation from the interior composition, which should be

insulating as well as antiferromagnetic [142]. In the second (La/Sr)O layer (at 1 u.c.), for the thick 40 u.c. film, Sr dramatically drops to the bulk value of ~ 0.35 with about 6% deviation from its interior layers. While, for the thin films with 8 u.c. and 4 u.c., Sr concentrations still have a considerable deviation of 33% from the 0.33 value.

To produce a more quantitative difference at the interface of the thick and thin films, we fit the Sr profiles with the exponential function:

$$f_z^{Sr} = b + \delta_I \cdot exp(-zd/l_I) \tag{4.1}$$

where z indicates the position of the Sr/La-O layer (z=0 u.c. at the first interface layer), b is 0.33, and l_I is related to the decay length. The difference can be directly reflected in the fitting parameters. The Sr profiles can be fit well with this exponential function with a fitting parameter $l_I = 0.94 \pm 0.18$ for the 8 u.c. film. Although only three data points for 4u.c. can be used for fitting, which cannot give good fitting results, the ultrathin films of 4 u.c. and 8 u.c. have a very similar Sr depth profile at the interface, so that the 4 u.c. and 8 u.c. LSMO films should have similar decay lengths at the interface. For 40 u.c., the fitting parameter l_I is given by 0.26 ± 0.06. The Sr concentration decay in thin films (4 u.c. or 8 u.c.) is much slower than that of thick films (like 40 u.c.), which could be due to influences from its surface. The fitting parameters for Sr profiles near the interface are given in Table 4.1.

TABLE 4.1: Fitting results for Sr profiles near the interface of LSMO films

Film	δ_I	l_I/d	Sr
4 or 8 u.c.	0.31±0.02	0.95±0.18	0.33+0.31 · exp(-z/0.95)
40 u.c.	0.22±0.01	0.26±0.06	0.33+0.22 · exp(-z/0.26)

4.3 LSMO film surface composition from ARXPS

During the STEM sample preparation, a focused ion beam could damage the surface without any covering layers, which gives an unpredictable error bar not included in Fig. 4.6. In the Fig. 4.6, for the 8 u.c. LSMO film, two layers of Sr/La at positions 7 u.c. and 8 u.c. near the surface are not plotted because the EELS data for these two layers are not good, which is due to the aforementioned surface damage. This may cause the absolute value of surface Sr to be less reliable.

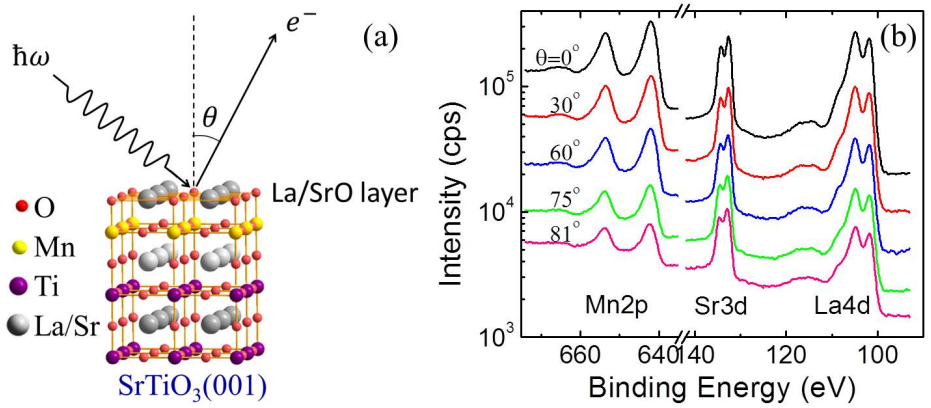

FIGURE 4.7: (a)Schematic diagram of ARXPS measurement. (b) raw ARXPS spectrum of Mn2p, Sr3d and La4d core levels for 65u.c. LSMO films grown on TiO_2 terminated STO substrate.

To obtain more precise surface information, the surface composition is determined by $in-situ$ ARXPS with the experimental schematic shown in Fig. 4.7(a). By changing the emission angle θ, angle-dependent XPS spectra are obtained. Figure 4.7(b) shows the raw XPS spectra containing Mn 2p, Sr 3d and La 4d core peaks for 65 u.c. LSMO films as a function of emission angle θ. Due to the finite inelastic mean free path of electrons, by vary emission angle θ, the XPS spectra provide chemical composition information from different depths.

To quantitatively analyze the chemical composition of an LSMO film near the surface, the angle dependence of the relative intensities of Sr3d/La4d is used. After subtracting the Shirley background from the raw data, the core level (Mn2p, Sr3d, and La4d) intensities for each emission angle can be calculated. Further, the angular dependence of the LSMO Sr3d/La4d intensities are obtained in Fig. 4.9 (a). For films with thickness $\leq$ 10 u.c., due to the Sr signal intensity partially coming from substrate STO, the fittings of ultra-thin films are disturbed and less reliable, and are not discussed here.

For the thick film fitting of Sr3d/La4d intensities, the equation for the XPS intensity ratio $R_{AB}(\theta)$ of two atoms core level peaks (A and B) must be used [99]:

$$R_{AB}(\theta) = \frac{I_A}{I_B} = \frac{\sigma_A * T_A}{\sigma_B * T_B} \frac{\sum_i f_i^A exp(\frac{-id}{\lambda_A cos(\theta)})}{\sum_j f_j^B exp(\frac{-jd}{\lambda_B cos(\theta)})} \tag{4.2}$$

Here, σ_A is the photoionization cross section of element A, T is the transmission coeffcient of the analyzer, d is the interlayer spacing, λ is the inelastic mean free path of the photoelectrons, θ is the emission angle with respect to the surface normal, and f_i^A is the atomic fraction of element A at the ith layer. For top surface layer, the i is 0. f_i^A is assumed to has an exponential segregation profile:

$$f_i^A = b + \delta_S \cdot e^{-id/l_S} \tag{4.3}$$

Where b is the bulk fraction of Sr (0.33) in our case; δ_S and l_S are two parameters determined by fitting.

Before using Eq. 4.2 and Eq. 4.3 to fit the angle dependence of the intensity ratios Sr3d/La4d, the relative parameters need to be calculated first. The parameters needed for the IMFP calculation are shown in Table 4.2. Combing Equation 2.10

and Table 4.2, the IMFP for different cores of LSMO are calculated and listed in Table 4.3, which includes all parameters for the relative intensity ratio calculation.

TABLE 4.2: Parameters to calculate the IMFP of characteristic curves for LSMO.

Valence electrons number N_v	27.33	Band gap E_g (eV)	0
Density ρ (g.cm^{-3})	6.27	Molecular weight M (g/mol)	224.75

TABLE 4.3: List of parameters for LSMO ARXPS Sr3d/La4d fitting.

Element	Shell	Cross section σ	Mean free path λ (Å)	Transmission coefficient T
Sr	3d	5.05	22.66	39.10
La	4d	6.25	23.06	38.89
Mn	2p	13.91	15.78	44.25
O	1s	2.92	19.01	43.30

By using this model, the Sr3d/La4d ratio of LSMO films (thickness $>$ 10 u.c.) can be fitted. Figure 4.8 (b) presents the fitting curve for the 65 u.c. LSMO film, which agrees very well with the experimental data.

Based on the complementary measurements with STEM/EELS and ARXPS, the layer-by-layer Sr concentrations near interface and surface of the LSMO film are obtained and compared. Figure 4.9 displays the Sr concentration profiles near the interface and surface for different thicknesses of LSMO films, which can be fitted well by using an exponential function for both the interface and surface regions, where z is the position of the (Sr/La)O layer with z = 0 at the interface layer, z =

n at the surface layer for an n u.c. film, such that i = n-z . The fitting results of the surface from ARXPS are displayed in Table 4.4. For these films, l_S, which is related to the decay length of Sr concentrations in the proximity of the free surface, is around 1. This is half the value of its interface. These results show that these thick films have the same surface with a slower decay ($l_S \sim 1$ u.c.) than their interface ($l_I \sim 0.26$ u.c.), which suggests different origins for surface and interface Sr richness.

TABLE 4.4: List of parameters of Sr 3d, La 4d, Mn 2p and O 1s core levels for LSMO ARXPS calculation.

Film	δ	l_S/d	Sr value
20 u.c.	0.25±0.01	0.83±0.16	0.33+0.25 · exp(-i/0.83)
40 u.c.	0.25±0.01	1.12±0.31	0.33+0.25 · exp(-i/1.12)
65 u.c.	0.24±0.01	1.07±0.16	0.33+0.24 · exp(-i/1.07)
Averaged	0.24±0.01	1.02±0.16	0.33+0.24 · exp(-i/1.02)

There is significant Sr segregation and layer-by-layer variation near the surface of LSMO films. The layer-by-layer Sr concentration near the surface of 20, 40, and 65 u.c. thick films are obtained through the fitting procedure described above and shown in the right part of Fig. 4.9. The Sr profiles are almost identical for these films, indicating that for all films above 20 u.c., this is the case. Sr concentration in the proximity of the surface shows a significant deviation from the nominal concentration (x = 1/3). For instance, Sr concentration in the top layer reaches $\sim$ 0.6 (increased by $\sim$ 80%) and the deviation from the bulk value extends to more than 3 u.c. from the top surface [see Fig. 4.9]. Based on periodic density functional theory calculations [141], significant Sr segregation is favorable for reducing the

total surface energy of these polar perovskite oxides films. This will be discussed further in the next chapter.

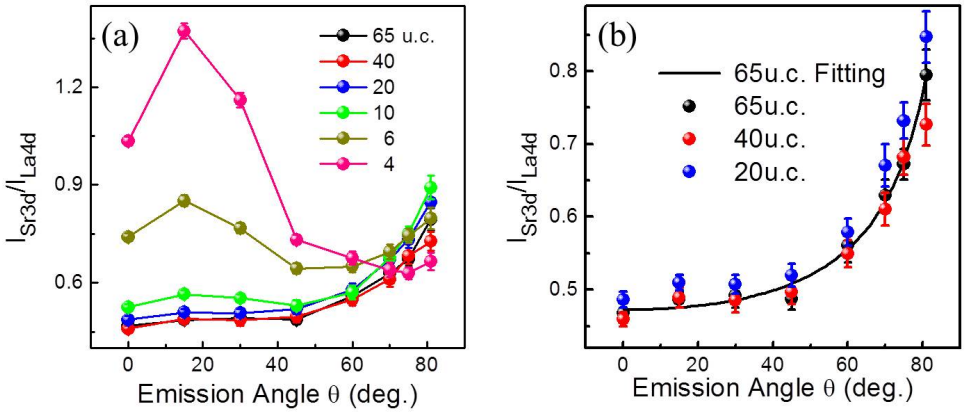

FIGURE 4.8: (a) Intensity ratio of Sr3d to La4d cores as a function of the emission angle θ for different thickness of LSMO films. (b) The experimental (20, 40 and 65 u.c.) and fitted (65 u.c.) intensity ratios of Sr3d/La4d as a function of emission angle for LSMO films.

However, the Sr concentration profile near the interface behaves differently. As shown in the left side of Fig. 4.9, the Sr profiles for the ultrathin films (4 u.c. and 8 u.c.) are different from that of the 40 u.c. film. The value $l_I = 0.26$ u.c. is related to the decay length for the 40 u.c. film and is only about 1/4 of that for ultrathin films ($l_I = 0.96$ u.c.) which is compatible with the $l_S = 1$ u.c. near the free surface. Because Sr compositions at the interface suffer from influence from its surface for ultrathin films, Fig. 4.9 shows the Sr doping variation at the interface that reflects the pure intrinsic interfacial effects only for thick samples such as the 40 u.c. film. The measured interface Sr profiles for ultrathin films should combine both intrinsic interface and surface contributions. Therefore, compared with these results near the surface, we can conclude that the deviation of the Sr concentration at the interface is small (only 1 u.c.), while in the proximity of the surface it is much larger (3 u.c.)[see Fig. 4.9]. The inter-diffusion may be the main reason for Sr

deviation at the interface, which is different from Sr segregation at the free surface of films.

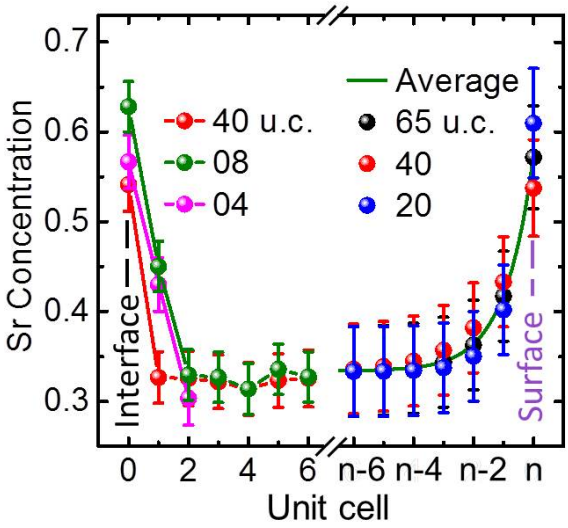

FIGURE 4.9: Layer-by-layer dependence of Sr concentration of LSMO films near (left) the interface determined by STEM/EELS and (right) the surface determined by ARXPS.

The observed large deviation of the Sr concentration near the surface and interface should have significant impact on the electronic and magnetic properties of ultrathin LSMO films, including the relevant dead-layer behavior. Because the various structural, electric, and magnetic phases of LSMO strongly depend on the Sr doping level due to strong lattice, charge, spin, and orbit coupling, numerous possible electronic and magnetic ground states compete with each other [134, 135]. Although strain and orbital order at the interface or phase separation were suggested as explanations for the dead layer phenomenon (antiferromagnetic insulating) in ultrathin films [121, 125, 19], Sr accumulation at the interface and surface indicates that the stoichiometry change occurring plays a key role in causing the dead layer. The layer-by-layer deviation in the stoichiometry also indicates that

a non-metallic surface always exists in thick films even though the ferromagnetic metallicity is dominant in overall film properties.

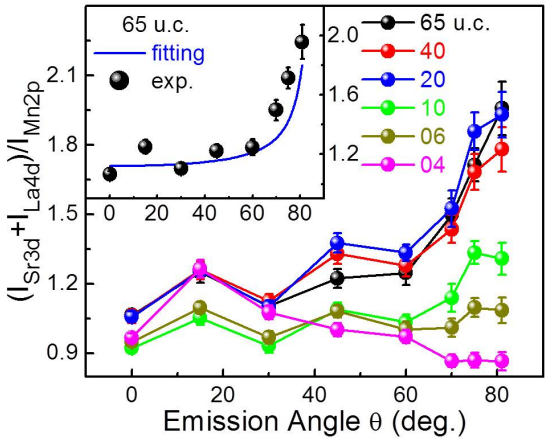

FIGURE 4.10: Intensity ratio of Sr3d plus La4d to Mn2p cores as a function of the emission angle θ for different thicknesses of LSMO films.

ARXPS provides information not only on the layer-by-layer Sr doping profile, but also surface termination. Figure 4.10 is the angle dependence of the intensity ratio of the (La 4d + Sr 3d) cores and the Mn 2p core for LSMO films with different thickness. The enhanced intensity around 18 deg. and 45 deg. is due to the elastic forward scattering effect, which is used to analyze the crystal structure through x-ray photoelectron diffraction [99]. For thick films ($\geq$20 u.c.), the θ dependence of (La 4d + Sr 3d)/Mn 2p intensity ratio curves collapse into almost a single curve, where the increasing magnitude with θ indicates that their terminations are dominated by the (La/Sr)O layer. For thin films (n<20 u.c.), (La 4d + Sr 3d)/Mn 2p is more complicated, due to the substrate contribution at small θ. However, estimated from the limited electron mean free path, the top 2 u.c. provide about 98% of the contribution to the value of (La 4d + Sr 3d)/Mn 2p at θ = 81°. Therefore, the intensity ratio at large emission angle θ should be reasonable

to determine the surface termination. We realize that the Sr surface segregation also affects the value of (La 4d + Sr 3d)/Mn 2p. However, we estimate that the maximum contribution for the drop of (La 4d + Sr 3d)/Mn 2p with decreasing thickness is only $\sim 13\%$, much smaller than the observed $\sim 50\%$ [see Fig. 4.10 at $\theta = 81°$], thus indicating the change of termination layer with reduced film thickness.

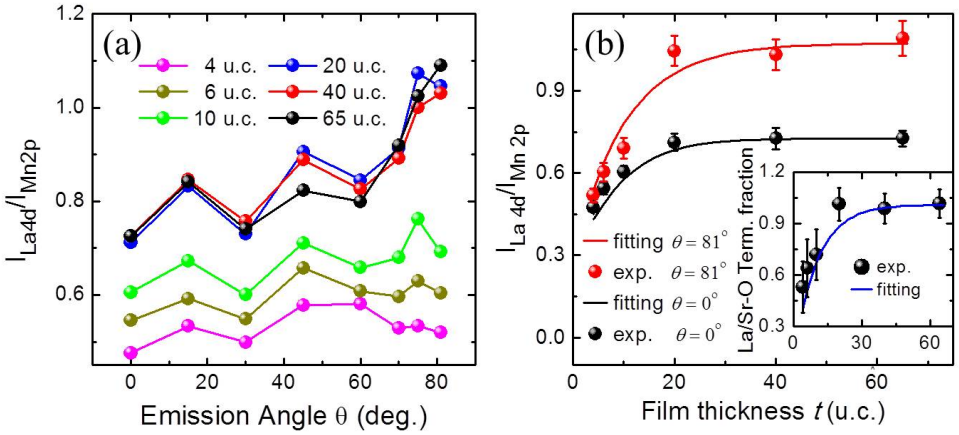

FIGURE 4.11: (a) Intensity ratio of La4d to Mn2p cores as a function of the emission angle θ for different thickness of LSMO films. (b) Intensity ratio of La4d to Mn2p core as a function of film thickness for $\theta = 0°$ and 81°. The inset presents the determined fraction of surface La/Sr-O termination for different thickness of LSMO films.

To further quantitatively understand the thickness dependence on the surface termination without influence from the STO substrate, we chose the La 4d/Mn 2p intensity ratio instead of (La 4d+Sr 3d)/Mn 2p to perform the quantitative analysis, which is shown in Fig. 4.11 (a). Figure 4.11 (b) is the film thickness dependence of the La 4d/Mn 2p intensity ratio at 0 and 81°. Based on the Sr concentration obtained from the above EELS and ARXPS results, the La 4d/Mn 2p intensity ratio vs. film thickness data can be fit using the classical XPS model [see Eq. 4.2 and 4.3] with a mixed termination ratio between (La/Sr)O and MnO_2 layers, as shown in Fig. 4.11 (b). The (La/Sr)O termination percentage as a function of

film thickness is also obtained and shown in the inset of Fig. 4.11 (b). From the calculated and fitting results, one can easily find that the thinnest film (4 u.c.) in our experiment has a mixed termination dominated by MnO_2, and the fraction of (La/Sr)O termination increases with the film thickness. Although MnO_2 termination is expected from the preservation of perovskite stacking due to the epitaxial growth on STO with TiO_2 termination, LSMO films eventually evolve to pure (La/Sr)O termination at thicknesses above $\sim$ 20 u.c., consistent with the surface energy DFT results claiming that $La_{1-x}Sr_xO$ termination has less energy cost and higher stability [141]. In addition, different surface terminations of LSMO films also provide different electrostatic potential at the interface of the associated heterostructures, and will induce further influence on the interfacial structures, such as octahedral tilt angle, cation displacement and so on. These differences and changes also have significant impact on the electric, magnetic, and ferroelectric properties of those artificial heterostructures [143, 144].

4.4 Summary

In this chapter, we report our studies on the thickness dependence of the chemical composition variation with atomic layer precision for $La_{2/3}Sr_{1/3}MnO_3$ (LSMO) thin films grown on STO (001) substrate with TiO_2 termination. The measurements were performed utilizing a combination of $in-situ$ and $ex-situ$ microscopy and spectroscopy tools. Our results reveal that there is a substantial increase in the Sr concentration from its bulk value $x = 0.33$ both at interface and in the proximity of the film surface, though they have distinct origins. The deviation at the interface with the STO (001) substrate is mainly due to single unit cell intermixing, but the deviation in proximity to the film surface is because of surface Sr segregation. Although STO (001) with TiO_2 termination was used as a substrate, LSMO film surfaces experience a gradually self-organized conversion from MnO_2

to (La/Sr)O layer termination with increasing film thickness. Such layer-by-layer variation in chemical composition and its dependence on film thickness will have a significant impact on the physical properties of these epitaxial films and relevant heterostructures.

Chapter 5
Surface investigation

5.1 Introduction and motivation

Perovskite manganites have been extensively studied for more than half a century due to their rich physics such as colossal magnetoresisitance, charge ordering, half-metallicity, and phase separation, which are related to the close coupling among the charge, lattice, orbital, and spin [134]. The rich phase diagram of one such perovskite, $La_{1-x}Sr_xMnO_3$, is shown in Fig. 1.5. LSMO is of particular interest due to its high Curie temperature T_C ($\sim$ 369 K in the bulk crystals), its distinction as the most electrically itinerant material among the manganites [135], and the possible technological application. For LSMO ultrathin films, the metallicity as well as ferromagnetic ordering are greatly suppressed [27, 136] and is usually referred to as having a dead layer, so that the film exhibits a metal-insulator transition (MIT) with reducing film thickness. Understanding the nature of the MIT still remains highly controversial even though understanding and controlling such behavior is essential for the future of interface physics.

In the previous chapter, the chemical composition variation with atomic layer precision for LSMO films was given, and the data therein suggests that Sr variations on the surface and interface have an immense impact on the physical properties of the epitaxial films and heterostructures. Although similar conclusions about the immense impact on the LSMO application and properties have been suggested by many groups [66, 69, 140, 141, 145], there is no study about the influence on surface properties coming from the significant composition deviations.

5.2 Surface morphology and local tunneling conductivity(STS/STM)

Scanning tunnelling microscopy (STM) and spectroscopy (STS) provide us with powerful *in-situ* tools to characterize the local surface morphology and electronic states of materials on the nanoscale, and help us obtain the intrinsic surface information, such as morphology and electrical properties, of surface states of LSMO thin films with Sr-rich surfaces that were observed by STEM and ARXPS in chapter 4.

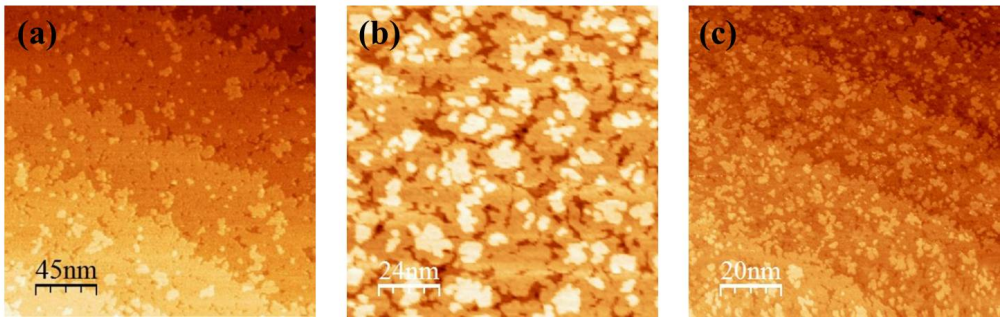

FIGURE 5.1: The STM morphological surface images of (a) 12 u.c., (b) 40 u.c. and (c) 60 u.c. LSMO films on STO with TiO_2 termination. The STM images are obtained at bias voltage V = 1.0 V, tunneling current setpoint I_p = 20 pA, and at room temperature).

Achieving an atomically-flat surface for these thin films is essential in order to understand the physics of these oxides surfaces with broken symmetry as well as produce any oxides-based device applications or other heterostructure fabrications. After the systematic studies given in chapter 3 on the optimization of growth parameters and conditions for LSMO films such as substrate preparation, growth temperature, Ar/O_2 and O_3 gas pressure, laser power and frequency etc., we obtained layer-by-layer growth of thin epitaxial LSMO films on STO with TiO_2 termination, which has better transport and magnetic properties as well as an atomically flat surface. As a reminder, in chapter 3, the 12 u.c and 20 u.c. LSMO films on STO(001) had an atomically flat surface, metallic behavior, and high elec-

trical conductivity, which was proven through LEED, RHEED, and STM images and the temperature dependence of the resistivity shown in Fig. 3.5, Fig. 3.6, and Fig. 3.8 respectively.

To further prove that the surface is atomically flat, LSMO films with different thicknesses were investigated systematically with *in-situ* STM morphological surface images, as shown in Fig. 5.1. The scans were recorded with a bias voltage of 1 V and a tunneling current setpoint of 20 pA at room temperature, the size of images being 250 $\times$ 250 nm^2 for 12 u.c., 120 $\times$ 120 nm^2 for 40 u.c. and 100 $\times$ 100 nm^2 for 60 u.c., respectively. In Fig. 5.1, one can easily see that the films have atomically flat surfaces with a clear step ($\sim$ 0.4 nm) induced by the STO substrate. The terrace width depends on the cut angle of the substrate and substrate treatment processes. Even for the same batch of substrates, the terrace width can vary from 20 nm to 50 nm. For all the films, the flatness of each step is within 1 u.c. ($\sim$ 0.4 nm) and are devoid of any land-type flat grains.

The atomically resolved layer-by-layer stoichiometry was obtained with ARX-PS and STEM and discussed in chapter 4, revealing that there is a considerable deviation in the Sr concentration ($x \sim 0.57$) from its bulk (x =1/3) value both at the interface and close to the film surface. Based on the complex electric phase diagram of LSMO introduced in chapter 1, the slight variation in Sr doping is expected to have a significant impact on its physical properties. Therefore, the Sr-rich deviation of 40%$\sim$ 80% in the proximity of the film surface (within 1-2 u.c.) should cause distinctly different physical properties at the surface compared to layers inside the film. To precisely extract the intrinsic electronic state of the surface from the adjacent metallic inside layers, scanning tunneling spectroscopy (STS) was performed systematically on LSMO films with different thicknesses at different temperatures. Our STS measurements were taken by Pt-Ir tips cleaned

with focused ion beams. In addition, tungsten tips were also used for comparative experiments to asses any tip influence on the experiment's results, which will be discussed later. Before taking each STS data set, the stabilization of the system was checked by setting a bias voltage to $V = 0.5$ V and tunneling current setpoint to $I_p = 50$ pA. The STM feedback was then turned off to fix the distance between tip and sample, after which the tunneling current I versus the bias voltage V between sample and tip were measured and recorded as $I - V$ spectra. For each sample, we randomly chose $10 \sim 15$ locations for performing $I - V$ spectra, and for each location, twenty $I - V$ curves were recorded, half scanning from +0.5 V to -0.5 V, and half scanning -0.5 V to +0.5 V.

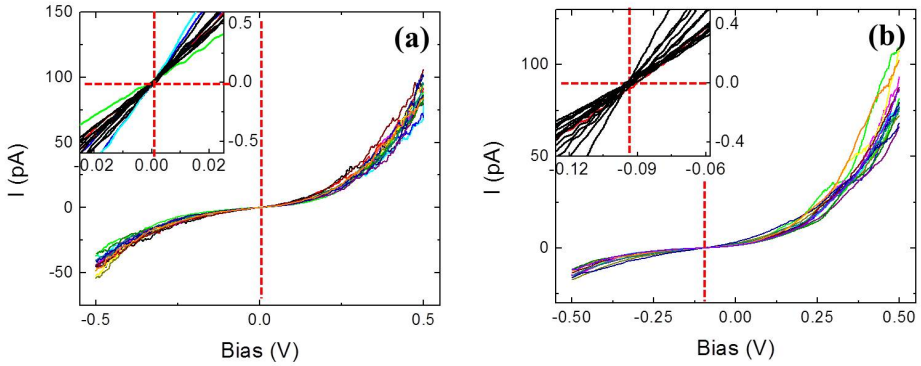

FIGURE 5.2: The 200 $I-V$ curves of 40 u.c. LSMO film are measured at 10 different locations at (a) room temperature (RT) and (b) low temperature ($\sim$ 100K, LT) ($V_b = 0.5$ V, $I_{setpoint} = 50$ pA).

Figure 5.2 shows the $I - V$ spectra of the 40 u.c. LSMO film obtained at room temperature (RT) and low temperature (LT)$\sim 100K$ at different locations. The insets display zoom-in's of the spectra near the zero current region. In Fig. 5.2 (a), the RT $I - V$ spectra starting with both positive (+0.5 V) and negative(-0.5 V) voltage biases have similar gapless shapes, which suggests that the 40 u.c. LSMO film is metallic at RT. In addition, the zoom-in spectra in the inset of Fig. 5.2 (a)

clearly shows that the voltage bias $V_b = 0$ V corresponds to a tunneling current of $I_t = 0$ pA. Figure 5.2 (b) is the $I - V$ spectra for the 40 u.c. LSMO film measured at LT ($\sim$ 100 K). Similar to the RT $I - V$ spectra, there is no gap observed in the LT $I - V$ spectra. However, the zoom-in spectra in the inset of Fig.5.2 (b) clearly shows that, when the tunneling current is $I_t = 0$, the applied voltage bias V_b is 95 mV rather than 0. This shift of voltage bias at zero tunneling current is completely different from the STS $I - V$ spectra for a normal metal. This shift of voltage bias at zero tunneling current is called a 'zero current bias shift' or 'bias shift'.

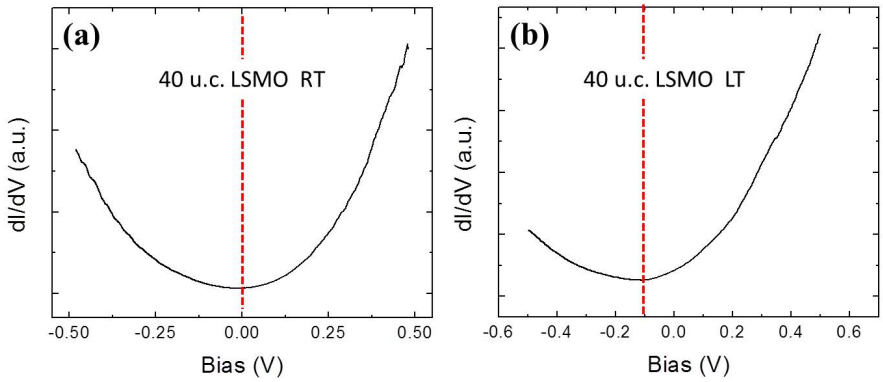

FIGURE 5.3: The differential tunneling conductance dI/dV spectra of 40 u.c. LSMO film measured at (a) room temperature (RT) and (b) low temperature ($\sim$ 100K, LT) ($V_b = 0.5$ V, $I_{setpoint} = 50$ pA).

In our particular case, the bias shift also can be defined by the minimum of the dI/dV spectra. In our experiments, the tunneling conductance $dI/dV - V$ spectra are directly measured by a lock-in amplifier. For samples with the same thickness, the $dI/dV - V$ curves measured at different locations at certain temperatures are very similar. Each $dI/dV - V$ spectrum reported here has an average of about 200 $dI/dV - V$ curves measured at 10 different locations. Figure 5.3 is the averaged $dI/dV - V$ spectra of the 40 u.c. LSMO film at RT (a) and LT$\sim 100K$ (b). The minimum of dI/dV is marked with the red dash line. In Fig. 5.3, the minimum of

the tunneling conductance spectrum at RT is around $V_b = 0$ V, while the minimum at LT $\sim$ 100 K is at a bias shift of - 0.1 $\pm$ 0.01 V, which is consistent with the results obtained in the $I - V$ spectra in Fig. 5.2.

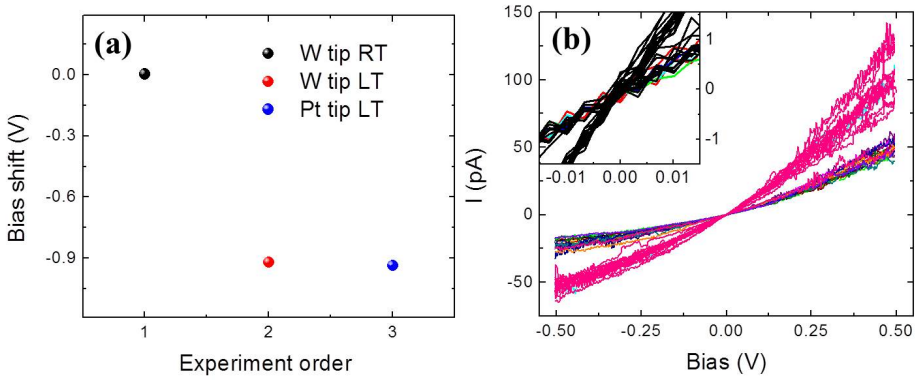

FIGURE 5.4: (a) Bias shift of 40 u.c. LSMO film extracted from the STS spectra measured by using Pt-Ir tip and W tip at RT and low temperature (LT$\sim$ 100k). (b) The STS spectra of 10 u.c. $SrVO_3$ film measured at low temperature ($\sim$ 100k) ($V_b = 0.5$ V, $I_{setpoint} = 50$ pA (blue) and 100 pA(red))

Before we further discuss the underlying physics of the bias shift phenomenon, any possible extrinsic disturbances needs to be ruled out, such as from tips or other STM/STS instruments, or other uncertain factors. First, to figure out whether the bias shift comes from the tips of the STM, we repeated the LT STS experiments many times using different Pt-Ir tips, and these experiments always gave the same bias shift value for the 40 u.c. LSMO films. Those results are not shown here. Furthermore, we also used tungsten tips to explore different materials to repeat the LT STS measurements on 40 u.c. LSMO films, the results of which are shown in Fig. 5.4 (a). The results obtained by both the W tip and Pt-Ir tip show a similar bias shift value of - 0.1 $\pm$ 0.01 V. Secondly, to further exclude possible instrument interference, a standard sample of highly oriented pyrolytic graphite (HOPG) was measured at LT, and the spectra of HOPG found were consistent with the results

reported by other groups. There was no bias shift observed for HOPG in the LT STS spectra. We also grew a 10 u.c. $SrVO_3$ (SVO) film on the TiO_2 terminated STO substrate, and it was observed that the SVO film has good conductivity and shows a metallic behavior, much the same as LSMO. However, different from the LSMO films, there was no element segregation or accumulation at the surface of SVO because Sr is the only element at the A-site of these perovskites. For the SVO film, $I - V$ spectra were also measured at RT and LT$\sim$ 100 K. The STS spectra of our SVO film shows normal metallic STS spectra without any bias shift, seen in Fig. 5.4(b). The above RT and LT STS experiments of HOPG and SVO films were performed using the same STM/STS instrument as was used to investigate the LSMO films. Therefore, we can safely conclude that the bias shift observed on LT LSMO films is not due to extrinsic instrumentation issues.

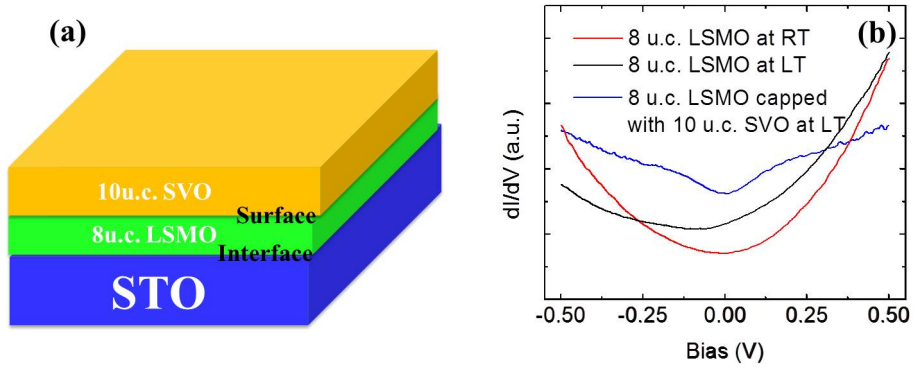

FIGURE 5.5: (a) Schematic view of 8 u.c. LSMO film grown on STO substrate capped with 10 u.c. SVO films. (b) The $dI/dV - V$ spectra of 8 u.c. LSMO film and 8 u.c. LSMO film capped with 10 u.c. SVO obtained at RT and LT $\sim$ 100 K, respectively.

To further investigate the origin of the bias shift, the experiment is designed to determine if the bias shift originates from the LSMO film surface or the interface between LSMO films and the STO substrate. Only 8 u.c. LSMO thin films were

studied with the STS, and the dI/dV spectra at RT and LT are shown in Fig. 5.5 (b), which only shows a bias shift of V_{shift} = - 0.08 ± 0.01 V at LT, which is comparable to the V_{shift} = - 0.1 ± 0.01 V from 40 u.c. LSMO films. In the SVO experiment above, the STS spectra shows that SVO has the same conductivity as LSMO and no bias shift at RT or LT [see Fig. 5.4 (b)]. To probe their relationship, another 10 u.c. SVO film was grown on top of the 8 u.c. LSMO film, as illustrated in Fig. 5.5 (a). The electronic properties of this LSMO/SVO bilayer film were studied using STS. As with previous research done by my group where LSMO thin films were capped with STO, the 8 u.c. LSMO film with 10 u.c. SVO capping should show a better conductivity and ferromagnetism with higher T_c than the 8 u.c. LSMO without capping. The original surface of the LSMO film is destroyed however, changing into an interface between LSMO and SVO. The $dI/dV - V$ spectra of the LSMO film with 10 u.c. SVO capping shows a metallic characterization much the same as the metallic SVO film, and no bias shift is observed at LT. The bias shift in the STS spectra should be observed at LT if the shift comes from the interface between the LSMO film and STO substrate, because SVO capping only suppresses the surface of LSMO and has no impact on that interface. This experiment further confirms that the bias shift behavior is most likely due to the non-conductive LSMO surface state. These bias shift phenomena are typically observed in insulating ferroelectric materials due to spontaneous electric polarization [146, 147], the insulating surface of polar compounds due to electrostatic coupling induced polar surfaces [130], or p-n junctions under illumination due to the photovoltaic effect [148, 149, 150]. In general, these bias shift phenomena are the result of the electric field based on the non-conductive grain boundary or surface due to the external excitation-induced charge accumulation or spontaneous electric polarization.

To further confirm the existence of an electric field (or charge accumulation) at the surface of LSMO at low temperature, the LT XPS is performed on a 40 u.c. LSMO film. Figure 5.6 (a) shows the O 1s spectra of the 40 u.c. LSMO film measured at RT and LT $\sim$ 100 K with emission angle $\theta = 0°$. For $\theta = 0°$, XPS mainly carries more information from the inside of the LSMO films. The asymmetric peak shape of O 1s, which comes from the low energy electron hole excitation, indicates the internal metallicity of the LSMO film.

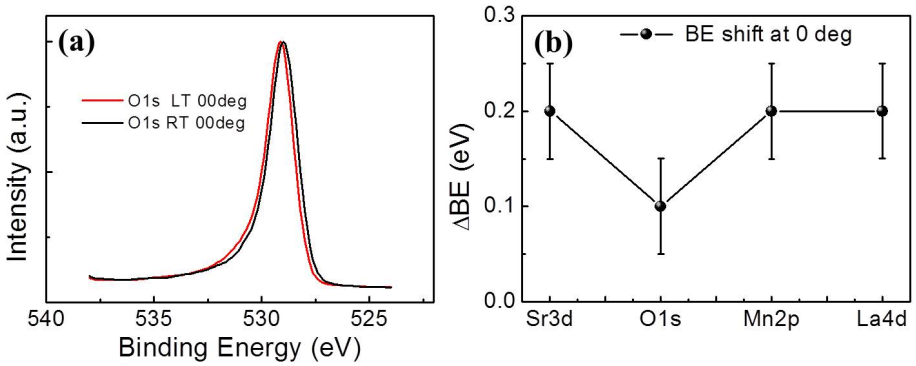

FIGURE 5.6: (a) XPS O 1s core-level spectra of 40 u.c. LSMO film on STO substrate measured at RT and LT $\sim$ 100 K. (b) The binding energy difference for RT and LT La 4d, Sr 3d, Mn 2p and O 1s core-level spectra of 40 u.c. LSMO film.

Compared with the O 1s core at RT, O 1s at LT shifts to a higher binding energy by about 0.1 eV. Similarly, the binding energy differences between RT and LT for the Sr 3d, Mn 2p, and La 4d spectra individually are also compared, as shown in Fig. 5.6(b). The XPS spectra are measured in 0.1 eV steps, so the 0.1 eV error bar is a given in our XPS data. In chapter 4, ARXPS and STEM demonstrate the chemical composition variation with atomic layer precision for the LSMO films and show that the top $\sim$ 2 u.c. layers of the LSMO films have much larger Sr doping (0.45-0.56) than the inside layers(x = 1/3). Based on the phase diagram of LSMO, the composition analysis also suggests that the top 2 u.c.

layer should show much less conductivity and might even become insulating. STS also demonstrates that the surface is nonmetallic at LT. The 40 u.c. LSMO film is very metallic, having excellent conductivity in the bulk. However, for the XPS spectra, the binding energy of all elements (La, Sr, Mn, and O) obtained at LT are higher than at RT, which is consistent with the STS results, and should be due to surface charge accumulation and a surface induced electric field. We can then safely conclude that the bias shift in the STS spectra and XPS spectra shift to higher binding energy at low temperature, which directly demonstrates that the surfaces of both thin and thick LSMO films are nonmetallic, which is distinct from the inside metallic layers in thick LSMO films.

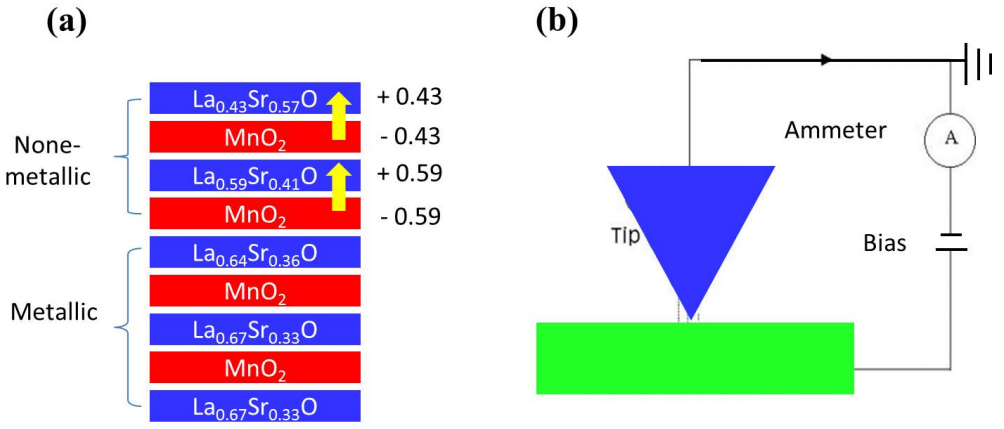

FIGURE 5.7: (a) Schematic view of the polar surface of thick LSMO film based on the ARXPS results. The yellow arrow is the spontaneous polarization P_S. (b) Schematic diagram of the STS experiment. I is the tunnel current, and V is the bias applied between the tip and sample.

Furthermore, the bias shift in our low temperature STS experiments also indicate that a spontaneous electric field exists in the non-conductive Sr-rich surface. The physical effects that induce this spontaneous electric field in the epitaxial growth of polar LSMO thin films with non-conductive surfaces are still in question. It is well known that the emergence of a two-dimensional electron gas in LAO/STO

comes from the so-called polar discontinuity, which was introduced in chapter 1 in detail. The presence of this polar discontinuity at the interface leads high density bound charges at the interface. These bound charges incite a linear divergence of the electrostatic potential with increasing polar compound (LAO) thickness, a phenomenon referred to as polar catastrophe. To avoid the potential divergence and reduce the energy cost, the junction or surface undergoes charge redistribution to screen these bound charges by the displacement of ions or electronic reconstruction, thus creating a spontaneous electric polarization. The emergence of spontaneous polarization has been theoretically predicted and experimentally observed in polar and non-polar oxide heterojunctions. In the discussion of layer-by-layer composition in chapter 4, our ARXPS date not only calculates the concentration variation at the surface of LSMO films, but also provides termination information for the thick films. According to our ARXPS results, the schematic of the elemental stacking and bound charge stacking in the non-conductive 2 u.c. top surface layers of LSMO films are drawn in Fig. 5.7 (a). Although the total charge in each top layer has some variation due to the Sr concentration change, these bound positive and negative charge stacking induced spontaneous electric polarizations do not change their directions because the same elemental stacking order and (La,Sr)O terminations of LSMO thick films grown on STO with TiO_2 termination are seen. Since the electrostatic screening effect is from metallic layers below the top insulating surface layers, the spontaneous electric polarization P_S comes only from the contribution of the several top surface layers of LSMO films (2-3 u.c.). Based on the direction of P_S marked with the yellow arrow in Fig. 5.7 (a), a positive electric field E is generated in the top surface of LSMO films. To illustrate the influence of a positive spontaneous electric polarization P_S in the STS spectra, a schematic of the STS experiment is given in Fig. 5.7 (b). In an STS experiment with sample bias

V and a grounded tip, by changing the external bias voltage V_E, the corresponding tunneling current I_t is measured. As shown in Fig. 5.7(b), when the positive bias is applied to the sample, the positive tunneling current I_t is measurable and in the clockwise direction. If the LSMO film has a positive spontaneous potential V_S built into the surface, the total bias voltage V_t between the tip and the sample is given by $V_E + V_S$. If $V_E = 0$, the positive tunneling current I_t can still be excited by a spontaneous V_S. If zero current is desired, then V_t must equal 0 (V_E = - V_S), which causes a negative bias shift in the STS spectra. Currently, this argument is based on the ARXPS results without any structural distortion, and its influence will be discussed later.

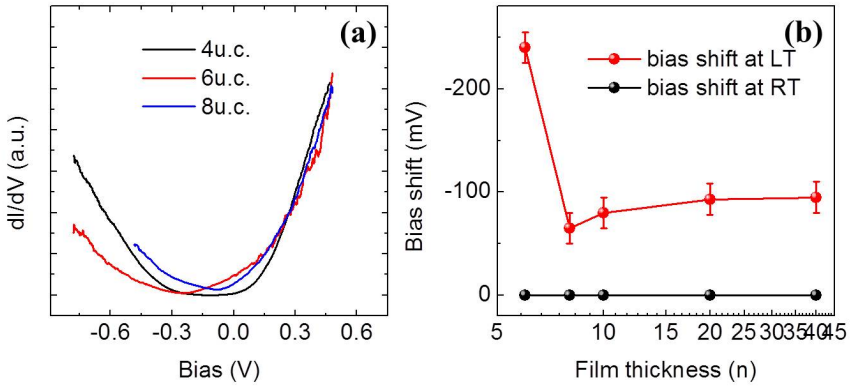

FIGURE 5.8: (a) Averaged and tunnel spectra of the 4, 6, and 8 u.c. LSMO films at LT $\sim$ 100 K. (b) The thickness dependence of bias shift obtained at RT and LT $\sim$ 100 K.

We further investigate the thickness dependence of the bias shift. The films with thicknesses ranging from 4 u.c. to 40 u.c. are all grown on STO with $TiO2$ termination under the same growth conditions. Figure 5.8 (a) is the dI/dV spectra of 4, 6, and 8 u.c. LSMO films measured at LT $\sim$ 100 K. One can easily observe that the 4 u.c LSMO film has a clear gap in its tunneling conductance spectra, consistent with the insulating behavior of the 4 u.c. LSMO film observed with standard

electrical transport measurements. If we assume the exiting gap is symmetric about the fermi level, the bias shift of 4 u.c. LSMO is around 0.15 V. Although the temperature dependence of the resistance of the 6 u.c. film displays insulating behavior, it does not show a clear gap in the LT STS spectra, which suggests that the metallic layer still exists at LT. Since the films grow layer-by-layer on STO substrates in many steps of 20-100 nm width and 0.4 nm height (see Fig.5.1), the insulating behavior observed in the macroscale resistance measured using the standard four-probe method is the result of these step induced-grain boundaries and the insulation of the conductive layers in such thin films (only 2.4 nm) from each other. However, the STS spectra, which only reflect local information, show a nanoscale electronic state for the films. For 8 u.c. LSMO films, the dI/dV spectrum is similar to that of 40 u.c. thick films. To investigate the evolution of the bias shift with the thickness of films, the dependence of bias shifts on thickness n in u.c. are given in Fig. 5.8 (b). At RT, $I-V$ spectra for all films do not show any bias shift. While at a LT of about 100 K, the bias shift value is around 90 mV for all films except the 4 and 6 u.c. films. This indicates that the films above 8 u.c. have the same surface states which are non-conductive with SrO termination and Sr-rich due to the Sr segregation at the surface, which is consistent with the elemental composition analysis results obtained from our ARXPS and STEM. For ultrathin 4 and 6 u.c. films, the bias shift is almost double the value of the thick films due to these ultrathin films showing insulating behavior not having electrostatic screening influences.

The temperature evolution of the bias shift for 40 u.c. LSMO film was also investigated with the temperature range from 100 K to 300 K. Based on the $I-V$ and dI/dV spectra, the bias shift as a function of temperature is obtained and shown in Fig. 5.9, where the black spots represent the bias shift without light

illumination. At RT, no bias shift is observed. When sample cooling to 150 K, there is very tiny bias shift observed. When the sample is further cooled down to $\sim$ 100 K, the bias shift increases to about 100 mV.

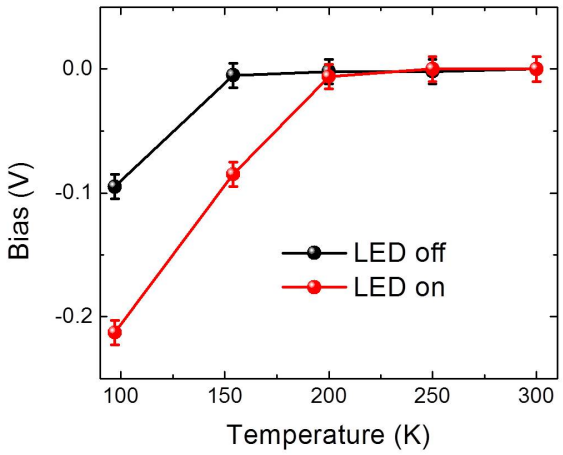

FIGURE 5.9: Temperature dependence of bias shift for 40 u.c. LSMO film measured with LED light on and off.

In addition, photovoltaic-like effect of the $I-V$ and dI/dV spectra for 40 u.c. LSMO film was studied with the temperature range from 100 K to 300 K. In Fig. 5.9, the red spots illustrate the bias shift including photovoltaic effects under LED light illumination. LED light is broad, with wavelengths ranging from 380 to 780 nm, i.e. with energies ranging from 3.2 eV to 1.6 eV. At RT, bias shift is zero with light illumination, which is similar to the result without light illumination. However, when the sample is cooled down below 200 K, the bias shift first begins to appear under LED light illumination. When the sample is further cooled down to $\sim$ 100 K, the bias shift for the illuminated sample increases to about 220 mV, which is doubled by the the LED light illumination. The bias shift was enhanced by LED light illumination, which uses the same photoelectric effect as the aforementioned XPS experiment, the only difference being that XPS uses high

energy X-ray and LED uses low energy visible light to excite electrons out of the LSMO film. There are many experiments in perovskite ferroelectric oxides that have observed photovoltaic efficiencies comparable to semiconductor p-n junction solar cells [148, 149, 150]. Recently, intensive studies are focusing on how to use the spontaneous polarization of ferroelectric oxides to enhance power conversion efficiency in photovoltaic systems [149]. Our LED light enhancement of the bias shift in the STS spectra suggests that high efficiency may be achieved in single ferromagnetic perovskite oxides with a metallic bulk and spontaneous polarization surface or interface due to elemental surface segregation and interface engineering.

5.3 Layer-by-layer structure

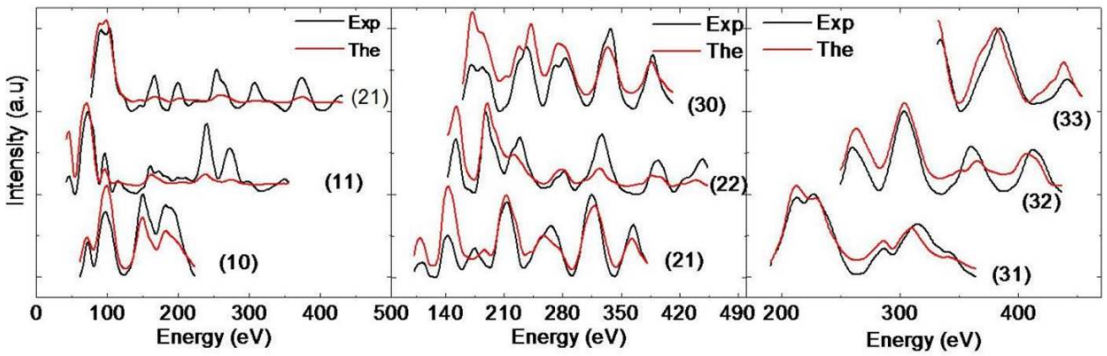

FIGURE 5.10: Comparison between experimental and theoretically-generated I(V) curves for the final structure of 2 u.c. LSMO film surface at RT

To quantitatively calculate and understand the origin of the bias shift, we further used LEED-IV refinement to determine the surface structure and chemical composition. Nb-doped STO substrates were used for LEED experiments. The growth conditions for the LSMO films for LEED I-V were similar to LSMO films used in STM and XPS experiments. After films were grown in the growth chamber, they were $in-situ$ transferred into the main chamber for LEED analysis. The LEED-IV was taken at room temperature at an ultra high vacuum pressure of 4

$\times 10^{-10}$ Torr. The surface structure is p(1×1), which has already been illustrated in chapter 2.

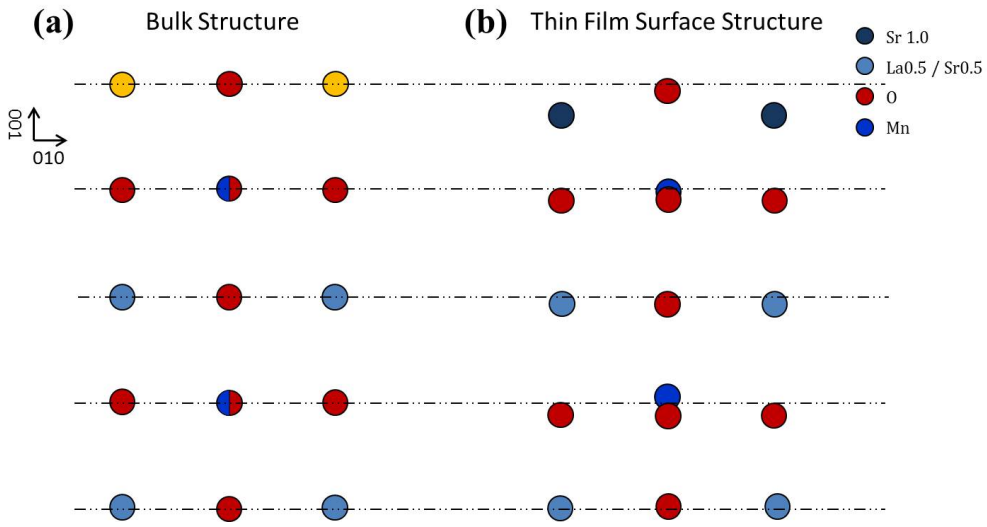

FIGURE 5.11: (a) bulk structure of LSMO and (b) Surface Structure of 2 u.c. LSMO film

To determine details of the structure and their evolutions with thickness, LEED-IV structural refinements were performed. Final LEED-IV refinement of a 2 u.c. LSMO sample is shown in Fig. 5.10, which gives an extremely low R_p factor of 0.16. For the LEED-IV refinement, the R_p factor needs to be smaller than 0.3, where lower R_p means the surface structure refinement is more reliable. Based on the LEED IV refinement, the relative atomic postions of the surface are given in Table 5.1 and the structure model is shown in Fig. 5.11.The LEED-IV refinement shows that the topmost atomic layer is SrO. Because LEED is only sensitive to the top layer, our assertion of an SrO layer on the surface is reliable. In the LEED refinement, although the ratio of the Sr/La layer is given by La0.5Sr0.5, the insensitivity of LEED to any other levels underneath the second (La/Sr)O layer makes the exact La to Sr ratio at inner layers unclear. According to the refinement results, both Sr and O in the topmost layer move down. In particular, the Sr moves

down by 0.2952 Å, while O moves down 0.0685 Å. The atoms of MnO_2 in the 2nd layer are not in their original bulk positions. Mn moves down 0.0112 Å , while two O atoms move down about 0.0822. As a result, the out of plane lattice constant in the (001) direction of the topmost unit cell is compressed by 0.27 Å, and the bottom unit cell is compressed by 0.09 Å. The averaged lattice constant for a 2 u.c. LSMO sample is 3.7 Å.

TABLE 5.1: Relative atomic positions of the refined surface structure of 2 u.c. LSMO film grown on STO.

Layer	Atom	Bulk position (Å)	Surface position (Å)	△Z (Å)	Error (Å)
1	Sr	0.0000	0.2952	+0.2952	± 0.03
1	O	0.0000	0.0685	+0.0685	± 0.03
2	O	1.9467	2.0289	+0.0822	± 0.04
2	O	1.9467	2.0289	+0.0822	± 0.04
2	Mn	1.9467	1.9579	+0.0112	± 0.01
3	La/Sr	3.8933	3.9232	+0.0299	± 0.04
3	O	3.8933	3.9232	+0.0415	± 0.05
4	O	5.8400	5.9313	+0.0913	± 0.12
4	O	5.8400	5.9313	+0.0913	± 0.12
4	Mn	5.8400	5.8269	-0.0131	± 0.01
5	La/Sr	7.7867	7.7279	-0.0588	± 0.07
5	O	7.7867	7.7336	-0.0531	± 0.27

Similar to the 2 u.c. LSMO film, surface structure refinement of 6, 8, and 10 u.c. films can be achieved by LEED-IV refinement, as shown in Table 5.2. The R_p for 6 u.c. and 10 u.c. LSMO are 0.3125 and 0.3155 respectively, which are good enough

for complex oxide films. For the 6 u.c. LSMO film, the best model shows 70% of Sr at the topmost layer, while for a 10 u.c. film, the topmost layer is given by 60% of Sr in the fitting model. Another remarkable part of the structure is that, for the 6 u.c. LSMO, the topmost surface unit cell is compressed by 0.73 Å, which is bigger than that of the 2 u.c. (0.27 Å) and 10 u.c. (0.41 Å) films. The second unit cell is compressed by 0.05 Å, which is a little smaller than that of the 2 u.c. (0.09 Å) and 10 u.c. (0.09 Å) films.

TABLE 5.2: Relative atomic positions of the refined surface structure of 6 u.c. and 10 u.c. LSMO films.

Layer	Atom	Bulk position (Å)	Surface position (6 u.c.) (Å)	Surface position (10 u.c.) (Å)
1	Sr/La	0.0000	0.5836	0.4041
1	O	0.0000	0.1149	0.0955
2	O	1.9467	2.2120	2.2415
2	O	1.9467	2.2120	2.2415
2	Mn	1.9467	2.0472	2.0067
3	La/Sr	3.8933	3.9232	3.8835
3	O	3.8933	3.9050	3.9593
4	O	5.8400	5.8909	5.6348
4	O	5.8400	5.8909	5.6348
4	Mn	5.8400	5.7781	5.7984
5	La/Sr	7.7867	7.5902	7.6912
5	O	7.7867	7.7637	7.8046

In order to have a better idea of the evolution of the surface atom positions, the surface relative atomic positions as a function of the film thickness is given in Fig. 5.12 (a), which is normalized by the LSMO bulk lattice constant. Figure 5.12 (b) depicts the tolerance factor ($\Gamma = d_{(La/Sr)-O}/(\sqrt{2}d_{Mn-O})$) calculated by the atom position. Our LEED-IV refinement results show that the 6 u.c. LSMO film has the largest compression in the topmost unit cell, which gives a smaller tolerance factor (0.92) than the other films. The fact that the top layer is compressed more than the second layer could be due to the Sr segregation at the surface as well as broken symmetry. 6 u.c. LSMO has the largest compression, which may be related to it having the largest potential on its surface. This requires further study.

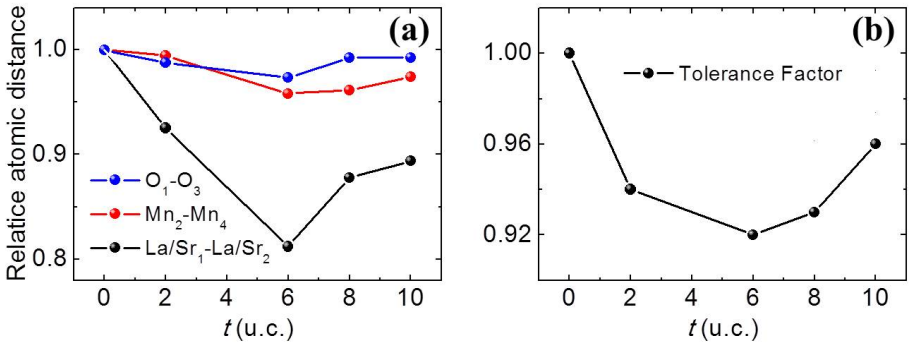

FIGURE 5.12: Evolution of the interlayer atom distances and the tolerance factor (Γ) with film thickness. The distances are normalized by LSMO bulk lattice constant.

LEED-IV evolution and structural refinement for LSMO films with different thicknesses indicate that the LSMO thin films of different thicknesses have similar compressed surface structures. Based on the surface structure from the LEED IV refinement and chemical composition from the ARXPS fitting results, the 10 u.c. LSMO film surface potential can be quantitatively calculated. Although the surface structure distortion can greatly reduce the polarity of the very top layer,

the calculation results show that the surface distortion only slightly reduces the surface potential.

5.4 Film properties interpretation

Our data in chapter 4 shows that the segregation at the interface and surface is roughly independent of LSMO film thickness. According to the layer-by-layer concentration of LSMO film achieved in chapter 4, we do believe that the substantial increase in Sr concentration from its bulk value would result in nonmetallic behavior not only at the surface but also at the interface, which is illustrated in Fig. 5.13 (c). In a previous section of this chapter, the bias shift demonstrates that the surfaces of LSMO films are none-metallic. Although we didn't prove that the interfaces of LSMO films are also none-metallic, we do believe that the interface between LSMO and STO is also non-metallic.

To further study the influence of high Sr concentration to the properties of LSMO films, the thickness dependence of the film conductivity is explained using the model in Fig. 5.13 (c). Figure 5.13 (a) shows the temperature dependence of the resistivity ρ of LSMO films with different thicknesses, which exhibits a metal-insulator transition (MIT) with reduced film thickness. When film thickness $t \leq 6$ u.c., LSMO films are insulating, shown by the increase in resistivity as the temperature decreases. When the $t \geq 7$ u.c., LSMO films show metallic behavior. For film thicknesses $t \leq 6$ u.c., the resistivity is too high and cannot be measured. With the measured resistivity results, the conductivities (σ) of the LSMO films (≥ 7 u.c.) at 6 K as a function of film thickness are shown in Fig. 5.13 (b). The thickness dependence of the conductivity shows that the conductivities of LSMO films are not constant but rather gradually increase with increasing film thickness. However, the thickness dependence of the conductivity can be modeled assuming that there is a certain thickness (n_0) of nonmetallic layers in a n u.c. LSMO film

such that only (n - n_0) thick films are conductive. As shown in Fig. 5.13 (d), the measured conductivity (σ) can be fitted to

$$\sigma = \sigma_{real} \cdot (n - n_0)/n \tag{5.1}$$

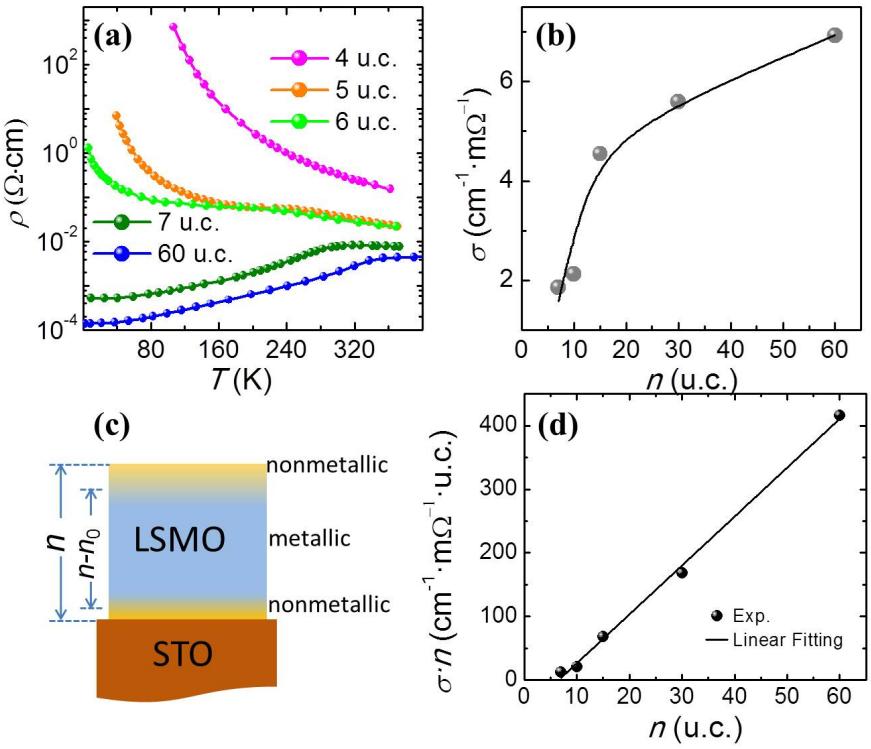

FIGURE 5.13: (a) Temperature dependence of the resitivity(ρ) of LSMO films with different thicknesses. (b) Thickness dependence of the conductivity (σ) measured at 6 K. (c) Schematic view of n u.c. LSMO film with a certain thickness (n_0) of nonmetallic layers near the surface and interface. (d) The thickness dependence of the measured conductivity (σ) times film thickness (n), measured at 6 K. The solid line is the fitting result with the suggested model by assuming a certain thickness (n_0) of nonmetallic layers near the surface and interface of LSMO films on STO (001)

Here σ_{real} is the constant real conductivity of the inside of the LSMO film. In other words, $\sigma \cdot$ n =σ_{real} *(n-n_0) can be fit with a linearly dependent n. The fitting result gives $n_0 = 6.5$ and $\sigma_{real} = 7.68$ ($\mathrm{m\Omega^{-1} \cdot cm^{-1}}$), which are comparable to the

measured critical thickness of the 6 u.c. film dead-layer and bulk conductivity ($\sim$ 11 $m\Omega^{-1} \cdot cm^{-1}$) for LSMO single crystals [135], respectively.

The layer-by-layer concentration of LSMO films not only suggests the existence of insulating layers, which had already been proven in this thesis, but also suggests that antiferromagnetism exists near the surface and interface, which has been seen by different groups. One such group used x-ray magnetic circular dichroism to verify the existence of a canted antiferromagnetic insulating phase in ultrathin LSMO films [151]. Another group used polarized neutron reflectometry to study the exchange bias effects of LSMO grown on STO, which is related to the antiferromagnetic structure formed in this part of the LSMO thin film [152]. Although the structural distortion needs to be considered in the antiferromagnetic insulating phase of LSMO films and is the main focus of the above studies, the stoichiometry change can have immense impact on LSMO films. The change of Sr doping can not only turn metal to insulator, but can also change ferromagnetism to antiferromagnetism.

5.5 Summary

In this chapter, my study of the chemical composition of ultrathin films of LSMO grown on STO (001) with atomic layer precision through a combination of $in-$ and $ex-situ$ microscopy and spectroscopy techniques is detailed. Our results reveal that there is a substantial increase in the Sr concentration from its bulk value both at the interface and surface, which suggests that the surface and interface have several nonmetallic layers. This should have an immense impact on the physical properties of the epitaxial films and heterostructures.

To prove the existence of the insulating layer, STS was applied to LSMO films with different thicknesses. For 4 u.c. LSMO, a gap is observed in the LT STS spectra. For the LSMO films with thicknesses $\geq$ 6 u.c., the novel bias shift is

observed in the LT STS spectra, which cannot exist in the metallic layers but is explained by the surface polarization due to Sr segregation. For 6 u.c. LSMO films, the bias shift is about -0.24 V higher than other films ($\sim$ -0.1 V). This is due to the 6 u.c. LSMO film being more insulating and which may therefore accumulate a higher potential between the interface and surface.

The surface structure of the LSMO films were studied with LEED, which demonstrated that the 6 u.c. LSMO film has the largest compression in the topmost unit cell, which gives a smaller tolerance factor (0.92) than the other film thicknesses. This could be related to the 6 u.c. LSMO film having the largest polarization. According to the layer-by-layer concentration of LSMO films and the existence of the persistent nonmetallic behavior near the surface of LSMO films, regardless their thickness, the thickness dependence of conductivity is well explained by a model that assumes a certain thickness (n_0) of nonmetallic layers in an n u.c. LSMO film such that only (n - n_0) u.c.'s provide constant conductivity.

Chapter 6

Introduce to the segregation theory and experiment discussion in LSMO

6.1 Introduction and motivation

Segregation has been studied for over half a century, being predicted by McLean in 1957 [153]. It was first discovered at grain boundaries in metal alloys and has been extensively studied due to the fact that the mechanical and chemical properties of the alloys can be dramatically affected by the segregation. The grain boundary is a defect of the crystal structure or the interface between two grains, or crystallites, in a polycrystalline material. The existence of a grain boundary can decrease the electrical and thermal conductivity of the material. A schematic illustration and image of a low angle grain boundary is shown in Fig. 6.1. Compared to the bulk crystal, grain boundaries usually have a higher Gibbs energy (grain boundary energy σ). Systems containing grain boundaries will tend to reduce this energy in many ways. One way for a system to reduce its total energy is in the interaction of the grain boundaries with other lattice defects such as solute or impurity atoms. As a consequence, these atoms accumulate (segregate) at grain boundaries to some extent. Once segregation appears, the chemical nature of the boundary becomes qualitatively different from the inside of the bulk.

Segregation has important effects on the overall properties of a material. For the metal alloys, segregation usually produces a deleterious effect on the quality, which can lead to grain boundary fracture as a result of temper brittleness, creep embrittlement, stress relief cracking of welds, hydrogen embrittlement, environmentally assisted fatigue, grain boundary corrosion, and some kinds of intergranular stress corrosion cracking [162]. Grain boundary segregation is a very important phenomenon, which not only has an effect on the metallic properties, but also has

an important impact on other polycrystalline material properties. For example, it may promote successful sintering of ceramic powders, and it also can dramatically reduce the electric conductivity of semiconductors and high-temperature superconductors [168, 169, 170, 171]. Grain boundary segregation in metal alloys have been deeply studied. Before moving on to discussing segregation in complex oxides material, the grain boundary segregation of metal alloys will be briefly introduced in the first part of this chapter.

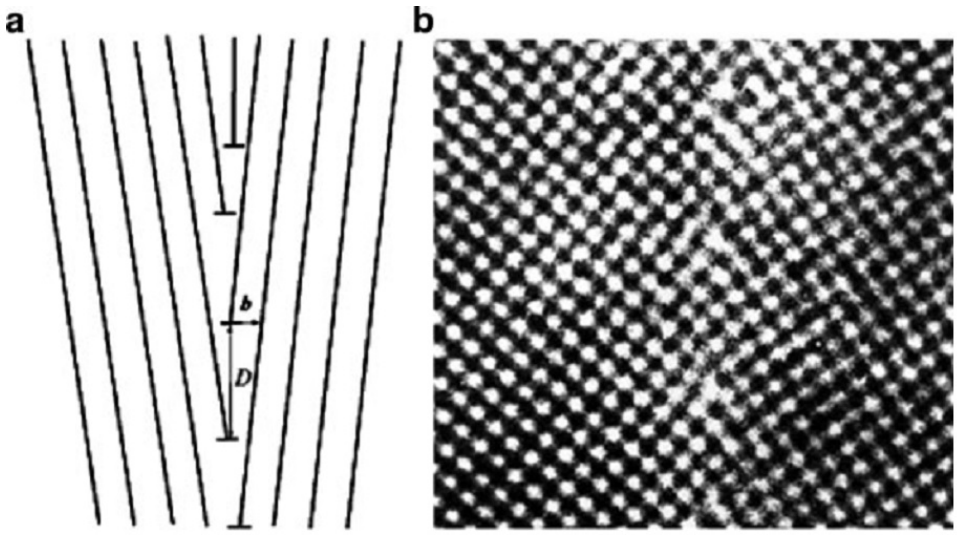

FIGURE 6.1: Structure of a low-angle grain boundary (a) schematic illustration; (b) image of a [100] low-angle grain boundary in molybdenum revealed by the high-resolution electron microscopy. [172]

There are two recognized types of segregation: equilibrium segregation and non-equilibrium segregation. To minimize the free energy in the segregation, one possible solution is the diffusion of elements from the bulk to the free surface, grain boundary, and interface, which is called equilibrium segregation. Non-equilibrium segregation was first theorized by Westbrook in 1964 [164]. Different from equilibrium segregation related to the minimization of the free energy, non-equilibrium segregation occurs as a result of the solutes coupling to vacancies during quenching

or the application of stress, and can also be due to solute accumulation at a moving interface [165]. Due to the different mechanisms, there is a distinguishable difference between non-equilibrium and equilibrium segregation. In the non-equilibrium case, the lowest energy state corresponds to a uniform solute distribution. As a result, the non-equilibrium segregation, which increases with increasing temperature, can be avoided by suitably heating the material to some temperature without further quenching. In contrast, the lowest energy state in a system naturally exhibits equilibrium segregation, and the extent of the segregation effect decreases with increasing temperature [154]. Although vacancies can be caused by quenching, component vacancies of a material, such as oxygen vacancies, are still included in the later equilibrium calculation. In this chapter, we mainly focus on equilibrium segregation.

Besides the segregation, there are two more important phenomena (phase separation and adsorption) for non-uniformity in the chemical composition of many materials, namely those of phase separation and adsorption. The difference can be clearly distinguished by the schematic diagrams of the three phenomena shown in Fig. 6.2. Adsorption describes the attraction and retention of the molecules of a substance on the surface of a liquid or solid resulting in a higher concentration of molecules on the surface shown in Fig. 6.2(a), which can influence the results of surface segregation experiments. Different from adsorption, phase separation and segregation are inhomogeneous for the material itself shown in Fig. 6.2 (b) and (c). Phase separation includes competing phases creating inhomogeneities in the bulk. However, the segregation enriches the chemical material constituents at a free surface or interface in a crystalline solid (including the crystalline films), as shown in Fig. 6.3 (a). In a polycrystalline solid, a segregation site can be a dislocation,

grain boundary, stacking fault, interface with a precipitate, or a secondary phase within the solid, shown in Fig. 6.3 (b).

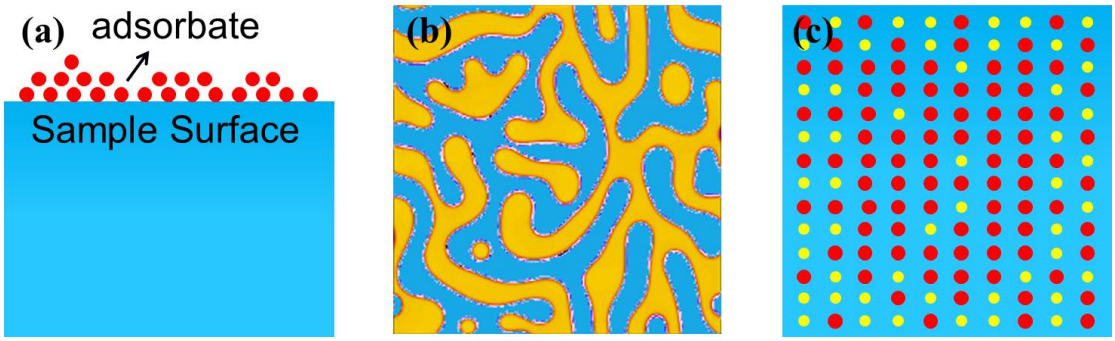

FIGURE 6.2: The schematic diagrams for (a) absorption, (b) phase separation, and (c) segregation.

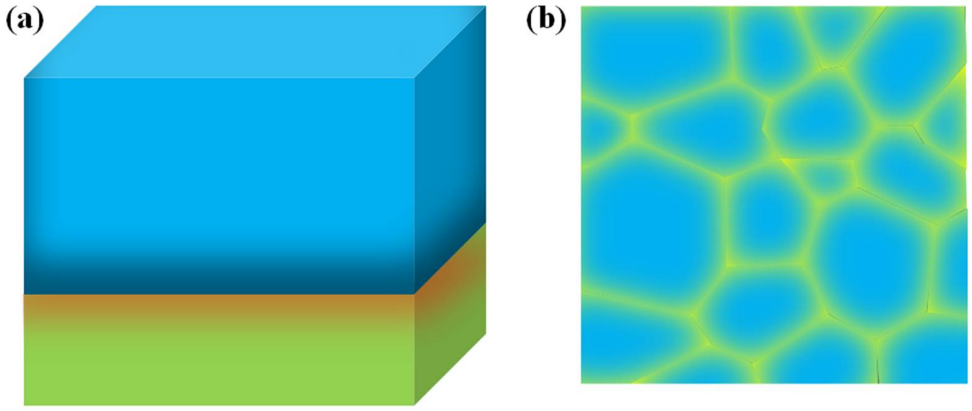

FIGURE 6.3: (a) Schematics of interface and surface segregation for a crystalline film; (b) Schematics of grain boundary segregation in a polycrstalline solid.

No grain boundary is observed with STEM in our LSMO films. Segregation to free surfaces and interfaces is therefore the main phenomena investigated in the second part of this chapter, focusing on theoretical and experimental segregation results in complex oxide materials and LSMO. For the transition metal oxides, segregation can be crucial to many properties, such as the overall device performance in a range of device applications, including solid oxide fuel cells, oxygen

permeation membranes, batteries, and magnetic, catalytic, ferroelectric materials [155, 156, 157, 158, 159, 160, 161]. For transition metal oxides, because the physical properties are strongly related to the doping [see Fig. 1.3], favorable segregation of dopants to the surface or interface of the material can lead to significant differences in composition between the surface/interface and the inside of films. In device designs, when specific bulk properties are needed, segregation can result in completely different properties, which reduces performance in the device or causes complete failure. Therefore, a better understanding of the mechanisms surrounding segregation is pivotal and can lead to better control of these effects in the future. Modeling potentials and related theories are still being developed to explain these segregation mechanisms for increasingly complex systems.

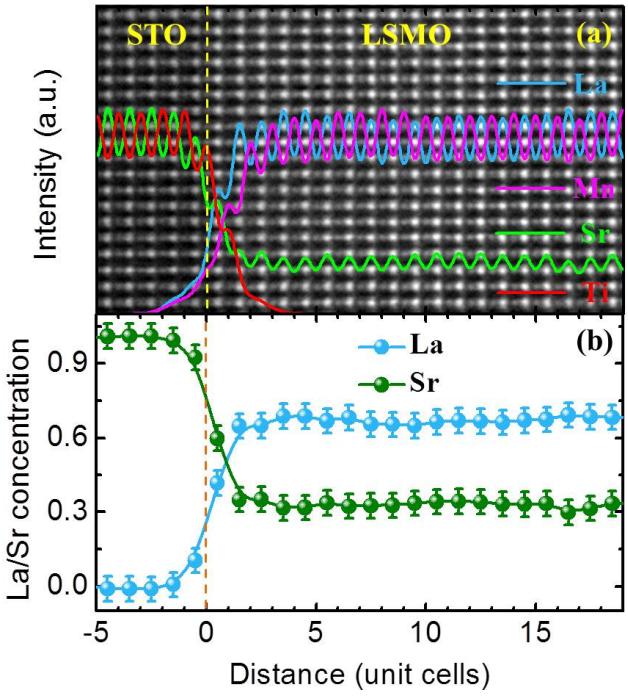

FIGURE 6.4: (a) HAAD-STEM image and EELS elemental profiles for La, Sr, Ti and Mn of 40 u.c. LSMO/STO interface. (b) The concentration profiles for La and Sr as a function of distance(unit cells) from the interface of 40 u.c. LSMO film.

6.2 Segregation in Metal alloys

Metallic materials have been used by mankind for eight millennia [166] and are still irreplaceable in many applications to this day. Though we have used them for much of our history, there is still ongoing research into understanding the mechanisms of the processes at every stage of the production and application of metals. The first attempts to describe segregation processes systematically were done by Agricola [167]. His reports can be regarded as the first observations of phenomena induced by grain boundary segregation.

6.2.1 Experimental Methods for Study of Grain Boundary Segregation

Grain boundary segregation has been detected by various methods both indirectly and qualitatively. These techniques include many experimental measurements, such as the electrode potential on grain boundary fractured surfaces, the variations of lattice parameter with varied grain size using X-rays, spectrographic analysis of material extracted from the grain boundary region, and so on [173]. However, the limitations of these measurement techniques mean that they cannot be used to fundamentally understand the grain boundary segregation. They are also not applicable to ternary or more complex systems, where the effects of individual elements may overlap. To study segregation in a quantitative way, the techniques used must satisfy two requirements, that they are suitable for the study of interfacial composition that enables a direct approach to the interface as well as localization of the analysis, and must also be able to give atomic resolution in at least one dimension. Therefore, there are typically two microscopic techniques used in the study of grain boundary segregation, that of analytical electron microscopy (AEM), which includes STEM, EELS and energy dispersive X-ray analysis (EDX) [174, 175, 176], and atom-probe field ion microscopy (AP FIM), which can achieve atomic spatial

resolution with a mass spectrometer [177]. In our previous experiment results, the interface segregation was studied by the STEM and EELS. Figure 6.4 is an example of this, where the interface segregation can be shown in (b) obtained from STEM and EELS results in (a).

6.2.2 Theoretical Study of Grain Boundary Segregation

As mentioned in the previous section, the appearance of equilibrium segregation is a result of inhomogeneities in the solid giving rise to sites for which solute atoms have a lower Gibbs energy. McLean was the first to develop a model to deal explicitly with the phenomenon of grain boundary segregation. Since then, there has been a steady effort to develop or improve the analytical models. Many groups still try to give better predictions or interpretations of interfacial segregation.

Theories of equilibrium segregation can be developed with two different approaches. One approach is a quantum method studying the system on the microscopic level. This approach deals with interactions between segregating species and the interface, as well as among the segregating species themselves. The other approach deals with the thermodynamics of the system, which provides useful interrelationships between the observable properties of the system in a macroscopic way.

For the microscopic approach, one can attempt to directly solve the Schrödinger equation. During the calculations, suitable approximations and processes are needed. For example, density functional theory (DFT) is well developed and is a typical method used. In 1965, modern DFT was developed with Kohn-Sham equations [197]. Later Walter Kohn was awarded the Nobel prize in chemistry for his development of the density functional theory. However, DFT was not considered accurate enough for calculations in quantum chemistry. In the 1990s, some approximations (such as generalized gradient approximation) used in the DFT calculation, which

greatly help DFT to be a better model with the exchange and correlation interactions [198].

The other way to approach the microscopics is with Molecular Mechanics based on the interatomic potentials further calculated by computer simulation methods, such as Molecular (or lattice) Statics, Molecular Dynamics, or Monte Carlo. These computational potentials are much more efficient than first principle techniques rooted in quantum mechanics, and enable simulations of systems that are several orders of magnitude larger both with respect to length and time scales. Previous attempts to develop a quantitative, microscopic theory have not been particularly successful. The first numerically derived surface segregation energies which appear quantitatively reasonable have been obtained by Foiles et al. [199]. The phase field method has recently emerged as a powerful computational approach to solve interface problems in materials at the mesoscale level. Phase field models were first introduced by Fix [200] and Langer [201], which is a phenomenological phase field model. Later, another phase field model was derived by Chen [202] and Wang [203] from Khachaturyan's microscopic theory [204, 205].

Segregation calculations also can be achieved by using thermodynamic models. Compared with the quantum models, these statistical thermodynamic calculations are simpler, but some have been applied to segregation with considerable success. Based on the model built by McLean, many efforts have made done to thermodynamic models, because of the simplicity it provides in the definitions of the relevant model parameters. Besides, the simplicity of these thermodynamic models help us to understand the driving forces for segregation more easily provides in the definitions of the relevant model parameters. Based on the model built by McLean, the majority of these efforts have made use of the regular solution approximation, because of the simplicity it. Therefore, in the following part of this section, we give a

brief introduction to the thermodynamic approaches, though detailed explanations of the calculations only are explained in the original references.

The first and one of the simplest segregation models was built by McLean [153]. In binary metallic systems, by partitioning the solute atoms between lattice sites and a fixed number of noninteracting grain-boundary sites, the energy of the system can be minimized, which gives

$$\frac{\chi_g}{\chi_g^o - \chi_g} = \frac{\chi_b}{1 - \chi_b} exp(-\Delta G/KT) \tag{6.1}$$

Here, χ_g is the solute mole fraction at the grain boundary; χ_b is the solute mole fractions in the bulk; χ_g^o is the saturation value for χ_g; ΔG is the free energy of segregation; k is Boltz-mann's constant; and T is the temperature of the system.

ΔG can be estimated by Seah and Handros's work [182], which extends the theory of Brunauer *et al* [183].

$$\Delta G = \Delta G' + \Delta G_s \tag{6.2}$$

Here, ΔG_s is the free energy of precipitation for the soluble substances, which is given by:

$$\Delta G_s = RTln\chi_b^o \tag{6.3}$$

$\Delta G'$, the free energy for segregation without precipitation, is given by:

$$\frac{\chi_g}{\chi_g^o - \chi_g} = \frac{\chi_b}{\chi_b^o} exp(-\Delta G'/KT) \tag{6.4}$$

where χ_b^o is the solute solubility.

In the previous model, only the elastic energy contribution was considered. The interactions between segregating species were first considered by Fowler in his theory [184], where

$$\frac{\chi_g}{\chi_g^o - \chi_g} = \chi_b exp[-\Delta G - Z_1 W(\chi_g/\chi)_g^o]/kT \tag{6.5}$$

Here, W is the interaction energy and Z_1 is the coordination number for the adsorbate in the grain boundary layer. Further developments of Fowler's theory were done by Guttman [185]. In his work, he presented a theory to allow for interactions between co-segregating species in ternary and higher-order systems, which further modified the results:

$$\frac{\chi_{gi}}{\chi_{gi}^{o}} = \frac{\chi_{bi} exp(-\Delta G_i/kT)}{1 + \sum[exp(-\Delta G_i/kT) - 1]} \tag{6.6}$$

Here, χ_{gi} is the molar fraction for co-segregating species. When two segregating species appear in one system χ_{b1} and χ_{b2}, the free energies for their segregations ΔG_i can be given by:

$$\begin{aligned} \Delta G_1 &= \Delta G_1^o + \tau_{12}\chi_{g2} \\ \Delta G_2 &= \Delta G_2^o + \tau_{12}\chi_{g1} \end{aligned} \tag{6.7}$$

where τ_{12} is an interaction coefficient and ΔG_i^o are the free energies of segregation for the species. If the interaction energies (τ_{ij},) disappear (i.e. equal to zero), the result here is the same as with McLean's model.

Another important model was built by Defay and Prigogine [189]. Although they neglect the elastic effects, this model was appropriate to represent segregation behavior of liquid solutions. However, as was pointed out by Burton and Machlin, neither the McLean nor the Defay models were able to give qualitatively correct predictions of grain boundary segregation with binary solid alloys [190]. The reason for this is that one of them only considers chemical contributions to the heat of segregation, while the other ignores the elastic contributions. As a result, the considerations of a combined model in which the chemical and elastic contributions to the heat of segregation were first recognized by Wynblatt and Ku [186]. The total free energy is given by:

$$\Delta G = \Delta G_{int} + \Delta G_{bin} + \Delta G_{\epsilon} \tag{6.8}$$

Each of these terms is given by:

$$\Delta G_{int} = (\gamma_1 + \gamma_2)S \tag{6.9}$$

$$\Delta G_{bin} = \Delta G_m / 3\chi_{b1}\chi_{b2} \tag{6.10}$$

$$\Delta G_{\epsilon} = -24\pi K' G r_1 r_2 (r_1 - r_2)^2 / (4G r_1 + 3K' r_2) \tag{6.11}$$

where γ_i is the interfacial energy; S is the interface area per atom; ΔG_m is the free energy of mixing of the binary solution, K is the bulk modulus of the solute, G is the shear modulus of the solvent, and r_l and r_2 are the effective radii of the solvent and solute, respectively.

In this model, there are three principal contributions responsible for segregation in solid metallic alloys. The chemical driving force includes three distinct contributions, the ΔG_{int} being the interfacial energy which depends on the difference between the surface/interfacial energies of the pure components (i.e., a surface energy driving force), and the ΔG_{bin} as a binary interaction contribution which depends on the regular solution constant (i.e., an interatomic interaction driving force). The third driving force ΔG_{ϵ} is the elastic strain energy, which was first identified by McLean. For this term, the contribution is associated with the degree of misfit of the solute in solution. In ideal solution case, the ΔG_{bin} and ΔG_{ϵ} contributions can vanish.

After that, there are several refinements and modifications of these models that have been proposed. For example, Lee and Aaronson first addressed the effects of interface structure and energy anisotropy [187, 188]. However, the major driving forces for segregation in metal alloys do not change much because the phenomenological descriptions of equilibrium segregation is qualitatively the same for all types of interfaces. The differences are rooted in the model values of equilibrium grain

boundary segregation particular to thethermodynamic parameters resulting from different structural/bonding conditions for individual cases [178, 179]. Because the results for those models are for the non-ideal case, the composition profile, or the changing segregation concentration from the surface to the bulk, is not necessarily limited to the surface. In other words, the segregation is not limited to the first two layers but can penetrate deeper. This is true even if only the first nearest neighbor interactions are included. For values of the parameters usually employed in these calculations, segregation is typically negligible beyond the third or fourth layer from the surface.

6.3 Present Results and Discussion for LSMO film

LSMO is one important group of the complex oxide materials. In the previous experimental result of LSMO films in chapter 4, the segregation is already proved to be existing on the surface and at the interface. Interfacial segregation for these systems describes the compositional heterogeneity that exists between the bulk and interface due to interfacial effects that are distinct from the bulk. Alternatively, surface segregation is the enrichment at the surface as a result of diffusion of elements from the bulk moving to the surface region. When thermodynamic equilibrium is reached, minimization of the total free energy at a given temperature may result in the segregation on the surface and interface. The amount of segregation enrichment depends on the growth conditions such as temperature, oxygen pressure.

The presence of inhomogeneity at the surface can be due to Sr diffusion from the bulk or absorption other elements such as carbon from the ambient background. The adsorption can strongly influence the experimental study of the surface equilibrium segregation. To investigate the surface segregation, ultrahigh vacuum (UHV) of at least 10^{-10} Torr is required to reduce the influence of adsorption. Sur-

face sensitive characterization probes usually include Auger electron spectroscopy (AES) and photoelectron spectroscopies (XPS, UPS, and ESCA). In chapter 4, the surface segregation of LSMO films was analyzed by ARXPS.

6.3.1 Segregation driving forces in LSMO films

Because of differences in the nature of ceramics and metals, segregation theories for metals cannot be directly extended to the case of ceramics [191]. The ionic nature of ceramic oxides leads to the formation of electrostatic potentials at interfaces related to the defects and structure, and there is no analogy in metals. Furthermore, doping with an aliovalent ion in the complex oxides leads to a higher heat of solution in ceramics than for that of metals. The heat of solution in ceramics is mostly related to vacancy formation rather than the strain energy which is important in the case of metals. Also, deviations from normal stoichiometry give rise to temperature and oxygen partial pressure dependent variations in composition. Doping in these manners with ceramics can produce a whole range of new variables, which do not exist metallic alloys. Thus, electrostatic contributions need be considered in the theory of interfacial segregation in complex oxides, such as perovskites.

Frenkel first pointed out that the existence of space charge regions at interfaces in ionic solids lead to several nanometers of compositional heterogeneities extending further into the materials [192]. Frenkel's initial model and subsequent refinements were further improved by Kliewer and Koehler [195]. All these methods have approached the problem by considering the space charge effect as the only major driving force for segregation. Yan *et al.* [193, 194] further extended Kliewer and Koehler's approach by including additional elastic and dipolar effects. All these theories were applied to alkali halides under equilibrium conditions.

Based on the approach used by Frenkel, Desu and Payne developed a model for equilibrium interfacial segregation in pure and doped perovskite materials [196].

The approach used regular solution approximations and considered space charge effects as the major driving force for segregation. For dopant segregation, elastic and electrostatic driving forces were considered. Giving the right solution to the model in the doped system requires fully considering the charge neutrality conditions and the strain energy contribution. One interesting prediction of this model is that the thickness of the space charge layer (i.e. the decay length of segregation) decreases with the increase of growth temperature, which was proved by comparison of the calculated values and experimental results in $BaTiO_3$.

There are some segregation calculations directly for LSMO. Recently, Harrison has hypothesized that the surface charging of LSMO has its origin in the segregation of Sr at the surface of LSMO [67]. On the (100) surface of LSMO films, with a uniform distribution of Sr and La cations, the charge of per site in $La_{1-x}Sr_xO$ planes is +e(1-x). Harrison constructed an electrostatic model of the interaction of Sr with the charged surfaces of LSMO. With this model, the total electrostatic surface energy can be calculated, which shows that this energy could be minimized by depleting the La and increasing the Sr concentration at or near the surface of LSMO. In this paper, he predicted an La concentration of $0.65(1 - 0.41^n)$ or $0.65(1 - exp(-0.89)^n)$, where the decay length quantitatively equals the surface segregation of LSMO, as shown in Table 4.4. Although bulk LSMO is metallic, this result would seem to give compelling evidence that the surface is nonmetallic, which is also proved by our STS experimental results in chapter 5, and the electrostatic energy is a source of the segregation of the dopant at the surface of LSMO. However, according to the Harrison model, the decay length is fixed, but this result is contradictory to the prediction made in Desu and Payne's model, that the decay length of the segregation decreases with increasing temperature. Another

weak point of this model is its failure to predict the amount of segregation, which is due to it neglecting the elastic energy as another driving force.

The importance of elastic energy was fully emphasized by another segregation calculation and experiment related to LSMO done by Yildiz *et al.* [69]. The density functional theory (DFT) calculation considers both the elastic energy and electrostatic energy as the driving forces for the surface segregation, which suggests that Sr segregation toward the surface can minimize the elastic energy due to a mismatch of the dopant and host cation sizes. It aslo minimizes the electrostatic energy due to the interactions between the dopants and charged defects at the surface and the space charge zone near the surface, in addition to the surface polarity effects. They also experimentally study the elastic energy differences by changing the radius of selected dopants (Ca, Sr, Ba) with respect to the host cations (La, Sm) while maintaining the same charge in an $LnMnO_3$ system. A smaller size mismatch between the host and dopant cations was found to suppress segregation effects. They also studied the oxygen pressure influence on the elastic and electrostatic energy.

LSMO is a part of a complex family of materials which could be important in future technological application. With Sr doping 0.33, LSMO bulk is the metallic state. However, the elastic energy can be the initial driving force for the Sr segregation in LSMO films, which induces the nonmetallic property of LSMO film. While, in the nonmetallic layers of LSMO films, the electrostatic energy can further enhance the segregation effect. For complex oxides, current models still cannot fully solve the segregation problem. However, it is undeniable that both the elastic and electrostatic interactions must be quantitatively taken into account for segregation calculations in complex materials.

6.3.2 Surface segregation in LSMO films

In general, the phenomenological description of free surface segregation is similar to that for interface segregation. In the aforementioned models, there is no distinct difference for the basic driving forces between the surface and interface segregations. Those models, originally designed for interface segregation, usually can be extended to use with surface segregation. The McLean model is a good example for this. Although it was originally designed for the segregation at grain boundaries, it can also be applicable to segregation at free surfaces [180, 181]. If the amount of segregation at the surface (only the topmost layer) is 0, denoted in fractions of a monolayer, then

$$\theta/(1-\theta) = \chi exp(-\Delta E_{Seg}/kT) \tag{6.12}$$

For a binary alloy with two components A and B, 0 is the surface layer concentration of component B. Here, $\chi = \chi_B^b/(1-\chi_B^b)$, and χ_A^b) and χ_B^b) are the bulk concentrations of A and B respectively. ΔE_{seg} is the system energy change when an atom of type B originally in the bulk changes position with an A atom originally at the surface. In this model, all sites are assumed to have the same environment. A positive value of E_{seg} corresponds to the enrichment of A at the surface, and a negative value for B enrichment.

In chapter 4, by comparing the surface and interface segregation, we already concluded that the deviation of Sr concentration at the interface is small (only 1 u.c.), while in proximity to the free surface it is more severe (3 u.c.)[see Fig. 4.9]. In other words, there is a difference in the Sr segregation decay length between the interface and the free surface of films. One possible reason for the difference is that the interface is metallic, while the free surface is nonemetallic. As the results, there fundamental difference between the driving forces for the interface and the surface.

Besides, the different structures, which has a larger distortion on surface as shown in section 5.3, and the different chemical environments such as oxygen vacancy of the surface and interface can further influence the segregation. Although similar theories can be used to explain the surface and interface segregation, the distinguish difference of the structure and chemical composition between the surface and interface can cause a segregation difference between the two zones.

6.4 Summary

In this chapter, the importance of segregation in many materials was discussed. Grain boundary segregation was first investigated in metal alloy systems and has been intensively studied. The experimental tools for probing the grain boundary were also introduced in the beginning of the chapter. The theory for equilibrium segregation was first developed by McLean, but it cannot provide qualitatively correct predictions for the segregating components at binary solid alloy surfaces due to only including the elastic contributions to the driving force. Thermodynamic models were also discussed. In the later models, the major driven forces for the grain boundary segregation in metal alloys were made to include both the elastic strain energy as well as the chemical driving force (i.e. the interfacial energy and the binary interaction).

Using the previous theory calculations, the models built for the interface can usually be extended to understand the surface. Although the driving forces considered are the same, the formula needs to be modified. In our experimental results, the decay lengths at the surface and interface are completely different. This may be due to needing a different formula for the calculation or being able to include different structures and vacancies between the surface and interface.

Though it is not important with metals, the segregation model in complex oxide materials needs to consider the electrostatic energy as one of the important driving

forces. In the early days of segregation studies, Frenkel pointed out the importance of space charge regions at interfaces in ionic solids. Yan *et al*. extended the model, and built the first approach to including electrostatic, elastic, and dipolar effects, which gave a more precise prediction for ceramic oxides materials. To address the segregation in pure and doped perovskite materials, Desu and Payne developed a model for equilibrium interfacial segregation, where elastic and electrostatic driving forces were considered.

For segregation calculations in LSMO films, there are two important papers. Harrison's work only considered surface charging in the origin of the segregation of Sr at the surface of LSMO. In this model, the decay length is qualitatively the same as those seen in our experimental results. However, the decay length does not change with the growth conditions, which contradicts with the predictions of Desu and Payne's model. Without considering elastic energy, Harrison's model cannot predict the change of dopants in the segregation. Another important segregation calculation and experiment related to LSMO was done by Yildiz *et al*.. The importance of elastic energy was proven in their work by changing dopants in their experiment. They used DFT calculations to further explain the experiment results, which also consider the elastic and electrostatic energy as the major driving forces.

References

[1] https://en.wikipedia.org/wiki/Abundance_of_the_chemical_elements

[2] X. Wu, C. Zhang, P. Goldberg, D. Cohen, Y. Pan, T. Arpin, and O. Bar-Yosef, Science **336**, 1696 (2012).

[3] J. G. Bednorz, and K. A. Müller, Zeitschrift für Physik B **64**, 189 (1986).

[4] C. W. Searle, and S. T. Wang, Can. J. Phys. **47**, 2703 (1969).

[5] H. Schmid, Ferroelectrics **162**, 317 (1994).

[6] M. A. Laguna-Bercero, Journal of Power Sources **203**, 4 (2012).

[7] V. Anisimov, and Y. Izyumov, Electronic Structure of Strongly Correlated Materials, Springer (2010).

[8] G. H. Jonker and J. H. Van Santen, Physica **16**, 337 (1950).

[9] M. Imada, A. Fujimori, and Y. Tokura, Rev. Mod. Phys. **70**, 1039 (1998).

[10] S. Jin, T. H. Tiefel, M. McCormack, R. A. Fastnacht, R. Ramesh and L. H. Chen, Science **264**, 413 (1994).

[11] M. N. Baibich, J. M. Broto, A. Fert, F. Nguyen Van Dau, F. Petroff, P. Etienne, G. Creuzet, A. Friederich, and J. Chazelas Phys. Rev. Lett. **61**, 2472 (1988).

[12] G. Binasch, P. Grünberg, F. Saurenbach, and W. Zinn, Phys. Rev. B **39**, 4828 (1989).

[13] The Nobel Prize in Physics 2007, NobelPrize.org.

[14] J. -H. Park, E. Vescovo, H. -J. Kim, C. Kwon, R. Ramesh and T. Venkatesan, Nature **392**, 794 (1998).

[15] S. A. Wolf, D. D. Awschalom, R. A. Buhrman, J. M. Daughton, S. von Molnŕ, M. L. Roukes, A. Y. Chtchelkanova, D. M. Treger, Science **294**, 1488 (2001).

[16] S. Okamoto and A. J. Millis, Nature **428**, 630 (2004).

[17] C. N. R. Rao and A. K. Raychaudhuri, Colossal Magnetoresistance, Charge Ordering and Related Properties of Manganese Oxides (Eds. C.N.R. Rao and B. Raveau), Singapore: World Scientific (1998).

[18] A. -M. Haghiri-Gosnet and J. -P. Renard, J. Phys. D: Appl. Phys.**36**, R127 (2003).

[19] N. Nakagawa, H. Y. Hwang, and D. A. Muller, Nature Materials. **5**, 204 (2006).

[20] P. Zubko, S. Gariglio, M. Gabay, P. Ghosez, and J-M Triscone, Annual Review of Condensed Matter Physics**2**, 141 (2011).

[21] V. M. Goldschmidt, Die Naturwissenschaften **21**, 477 (1926).

[22] Handbook of magnetism and advanced magnetic materials: Spintronics and magnetoelectronics, (Eds, Helmut Kronmüller, Stuart Parkin) John Wiley ℘ Sons (2007).

[23] H. A. Jahn and E. Teller, Proc. R. Soc. London A,**161**, 220 (1937).

[24] H. Sawada, Y. Morikawa, K. Terakura, and N. Hamada, Phys. Rev. B **56**, 12154 (1997).

[25] Y. Tomioka and Y. Tokura, Phys. Rev. B **70**, 014432(2004).

[26] J. Stahn, J. Chakhalian, Ch. Niedermayer, J. Hoppler, T. Gutberlet, J. Voigt, F. Treubel, H-U. Habermeier, G. Cristiani, B. Keimer, and C. Bernhard, Phys. Rev. B **71**, 140509(R) (2005).

[27] M. Huijben, L. W. Martin, Y. -H. Chu, M. B. Holcomb, P. Yu, G. Rijnders, D. H. A. Blank, and R. Ramesh, Phys. Rev. B **78**, 094413 (2008).

[28] J. B. Goodenough, Phys. Rev.**100**, 564 (1955)

[29] C. Zener, Phys. Rev.**81**, 440 (1951)

[30] P. W. Anderson, and H. Hasegawa, Phys. Rev.**100**, 675 (1955)

[31] P. G. de Gennes , Phys. Rev.**118**, 141 (1960)

[32] A. Ohtomo and H. Y. Hwang, Nature **427**, 423 (2004).

[33] S. Thiel, G. Hammer, A. Schmehl, C. W. Schneider, and J. Mannhart, Science **313**, 1942 (2006).

[34] A. Brinkman, M. Huijben, M. van Zalk, J. Huijben, U. Zeitler, J. C. Maan, W. G. van der Wiel, G. Rijnders, D. H. A. Blank and H. Hilgenkamp, Nature Materials **6**, 493 (2007).

[35] M. Ben Shalom, C. W. Tai, Y. Lereah, M. Sachs, E. Levy, D. Rakhmilevitch, A. Palevski, and Y. Dagan, Phys. Rev. B **80**, 140403(R) (2009).

[36] N. Reyren, S. Thiel, A.D. Caviglia, L. Fitting Kourkoutis, G. Hammerl, C. Richter, C.W. Schneider, T. Kopp, A.-S. Retschi, D. Jaccard, M. Gabay, D. A. Muller, J.-M. Triscone, J. Mannhart, Science **317**, 1196 (2007).

[37] J. A. Bert, B. Kalisky, C. Bell, M. Kim, Y. Hikita, H. Y. Hwang and K. A. Moler, Nature Physics **7**, 767 (2011).

[38] N. Kida, H. Yamada, H. Sato, T. Arima, M. Kawasaki, H. Akoh, and Y. Tokura, Phys. Rev. Lett. **99**, 197404 (2007).

[39] A. Savoia, D. Paparo, P. Perna, Z. Ristic, M. Salluzzo, F. Miletto Granozio, U. Scotti di Uccio, C. Richter, S. Thiel, J. Mannhart, and L. Marrucci, Phys. Rev. B **80**, 075110 (2009).

[40] B. R. K. Nanda and S. Satpathy, Phys. Rev. B **81**, 224408 (2010).

[41] R. H. Liu, W. L. Lim, and S. Urazhdin, Phys. Rev. Lett. **110**, 147601 (2013).

[42] J. Chakhalian, J. W. Freeland, A. J. Millis, C. Panagopoulos, and J. M. Rondinelli, Reviews of Modern Physics **86** 1189 (2014).

[43] Y. Tokura and N. Nagaosa, Science 288, 462 (2000).

[44] A. Tebano, C. Aruta, S. Sanna, P. G. Medaglia, G. Balestrino, A. A. Sidorenko, R. De Renzi, G. Ghiringhelli, L. Braicovich, V. Bisogni, and N. B. Brookes, Phys. Rev. Lett. **100**, 137401 (2008).

[45] B. Cui, C. Song, F. Li, G. Y. Wang, H. J. Mao, J. J. Peng, F. Zeng, and F. Pan, Scientific Reports **4** 4206 (2014).

[46] N. M. Nemes, M. J. Calderón, J. I. Beltrán, F. Y. Bruno, J. García-Barriocanal, Z. Sefrioui, C. León, M. García-Hernndez, M. C. Muñoz, L. Brey, and J. Santamaría, Adv. Mater. **26** 7516 (2014).

[47] D. Preziosi, M. Alexe, D. Hesse, and M. Salluzzo, Phys. Rev. Lett. **115**, 157401 (2015).

[48] H. Doğanay, I. P. Krug, J. Schubert, S. Cramm, D. M. Gottlob, F. Nickel and C. M. Schneider, Europhysics Letters **109** 67007 (2015).

[49] R. K. Zheng, Y. Wang, H. L. W. Chan, C. L. Choy, and H. S. Luo Phys. Rev. B **75**, 212102 (2007).

[50] J. Z. Sun, D. W. Abraham, R. A. Rao, and C. B. Eom, Appl. Phys. Lett. **74**, 3017 (1999).

[51] C. Aruta, G. Ghiringhelli, A. Tebano, N. G. Boggio, N. B. Brookes, P. G. Medaglia, and G. Balestrino, Phys. Rev. B **73**, 235121 (2006).

[52] A. Tebano, C. Aruta, P. G. Medaglia, F. Tozzi, G. Balestrino, A. A. Sidorenko, G. Allodi, R. De Renzi, G. Ghiringhelli, C. Dallera, L. Braicovich, and N. B. Brookes, Phys. Rev. B **74**, 245116 (2006).

[53] Y. Takamura, R. V. Chopdekar, E. Arenholz and Y. Suzuki, Appl. Phys. Lett. **92**, 162504 (2008).

[54] G. Colizzi, A. Filippetti, F. Cossu and V. Fiorentini, Phys. Rev. B **78**, 235122 (2008).

[55] C. Adamo, X. Ke, H. Q. Wang, H. L. Xin, T. Heeg, M. E. Hawley, W. Zander, J. Schubert, P. Schiffer, D. A. Muller, L. Maritato and D. G. Schlom, Appl. Phys. Lett. **95**, 112504 (2009).

[56] D. Pesquera, G. Herranz, A. Barla, E. Pellegrin, F. Bondino, E. Magnano, F. Sánchez and J. Fontcuberta, Nature Communications **3**, 1189 (2012).

[57] B. Cui, C. Song, G. Y. Wang, H. J. Mao, F. Zeng, and F. Pan, Scientific Reports **3**, 2542 (2013).

[58] F. Sandiumenge, J. Santiso, L. Balcells, Z. Konstantinovic, J. Roqueta, A. Pomar, J. P. Espinós, and B. Martínez, Physical Review Letters **110**, 107206 (2013).

[59] A. Vailionis, H. Boschker, Z. Liao, J. R. A. Smit, G. Rijnders, M. Huijben and G. Koster, Applied Physics Letters **105** 131906 (2014).

[60] J. Heidler, C. Piamonteze, R. V. Chopdekar, M. A. Uribe-Laverde, A. Alberca, M. Buzzi, A. Uldry, B. Delley, C. Bernhard, and F. Nolting, Physical Review B **91** 024406 (2015).

[61] F. Y. Bruno, J. Garcia-Barriocanal, M. Varela, N. M. Nemes, P. Thakur, J. C. Cezar, N. B. Brookes, A. Rivera-Calzada, M. Garcia-Hernandez, C. Leon, S. Okamoto, S. J. Pennycook, and J. Santamaria, Physical Review Letters **106** 147205 (2011).

[62] O. Shapoval, S. Hühn, J. Verbeeck, M. Jungbauer, A. Belenchuk, and V. Moshnyaga, Journal of Applied Physics **113** 17C711 (2013).

[63] X. Yin, M. A. Majidi, X. Chi, P. Ren, L. You, N. Palina, X. Yu, C. Diao, D. Schmidt, B. Wang, P. Yang, M. B. H. Breese, J. Wang and A. Rusydi, NPG Asia Materials **7** e196 (2015).

[64] H. Boschker, M. Huijben, A. Vailionis, J. Verbeeck, S. van Aert, M. Luysberg, S. Bals, G. van Tendeloo, E. P. Houwman, G. Koster, D. H. A. Blank, G. Rijnders, Journal of Physics D-Applied Physics **44** 205001 (2011).

[65] M. Huijben, Y. Liu, H. Boschker, V. Lauter, R. Egoavil, J. Verbeeck, S. G. E. te Velthuis, G. Rijnders and G. Koster, Adv. Mater. Interfaces **2**, 1400416 (2015).

[66] H. Dulli, P. A. Dowben, S. -H. Liou, and E. W. Plummer, Phys. Rev. B **62**, R14629(R) (2000).

[67] W. A. Harrison, Phys. Rev. B **83**, 155437 (2011).

[68] Z. Li, M. Bosman, Z. Yang, P. Ren, L. Wang, L. Cao, X. Yu, C. Ke, M. B. H. Breese, A. Rusydi, W. Zhu, Z. Dong, and Y. L. Foo, Adv. Funct. Mater. **22**, 4312 (2012).

[69] W. Lee, J. W. Han, Y. Chen, Z. Cai, and B. Yildiz, J. Am. Chem. Soc. **135**, 7909 (2013).

[70] H. Boschker, J. Verbeeck, R. Egoavil, S. Bals, G. v. Tendeloo, M. Huijben, E. P. Houwman, G. Koster, D. H. A. Blank, G. Rijnders, Advanced Functional Materials **22** 2235 (2012).

[71] R. Peng, H. C. Xu, M. Xia, J. F. Zhao, X. Xie, D. F. Xu, B. P. Xie, and D. L. Feng, arxiv: 1301.4822 (2013).

[72] R. P. Borges, W. Guichard, J. G. Lunney, J. M. D. Coey, and F. Ott, J. Appl. Phys. **89**, 3868 (2001).

[73] B. Wang, L. You, P. Ren, X. Yin, Y. Peng, B. Xia, L. Wang, X. Yu, S. M. Poh, P. Yang, G. Yuan, L. Chen, A. Rusydi, and J. Wang, Nature Communications **4**, 2778 (2013).

[74] R. Peng, H. C. Xu, M. Xia, J. F. Zhao, X. Xie, D. F. Xu, B. P. Xie, and D. L. Feng, Applied Physics Letters **104** 081606 (2014).

[75] Z. Liao, F. Li, P. Gao, L. Li, J. Guo, X. Pan, R. Jin, E. W. Plummer, and J. Zhang, Phys. Rev. B **92**, 125123 (2015).

[76] J. Hemberger, A. Krimmel, T. Kurz, H. -A. Krug von Nidda, V. Yu. Ivanov, A. A. Mukhin, A. M. Balbashov, and A. Loid, Physical Review B **66**, 094410 (2002).

[77] P. Wynblatt, R. C. Ku, in Interfacial Segregation (Eds. W.C. Johnson, J.M. Blakely), American Society for Metals, Metals Park (1979)

[78] Surfaces and Interfaces of Ceramic Materials (Eds. L.C. Dufour and C. Monty), Springer (1989).

[79] D. Pesquera, M. Wojcik, E. Jedryka, V. Laukhin, N. Dix, F. Sánchez, G. Herranz and J. Fontcuberta1, Advanced Materials Interfaces **1** 1400079 (2014).

[80] J. Peng, C. Song, F. Li, B. Cui, H. Mao, Y. Wang, G. Wang, and F. Pan, ACS Applied Materials and Interfaces **7** 17700 (2015).

[81] K. Lv, H. P. Zhu, W. Q. Zou, F. M. Zhang and X. S. Wu, Journal of Applied Physics **117** 185305 (2015).

[82] T. H. Maiman, Nature **187**, 493 (1960).

[83] D. Dijkkamp, T. Venkatesan, X. D. Wu, S. A. Shaheen, N. Jisrawi, Y. -H. Min-Lee, W. L. McLean, and M. Croft, Appl. Phys. Lett **51**, 619 (1987).

[84] J. Chakhalian, etc, Scientific Themes page. Retrieved from http://comp.uark.edu/ jchakhal/REED.htm.

[85] A. Zangwill, Physics at Surfaces (Cambridge University Press, Cambridge, 1988).

[86] J. B. Pendry, D. K. Saldin, K. Heinz, K. Miiller, and N. Bickel, Phys. Rev. Lett. **57**, 2951 (1986).

[87] P. J. Rous, and J. B. Pendry,Surf. Sci. **219**, 355 (1989)

[88] P. J. Rous, and J. B. Pendry, Surf. Sci. **219**, 373 (1989)

[89] P. J. Rous, Prog. Surf. Sci. **39**, 3 (1992).

[90] J. B. Pendry, J. Phys. Chem. **13**, 937 (1980).

[91] Retrieved from http://hyperphysics.phy-astr.gsu.edu/hbase/solids/squid.html.

[92] D. Briggs and J. C. Riviere. "Practical Surface Analysis", Second edn., Vol. 1 (Eds. and M. P. Seah), Wiley, Chichester (1990).

[93] J. F. Moulder, W. F. Stickle, P. E. Sobol, and K. D. Bomben, "Handbook of X Ray Photoelectron Spectroscopy", J. Chastain, Perkin Elmer Corp., Eden Prairie, MN (1992)

[94] C. D. Wagner, A. V. Naumkin, A. Kraut-Vass, J. W. Allison, C. J. Powell, J. R. Jr. Rumble, NIST Standard Reference Database 20, Version 3.4 (Web Version) (http:/srdata.nist.gov/xps/) (2003).

[95] D. Briggs, XPS: Basic Principles, "Spectral Features and Qualitative Analysis", in: D. Briggs, J.T. Grant (Eds.), "Surface Analysis by Auger and X-ray Photoelectron Spectroscopy", IM Publications, Chichester (2003).

[96] H. G. J. moseley, Philosophical Magazine **27**, 703 (1914)

[97] B. L. Henke, Phys. Rev. A, **6**, 94 (1972)

[98] C. S. Fadley, R. J. Baird, W. Sickhaus, T. Novakov. and S. AL. Bergstrom, J. Electron spectrosc. Relat. Phenom, **4**, 93 (1974).

[99] V. I. Nefedov and O. A. Baschenko, J. Electron Spectrosc. Relat. Phenom. **47**, 1 (1988).

[100] D. R. Penn, Phys. Rev. B **35**, 482 (1987)

[101] G. Binnig, H. Rohrer, Ch. Gerber, and E. Weibel, Phys. Rev. Lett. **49**, 57 (1982).

[102] J. A. Stroscio, R. M. Feenstra, and A. P. Fein, Rev. Lett. **57**, 2579 (1986).

[103] J. M. Carpinelli, H. H. Weitering, E. W. Plummer, and R. Stumpf, Nature **381**, 398 (1996).

[104] L. De Broglie, Annales de Physique **3**, 22C128 (1925).

[105] M. von Ardenne, Zeitschrift für technische Physik (in German) **19**, 407 (1938)

[106] A. V. Crewe, M. Isaacson, and D. Johnson, Rev. Sci. Inst. **40**, 241 (1969).

[107] R. F. Egerton, Rep. Prog. Phys. **72**, 016502 (2009).

[108] R. Herger, P. R. Willmott, O. Bunk, C. M. Schlepütz, B. D. Patterson, and B. Delley, Phys. Rev. Lett. **98**, 076102 (2007).

[109] R. Bachelet, F. Sánchez, F. J. Palomares, C. Ocal and J. Fontcuberta, Appl. Phys. Lett. **95**, 141915 (2009).

[110] T. Ohnishi, K. Shibuya, and M. Lippmaa, D. Kobayashi, H. Kumigashira, and M.Oshima, and H. Koinuma, Appl. Phys. Lett. **85**, 272 (2004).

[111] M. Radovic, N. Lampis, F. Miletto, P. Perna, Z. Ristic, M. Salluzzo, C. M. Schleputz, and U. Scottiddi Uccio, Appl. Phys. Lett. **94**, 022901 (2009).

[112] B. Zheng, and N. Binggeli, Phys. Rev. B **82**, 245311 (2010).

[113] M. Angeloni, G. Balestrino, N. G. Boggio, P. G. Medaglia, P. Orgiani, and A. Tebano, J. Appl. Phys. **96**, 6387 (2004).

[114] B. J. Kim, D. Y. Kwon, T. Yajima, C. Bell, Y. Hikita, B. G. Kim, and H. Y. Hwang, Appl. Phys. Lett. **99**, 092513 (2011).

[115] W. Braun, Applied RHEED Reflection High-Energy Electron Diffraction During Cystal Growth Springer. 1999.

[116] H. Y. Hwang, Y. Iwasa, M. Kawasaki, B. Keimer, N. Nagaosa, and Y. Tokura, Nat Mater **11**, 103 (2012).

[117] C. H. Ahn, A. Bhattacharya, M. Di Ventra, J. N. Eckstein, C. D. Frisbie, M. E. Gershenson, A. M. Goldman, I. H. Inoue, J. Mannhart, A. J. Millis, A. F. Morpurgo, D. Natelson, and J. -M. Triscone, Rev. Mod. Phys. **78**, 1185 (2006).

[118] M. Bibes, E. Villegas Javier, and A. Barthélémy, Advances in Physics **60**, 5 (2010).

[119] R. G. Moore, J. Zhang, V. B. Nascimento, R. Jin, J. Guo, G. T. Wang, Z. Fang, D. Mandrus , and E. W. Plummer, Science **318**, 615 (2007).

[120] R. G. Moore, V. B. Nascimento, J. Zhang, J. Rundgren, R. Jin, D. Mandrus, and E. W. Plummer, Phys. Rev. Lett. **100**, 066102 (2008).

[121] J. Chakhalian, J. W. Freeland, G. Srajer, J. Strempfer, G. Khaliullin, J.C. Cezar, T. Charlton, R. Dalgliesh, C. Bernhard, G. Cristiani, H. U. Habermeier, and B. Keimer, Nat. Phys. **2**, 244 (2006).

[122] P. Yu, W. Luo, D. Yi, J. X. Zhang, M. D. Rossell, C. -H. Yang, L. You, G. Singh-Bhalla, S. Y. Yang, Q. He, Q. M. Ramasse, R. Erni, L. W. Martin, Y. H. Chu, S. T. Pantelides, S. J. Pennycook, and R. Ramesh, Proceedings of the National Academy of Sciences **109**, 9710 (2012).

[123] K. Yoshimatsu, T. Okabe, H. Kumigashira, S. Okamoto, S. Aizaki, A. Fujimori, and M. Oshima, Phys. Rev. Lett. **104**, 147601 (2010).

[124] J. H. Ngai, F. J. Walker, and C. H. Ahn, Annual Rev. of Materials Research **44**, 1 (2014).

[125] H. Kroemer, Rev. Mod. Phys. **73**, 783 (2001).

[126] P. R. Willmott, S. A. Pauli, R. Herger, C. M. Schleptz, D. Martoccia, B. D. Patterson, B. Delley, R. Clarke, D. Kumah, C. Cionca, and Y. Yacoby, Phys. Rev. Lett. **99**, 155502 (2007).

[127] A. S. Kalabukhov, Y. A. Boikov, I. T. Serenkov, V. I. Sakharov, V. N. Popok, R. Gunnarsson, J. Brjesson, N. Ljustina, E. Olsson, D. Winkler, and T. Claeson, Phys. Rev. Lett. **103**, 146101 (2009).

[128] W. Siemons, G. Koster, H. Yamamoto, W. A. Harrison, G. Lucovsky, T. H. Geballe, D. H. A. Blank, and M. R. Beasley, Phys. Rev. Lett. **98**, 196802 (2007).

[129] G. Herranz, M. Basletić, M. Bibes, C. Carrétéro, E. Tafra, E. Jacquet, K. Bouzehouane, C. Deranlot, A. Hamzic, J.-M. Broto, A. Barthélémy, and A. Fert, Phys. Rev. Lett. **98**, 216803 (2007).

[130] R. Pentcheva, and W. E. Pickett, Phys. Rev. Lett. **102**, 107602 (2009).

[131] U. Schwingenschlögl, and C. Schuster, Chem. Phys. Lett. **467**, 354 (2009).

[132] J. M. D. Coey, M. Viret, and S. von Molnr, Adv. Phys. **48**, 167 (1999).

[133] I. žutić, J. Fabian, and S. Das Sarma, Rev. Mod. Phys. **76**, 323 (2004).

[134] Y. Tokura, Rep. Prog. Phys. **69**, 797 (2006).

[135] A. Urushibara, Y. Moritomo, T. Arima, A. Asamitsu, G. Kido, and Y. Tokura, Phys. Rev. B **51**, 14103 (1995).

[136] M. Izumi, Y. Konishi, T. Nishihara, S. Hayashi, M. Shinohara, M. Kawasaki, and Y. Tokura, App. Phys. Lett. **73**, 2497 (1998).

[137] T. Becker, C. Streng, Y. Luo, V. Moshnyaga, B. Damaschke, N. Shannon, and K. Samwer, Phys. Rev. Lett. **89**, 237203 (2002).

[138] M. B. Lepetit, B. Mercey, and C. Simon, Phys. Rev. Lett. **108**, 087202 (2012).

[139] R. Bertacco, J.P. Contour, A. Barthemy, and J. Olivier, Surf. Sci. **511**, 366 (2002).

[140] Å. F. Monsen, F. Song, Z. S. Li, J. E. Boschker, T. Tybell, E. Wahlström, J. W. Wells, Surf. Sci. **606**, 1360 (2012).

[141] L. Poggini, S. Ninova, P. Graziosi, M. Mannini, V. Lanzilotto, B. Cortigiani, L. Malavolti, F. Borgatti, U. Bardi, F. Totti, I. Bergenti, V.A. Dediu, and R. Sessoli, J. Phys. Chem. C **118**, 13631 (2014).

[142] A. T. Wong, C. Beekman, H. Guo, W. Siemons, Z. Gai, E. Arenholz, Y. Takamura, T. Z. Ward, Applied Physics Letters, **105**, 052401 (2014).

[143] P. Yu, W. Luo, D. Yi, J. X. Zhang, M. D. Rossell, C. Yang, L. You, G. Singh-Bhalla, S. Y. Yang, Q. He, Proc. Natl. Acad. Sci. **109**, 9710 (2012).

[144] Y. -M. Kim, A. Kumar, A. Hatt, A. N. Morozovska, A. Tselev, M. D. Biegalski, I. Ivanov, E. A. Eliseev, S. J. Pennycook, J. M. Rondinelli, S. V. Kalinin, and A. Y. Borisevich. Adv. Mater. **25**, 2497 (2013).

[145] T. T. Fister, D. D. Fong, J. A. Eastman, P. M. Baldo, M. J. Highland, P. H. Fuoss, K. R. Balasubramaniam, J. C. Meador, P. A. Salvador, Appl. Phys. Lett. **93**, 151904 (2008).

[146] M. Nakamura, F. Kagawa, T. Tanigaki, H. S. Park, T. Matsuda, D. Shindo, Y. Tokura, and M. Kawasaki, Phys. Rev. Lett. **116**,156801 (2016).

[147] S. M. Young and A. M. Rappe, Phys. Rev. Lett. **109**,116601 (2012).

[148] A. W. Bett, F. Dimroth, G. Stollwerck, O. V. Sulima, Appl. Phys. A, **69**, 119 (1999).

[149] E. Assmann, P. Blaha, R. Laskowski, K. Held, S. Okamoto, and G. Sangiovanni, Phys. Rev. Lett. **110**,078701 (2013).

[150] S. Y. Yang, J. Seidel, S. J. Byrnes, P. Shafer, C. -H. Yang, M. D. Rossell, P. Yu, Y. -H. Chu, J. F. Scott, J. W. Ager,III, L. W. Martin and R. Ramesh, **5**, 143 (2010).

[151] J. -S. Lee, D. A. Arena, P. Yu, C. S. Nelson, R. Fan, C. J. Kinane, S. Langridge, M. D. Rossell, R. Ramesh, and C. -C. Kao, Phys. Rev. Lett **105**, 257204 (2010).

[152] D. Schumacher, A. Steffen, J. Voigt, J. Schubert, and Th. Brückel, H. Ambaye and V. Lauter, Phys. Rev. B **88**, 144427 (2013).

[153] D. McLean: Grain Boundaries in Metals, Oxford University Press, London (1957).

[154] D. R. Harries, A. D. Marwick, Phil. Trans. R. Soc. A **295**, 197-207 (1980).

[155] Z. Cai, M. Kubicek, J. Fleig, B. Yildiz, Chem. Mater. **24**, 1116 (2012).

[156] S. Jiang, J. Solid State Electrochem. **11**, 93 (2007).

[157] L. Yang, L. Tan, X. Gu, W. Jin, L. Zhang, N. Xu, Ind. Eng. Chem. Res. **42**, 2299 (2003).

[158] W. S. Yoon, Y. Paik, X. Q. Yang, M. Balasubramanian, J. McBreen, and C. P. Grey, Electrochem. Solid State Lett. **5**, A263 (2002).

[159] D. Serrate, J. M. De Teresa, J. Blasco, M. R. Ibarra, L. Morellon, and C. Ritter, Appl. Phys. Lett. **80**, 4573 (2002).

[160] I. Hamada, A. Uozumi, Y. Morikawa, A. Yanase, H. Katayama-Yoshida, J. Am. Chem. Soc. **133**, 18506 (2011).

[161] G. C. Miles, M. C. Stennett, I. M. Reaney, A. R. West, J. Mater. Chem. **15**, 798 (2005).

[162] M. P. Seah, Journal of Catalysis **57**, 450-457 (1979).

[163] E. D. Hondros and M. P. Seah: Intern. Metals Rev. **22**, 262 (1977).

[164] J. H. Westbrook, Metall. Rev. **9**, 415-70 (1964).

[165] J. R. Rellick, C. J. McMahon, Metall. Trans. **5**, 2439-50 (1974).

[166] R. F. Tylecote, A History of Metallurgy (Institute of Metals, London, (1989).

[167] G. Agricola, De Re Metallica (J. Froben and N. Episcopius, Basel, 1556, translated by H.C. Hoover, L.H. Hoover, London, 1912, reprinted by Dover Publications, New York, 1950)

[168] J. Y. Laval, T. S. Orlova, Supercond. Sci. Technol. **16**, 1139 (2003).

[169] C. R. M. Grovenor, J. Phys. C **18**, 4079 (1985).

[170] C. R. M. Grovenor, P. E. Batson, D. A. Smith, and C. Y. Wang, Philos. Mag. A **50**, 409 (1984).

[171] M. M. Mandurah, K. C. Saraswat, C. R. Helms, and T. I. Kamins, J. Appl. Phys. **51**, 5755 (1980).

[172] J. M. Penissona, T. Nowickib, and M. Biscondib, Acta Cryst. **58**, 947 (1988).

[173] E. D. Hondros, M. P. Seah, S. Hofmann, P. Lejček, in Physical Metallurgy, 4th edn., ed. by R. W. Cahn, P. Haasen (North-Holland, Amsterdam, (1996).

[174] P. Doig, P. E. J. Flewitt, Acta Metall. **29**, 1831 (1981).

[175] J. Bruley, I. Tanaka, H. J. Klebe, M. R*ü*hle, Anal. Chim. Acta **297**, 97 (1994).

[176] P. E. Batson, N. D. Browning, D. A. Muller, MSA. Bull. **24**, 371 (1994).

[177] T. T. Tsong, Atom-Probe Field-Ion Microscopy (Cambridge University Press, Cambridge, 1990).

[178] S. Hofmann, Scanning Electron Microsc.III, 1071 (1985).

[179] S. Hofmann, J. Chim. Phys. **84**, 141 (1987).

[180] J. M. Blakely and J. C. Shelton, 'Equilibrium Adsorption and Segregation' in Surface Physics of Materials, 1, J. M. Blakely (ed.), Academic Press, 189-238 (1975).

[181] K. J. Rawlings, S. D. Foulias and B. J. Hopkins, Surf. Sci. **109**, 513 (1981).

[182] M. P. Seah and E. D. Hondros, Proc. R. Soc. London, **A335**, 191-212 (1973).

[183] S. Brunauer, L. S. Demming, W. E. Demming, and E. Teller, J. Am. Cerum. Soc., **62**, 1723-32 (1940).

[184] E. D. Hondros and M. P. Seah, Metall. Trans. **8A**, 1363-71 (1977).

[185] M. Guttmann, Surt Sci. 53, 213 (1975).

[186] P. Wynbaltt, and R. N. Ku, Interfacial Segregation, p. 115. Edited by W. C.Johnson and J. M. Blakely. American Society for Metals, Metals Park, OH, 1979.

[187] Y. W. Lee, and H. I. Aaronson, Surf. Sci., **95**, 227 (1980).

[188] Y. W. Lee, and H. I. Aaronson, Acta Metall., **28**, 539 (1980).

[189] R. Defay, I. Prigogine, A. Bellmans, and D. H. Everett, Surface Tension and Adsorption. Wiley, New York, 1966

[190] J. J. Burton and E. S. Machlin, Phys. Rev. Lett., **37**, 1433 (1976).

[191] W. D. Kingery, J. Am. Ceram. Soc., **57** 1 (1974).

[192] J. Frenkel, Kinetic Theory of Liquids. Oxford University Press, New York, 1946.

[193] M. F. Yan, R. M. Cannon, H. K. Bowen, and R. C. Coble, L Am. Cerum. Soc., **60**, 120(1977).

[194] M. F. Yan, R. M. Cannon, and H. K. Bowen, J: Appl. Phys., **54**, 764 (1983).

[195] K. L. Kliewer, and J. S. Koehler, Phys. Rev. A, Gen. Phys., **A140**, 1226 (1965).

[196] S. B. Desu, and D. A. Payne, J. Am. Ceram. Soc. **73**, 3391 (1990).

[197] W. Kohn and L. J. Sham, Phys. Rev. **140**, A1133 (1965).

[198] A. D. Becke, J. Chem. Phys. **98**, 5648 (1993).

[199] S. M. Foiles, M. I. Baskes, and M. S. Daw, Phys. Rev. B **33**, 7983 (1986).

[200] G. J. Fix, Phase field models for free boundary problems Free Boundary Problems: Theory and Applications vol 2 (Boston, MA: Pitman) (1983).

[201] J. S. Langer, Models of pattern formation in first-order phase transitions Directions in Condensed Matter Physics (Singapore: World Scientific) (1986).

[202] L. Q. Chen, A. Khachaturyan, Acta Mater. **39**, 2533 (1991).

[203] Y. Wang, L. Q. Chen, A. G. Khachaturyan, Acta Metall. Mater. **41**, 279 (1993).

[204] A. Khachaturyan, Sov. Phys. Solid State **9**, 2040 (1968).

[205] A. -G. Khachaturyan, Theory of Structural Transformations in Solids, Wiley-Interscience publications, Wiley, New York, (1983)

Vita

Lina Chen was born in February 1983 in Fuyang City, Anhui Province, China. She finished her undergraduate studies at Anhui University in July 2006. She earned a master of science degree in Physics from the University of Science and Technology of China in July 2009. In August 2009 she came to Louisiana State University to pursue graduate studies in mathematics. She is currently a candidate for the degree of Doctor of Philosophy in Physics, which will be awarded in August
2016.